



PACIFIC EARTHQUAKE ENGINEERING RESEARCH CENTER

Component Testing, Stability Analysis and Characterization of Buckling-Restrained Unbonded BracesTM

Cameron Black

Nicos Makris

University of California, Berkeley

Ian Aiken

Seismic Isolation Engineering, Inc.

Oakland, California

Final Report to Nippon Steel Corporation, Tokyo, Japan

Component Testing, Stability Analysis and Characterization of Buckling-Restrained Unbonded BracesTM

Cameron Black

Graduate Student Researcher
Department of Civil and Environmental Engineering
University of California, Berkeley

Nicos Makris

Professor
Department of Civil and Environmental Engineering
University of California, Berkeley

Ian Aiken

Principal
Seismic Isolation Engineering, Inc.
Oakland, California

Final Report to Nippon Steel Corporation, Tokyo, Japan

PEER Report 2002/08
Pacific Earthquake Engineering Research Center
College of Engineering
University of California, Berkeley

September 2002

Abstract

This report presents the results of a comprehensive component testing program on a type of buckling-restrained brace known as the Unbonded Brace™. This commercially available seismic brace enhances the earthquake resistance of building structures by providing supplemental strength and energy dissipation.

The report introduces the braces by presenting an in-depth analysis on their stability against: (a) global flexural buckling, (b) buckling of the inner core in higher modes, and (c) plastic torsional buckling of the inner core. After establishing the formulae that describe the brace capacity the report proceeds with a survey on past experimental studies conducted on *unbonded braces*.

Subsequently, the report presents the results from a two-phase experimental testing program at UC Berkeley that tested five buckling-restrained braces with various configurations. The unbonded braces tested are representative of the braces designed for use in two major building projects in Northern California. The test results established that the unbonded braces tested deliver stable and repeatable behavior. Their plastic deformation capacity exceeds the specified requirement both in terms of ultimate deformation and in terms of cumulative plastic deformation.

The behavior of the unbonded brace is characterized at the macroscopic, force-deformation level with the Bouc-Wen model, which is found to predict the brace behavior with fidelity. The parameters of the macroscopic model are related to the geometric characteristics of the brace and the mechanical properties of the steel and can be used with confidence to characterize the behavior of the braces.

A nonlinear analysis on the response of a single-degree-of-freedom structure equipped with the mechanism of the unbonded brace illustrates the benefits of added strength and dissipation in association with the ductility demands on the brace. This analysis also demonstrates that a bilinear force-deformation relation produces results in close agreement with the Bouc-Wen model.

The study concludes that the unbonded brace is a reliable and practical alternative to conventional lateral load-resisting systems, and is capable of enhancing the earthquake resistance of new and existing structures.

Contents

Abstract.....	iii
Table of Contents.....	v
List of Figures.....	vii
List of Tables.....	xi
List of Symbols.....	xiii
Acknowledgments.....	xvii
1 Introduction.....	1
1.1 Background.....	1
1.2 Implementation of the Unbonded Brace in the United States.....	3
2 Stability Analysis.....	7
2.1 Global Stability of Unbonded Braces under Axial Compression.....	7
2.2 Buckling of the Inner Core in Higher Modes.....	9
2.3 Torsional Buckling of the Inner Core.....	14
2.3.1 Elastic Buckling of the Cruciform Column.....	14
2.3.2 Inelastic Buckling of the Cruciform Column.....	19
2.3.3 Total Deformation Theory of Plasticity.....	19
2.3.4 Incremental Theory of Plasticity.....	21
3 Past Experimental Studies on Unbonded Braces.....	27
4 Component Testing of Unbonded Braces.....	33
4.1 Description of Braces.....	33
4.2 Experimental Setup.....	35
4.3 Instrumentation.....	40
4.4 Testing Protocols.....	40
4.4.1 Spring 1999 Test Protocol.....	44
4.4.2 Fall 2000 Test Protocol.....	47
4.5 Experimental Results.....	51
4.5.1 Spring 1999 Test Results.....	51
4.5.2 Fall 2000 Test Results.....	60
4.6 Comparison of Measured and Computed Stiffness Values.....	66
4.6.1 Elastic (Pre-yielding) Stiffness of the Brace.....	66
4.6.2 Secondary (Tangent) Stiffness.....	71
4.7 Cumulative Plastic Ductility Demands.....	71
5 Characterization of Mechanical Behavior.....	79
5.1 Macroscopic Modeling of Hysteretic Behavior.....	79
5.2 Estimation of Structural Response.....	82
6 Conclusions.....	91
References.....	93
Appendix A Acceptance Criteria for Fall 2000 Tests.....	97
Appendix B Estimation of Yield Displacement.....	99

List of Figures

Figure 1-1. Schematic of the unbonded brace (left), the steel core (center) and the outer tube (right)	2
Figure 2-1. (a) Unbonded brace under axial loading, (b) distributed load along the inner core in its deformed configuration and (c) distributed load along the encasing mortar/outer tube.....	8
Figure 2-2. Schematic of a cruciform column under axial compression. The geometry of flanges has bifurcated to a bent position (top). Normal and shear stresses acting on a cross section of a bent flange (bottom).....	15
Figure 2-3. Deflected shape of a plate under plane compression with one edge free and the three other edges simply supported.....	17
Figure 2-4. Recorded force-displacement curve (top). Values of the secant modulus, tangent modulus and Poisson ratio as the inner core contracts (center plots). Torsional buckling stresses computed with the total deformation (Equation 2-49) and the incremental (Equation 2-62) theories of plasticity (bottom). The results by the intuitive formulation proposed by Bleich are also shown	25
Figure 2-5. Brace at maximum elongation showing unsupported length (approximately 3.5"). The dark material covering the brace is the unbonding material layer	26
Figure 3-1. Unbonded braces tested in Japan (figures a through d) and at UC Berkeley (figures e and f). Brace sizes are shown to scale.....	28
Figure 3-2. Previous testing configurations.....	29
Figure 3-3. Euler buckling curves of five unbonded braces that have the same inner core (19x90 mm) but different outer tube sizes tested by Watanabe et al. (1988), Wada et al. (1989) and Watanabe et al. (1992)	31
Figure 4-1. Euler buckling curves for the specimens tested at UC Berkeley. Lines indicating the steel core axial yield loads are included for comparison	34
Figure 4-2. Front and plan views of Specimen 99-1	36
Figure 4-3. Front and plan views of Specimen 99-2	37
Figure 4-4. Front and plan views of Specimen 99-3	38
Figure 4-5. Elevation and plan views of Specimens 00-11 and 00-12	39
Figure 4-6. Plan and elevation views of the setup for unbonded brace test	41
Figure 4-7. Views of the unbonded brace mounted on the fall 2000 test setup.....	42
Figure 4-8. Location of potentiometers that measure brace displacements for spring 1999 tests (top) and fall 2000 tests (bottom)	43

Figure 4-9. SAC basic loading history used for spring 1999 test specimens	45
Figure 4-10. SAC near-field loading protocol imposed on Specimen 99-1	46
Figure 4-11. Low-cycle fatigue test imposed on Specimen 99-2	46
Figure 4-12. Brace displacement histories computed for an idealized five-story building subjected to the 1994 Sylmar record (top) and the 1940 El Centro record (bottom). These histories were used as displacement histories on Specimen 99-3	48
Figure 4-13. OSHPD brace loading history for fall 2000 test specimens	49
Figure 4-14. Drift-induced displacement histories determined from nonlinear structural analyses of a steel structure. They are representative of the most severe brace displacement histories for the Design Basis Earthquake (top) and Upper Bound Earthquake (bottom) used in the design of the Kaiser Santa Clara Medical Center	50
Figure 4-15. Top: SAC basic loading history. Center: The recorded force is plotted versus the displacement of the yielding portion (Specimen 99-1). Bottom: The recorded force is plotted versus the displacement of the entire brace (i.e., flexibility of connections included)	53
Figure 4-16. Top: SAC near-field protocol. Center: The recorded force is plotted against the displacement measured across the yielding portion (Specimen 99-1). Bottom: The recorded force is plotted versus the displacement of the inner core relative to each end of the tube	54
Figure 4-17. SAC basic loading history (top) and recorded force-displacement loops for Specimen 99-2	55
Figure 4-18. Low-cycle fatigue displacement history consisting of 15 cycles (top) and recorded force-displacement loops of Specimen 99-2. The brace exhibits stable, repeatable behavior without any signs of degradation until the 15th cycle when fracture occurs	56
Figure 4-19. SAC basic loading history (top) and recorded force-displacement loops for Specimen 99-3	57
Figure 4-20. Imposed displacement history derived from the computed interstory drift of an idealized five-story building subjected to the 1994 Northridge earthquake Sylmar motion (top) and the force-displacement loops recorded from Specimen 99-3 (bottom)	58
Figure 4-21. Imposed displacement history derived from the computed interstory drift of an idealized five-story building subjected to the 1994 Northridge earthquake Sylmar motion (top) and the force-displacement loops recorded from Specimen 99-3 (bottom)	59

Figure 4-22. Top: OSHPD brace loading history. Center: The recorded force is plotted against the displacement measured across the yielding portion (Specimen 00-11). Bottom: The recorded force is plotted versus the displacement of the inner core relative to each end of the tube.....	61
Figure 4-23. Bottom: Low-cycle fatigue test. Center: The recorded force is plotted against the displacement measured across the yielding portion (Specimen 00-11). Bottom: The recorded force is plotted versus the displacement of the inner core relative to each end of the tube.....	62
Figure 4-24. Top: OSHPD basic displacement history. Center: The recorded force is plotted versus the displacement of the yielding portion (Specimen 00-12). Bottom: The recorded force is plotted versus the displacement of the entire brace (i.e., flexibility of connections included).	63
Figure 4-25. Top: Displacement loading history that approximates the interstory drift of a structure subjected to the DBE earthquake. Center: The recorded force is plotted versus the displacement of the yielding portion (Specimen 00-12). Bottom: The recorded force is plotted versus the displacement of the entire brace (i.e., flexibility of connections included).	64
Figure 4-26. Top: Displacement loading history that approximates the interstory drift of a structure subjected to the MCE earthquake. Center: The recorded force is plotted versus the displacement of the yielding portion (Specimen 00-12). Bottom: The recorded force is plotted versus the displacement of the entire brace (flexibility of connections included).....	65
Figure 4-27. Possible unbonded brace steel core configurations. Top: configuration of Specimens 99-3, 00-11 and 00-12. Bottom: configuration of Specimens 99-1 and 99-2.....	67
Figure 4-28. Force-displacement loops for the different brace sizes tested along with the estimated stiffness values.....	69
Figure 4-29. Plot showing estimated secondary stiffness values calculated from Tests 1, 3 and 5 of the OSHPD brace loading history for Specimen 00-12.....	72
Figure 4-30. Top: Loading history normalized to the yield displacement. Thick segments indicate inelastic deformation. Center: Force-displacement loop. The successive visits in the inelastic range are counted with the index <i>i</i> . Bottom: Increase of Cumulative Plastic Ductility with time.	74
Figure 4-31. Drift-induced displacement history for the DBE earthquake used to test Specimen 00-12 (top) and the running value of the Cumulative Plastic Ductility (bottom).	75
Figure 5-1. Comparison of recorded hysteresis loops obtained from the first inelastic test of Specimen 00-12 (Test 1, OSHPD Brace Loading History) and those obtained by the calibrated Bouc-Wen model.....	81

Figure 5-2. Comparison of experimental hysteresis loops from Specimen 00-12 and the Bouc-Wen approximation. The model has been calibrated to Test 4 (bottom-left).....	83
Figure 5-3. Comparison of recorded hysteresis loops obtained from Specimen 00-12 when subjected to the drift-induced loading histories and the calibrated Bouc-Wen model.	84
Figure 5-4. Schematic of a SDOF structure with an unbonded brace.	85
Figure 5-5. Exact drift and base shear spectra for a linear SDOF structure with an unbonded brace subjected to the 1971 San Fernando earthquake, Pacoima Dam record.....	88
Figure 5-6. Exact drift and base shear spectra for a linear SDOF structure with an unbonded brace subjected to the 1979 El Centro earthquake, Array #5 record.	89
Figure 5-7. Exact drift and base shear spectra for a linear SDOF structure with an unbonded brace subjected to the SAC LA01 record.....	90
Figure B-1. Bilinear force-deformation relation.	100

List of Tables

Table 1-1.	Implementation of the unbonded brace in the United States	4
Table 3-1.	Comparison of unbonded braces tested (Watanabe et al. (1988), Wada et al. (1989) and Watanabe et al. (1992)).....	30
Table 4-1.	Unbonded braces tested at UC Berkeley in spring 1999 and fall 2000.	33
Table 4-2.	SAC basic loading history for spring 1999 test specimens.....	44
Table 4-3.	OSHPD brace loading history for fall 2000 test specimens	49
Table 4-4.	Comparison of measured and theoretical elastic stiffness values.....	70
Table 4-5.	Strain hardening moduli for Specimen 00-12.....	71
Table 4-6.	Cumulative Plastic Ductility calculations for the OSHPD brace loading history..	73
Table 4-7.	Cumulative Plastic Ductility of tests performed at UC Berkeley	76
Table 4-8.	Average, maximum response quantities of buckling-restrained braces for ground motions considered at each hazard level. (Adapted from Sabelli, 2000)	77
Table 5-1.	Parameters used in Bouc-Wen Model.....	80
Table A-1.	Specimens 00-11 and 00-12 maximum forces — Acceptance requirement 2.....	98

List of Symbols

A	area [m^2]
A_{con}	area of connection portion of the inner core [m^2]
A_{core}	area of inner core [m^2]
A_i	area of yielding portion of the inner core [m^2]
A_{tr}	area of transition portion of the inner core [m^2]
b	width of inner core [m]
C_o	damping coefficient of a single-degree-of-freedom frame structure [kg/sec]
E	Young's modulus [N/m^2]
E_c	Young's modulus of encasing concrete [N/m^2]
E_i	Young's modulus of inner core [N/m^2]
E_s	Secant modulus of steel core [N/m^2]
E_t	Tangent modulus of steel core [N/m^2]
E_o	Young's modulus of encasing mortar/outer tube [N/m^2]
f	$= F_y/mg$, normalized brace yield force
F_y	brace yield force [N]
g	acceleration of gravity [m/sec^2]
G	elastic shear modulus [N/m^2]
G_s	secant shear modulus [N/m^2]
I	moment of inertia [m^4]
I_i	moment of inertia of inner core [m^4]
I_{tube}	moment of inertia outer tube [m^4]
I_o	moment of inertia encasing mortar/outer tube [m^4]
J_2	second invariant of deviatoric stress tensor, s_{ij}
k	elastic stiffness [N/m]

k^c	stiffness computed analytically [N/m]
k^e	stiffness obtained from experimental data [N/m]
k_2	secondary (post-yield) stiffness [N/m]
k_{con}	stiffness of connection portion of inner core [N/m]
k_i	stiffness of the yielding portion of inner core [N/m]
k_{tr}	stiffness of the transition portion of inner core [N/m]
K_o	lateral stiffness of a single-degree-of-freedom frame structure [N/m]
KL	effective length [m]
L	length [m]
l	length of inner core protruding from the outer tube/encasing mortar [m]
L_{con}	length of the connection portion of the inner core [m]
L_i	length of the yielding portion of the inner core [m]
L_{total}	total length of the inner core [m]
L_{tr}	length of the transition portion of the inner core [m]
m	mass of single-degree-of-freedom frame structure [kg]
M^A	acting torque on a cruciform section [Nm]
M^R	resisting torque on a cruciform section [Nm]
n	dimensionless parameter used in Bouc-Wen model
P	axial load [N]
P_{cr}	critical load [N]
P_e	Euler buckling load [N]
P_y	axial yield load [N]
$q(x)$	transverse distributed load [N]
s_{ij}	deviatoric stress tensor
t	thickness of the inner core [m]
T_o	period of unbraced single-degree-of-freedom structure [sec]

$u(t)$	lateral displacement of single-degree-of-freedom frame structure [m]
\ddot{u}_g	ground acceleration [m/sec^2]
u_p	plastic displacement [m]
u_y	yield displacement [m]
$w(x)$	deflection of flange [m]
x	displacement variable [m]
$y(x)$	transverse displacement [m]
$z(t)$	dimensionless hysteretic parameter used in Bouc-Wen model
α	= k_2/k , post- to pre-yield stiffness
β	distributed spring constant of encasing mortar [N/m]
β	dimensionless parameter used in Bouc-Wen model
γ	dimensionless parameter used in Bouc-Wen model
δ_{br}	brace displacement [m]
δ_{ij}	Kronecker delta
ε	strain
ε_y	yield strain
ζ	viscous damping ratio
μ	ductility
μ_p	plastic ductility
ν	Poisson's ratio
σ	stress [N/m^2]
σ_y	yield stress [N/m^2]
τ	shear stress [N/m^2]
$\phi(x)$	rotation of cruciform section at a distance x from the center of the brace [rad]

Acknowledgments

The unbonded braces and the financial support for their testing were provided by Nippon Steel Corporation, Japan. Technical assistance during testing in the Structural Research Laboratory at the Richmond Field Station, University of California, was provided by Mr. Don Clyde, Mr. Wes Neighbour and Mr. David MacLam. Their help is greatly appreciated.

The Pacific Earthquake Engineering Research Center is supported by the Earthquake Engineering Research Centers Program of the National Science Foundation under award number EEC-9701568.

1 Introduction

1.1 Background

Following the behavior of building structures during recent earthquakes, it has been recognized that increased strength and stable energy dissipation capability are the most desirable mechanical characteristics needed to maintain interstory drift and overall displacements within tolerable levels.

The idea of using yielding metallic devices within the skeleton of a building frame to absorb large portions of the seismic energy is more than 30 years old (Kelly et al. 1972, Skinner et al. 1975). This early work in the area of seismic protection of structures considered torsional beams, flexural beams and other structural mechanisms as the basis for energy dissipation devices. Subsequently, a wide variety of efficient devices that consist of an array of mild steel plates, in triangular or hourglass shapes, have been proposed (Tyler 1978, Bergman and Goel 1987, Whittaker et al. 1991, Tsai et al. 1993). The motivation for plate shapes with variable triangular or hourglass sections is to achieve uniformly distributed yielding throughout the material of the plate, and to avoid localized deformations that will fail the devices rapidly due to low-cycle fatigue.

Another structural steel element that offers strength and energy dissipation while at the same time exhibiting well-distributed yielding is the buckling-restrained brace (BRB). One such buckling-restrained brace is the Unbonded Brace™, manufactured by Nippon Steel Corporation. The *unbonded brace* consists of a steel core member, often referred to as the “core plate,” encased in a steel tube filled with concrete (Figure 1-1). The steel core carries the axial load while the outer tube, via the concrete, provides lateral support to the core and prevents global buckling. A thin layer of material along the steel core at the concrete interface eliminates shear transfer during the elongation and contraction of the steel core and also accommodates its lateral expansion when in compression. It is the ability of the steel core to contract and elongate freely within the confining steel concrete-tube assembly that led to the name “unbonded brace.”

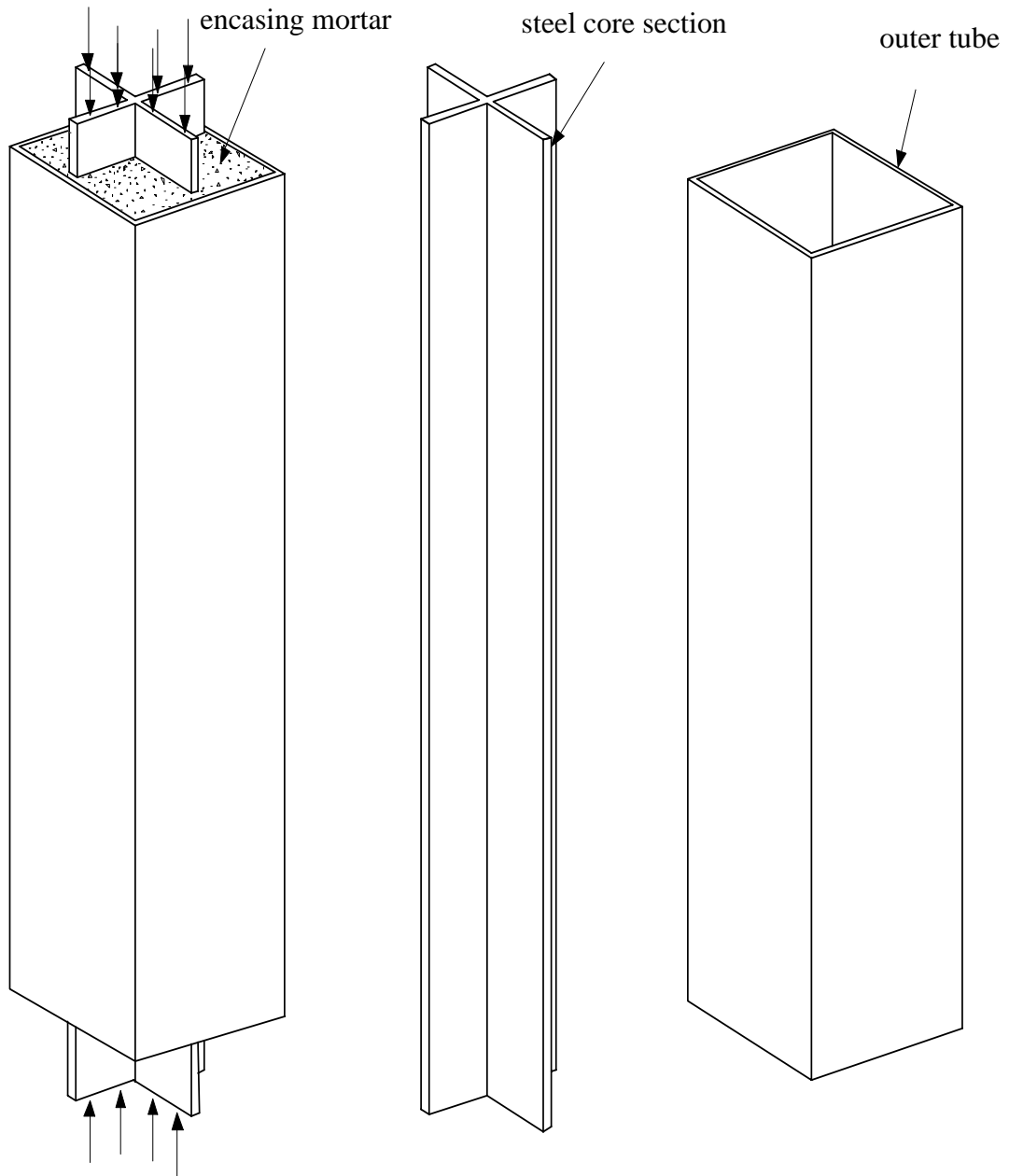


Figure 1-1. Schematic of the unbonded brace (left), the steel core (center) and the outer tube (right).

An early attempt to create a brace that dissipates energy yet does not buckle is reported in the paper by Kimura et al. (1976). The early seismic brace consists of a conventional brace encased in a square steel pipe filled with mortar. While Kimura et al. reported a few stable hysteretic characteristics, it was found that following a compressive loading cycle that the transverse deformation of the mortar resulted in a permanent void space large enough to allow local buckling during subsequent compressive loading.

Mochizuki et al. (1980) conducted tests on similar braces which were wrapped in reinforced concrete, with the concrete kept from adhering to the internal brace by use of a shock-absorbing material. It was found, however, that under repetitive loading the concrete cracks and its buckling restraining effect diminishes (Wada et. al 1989).

This concept was further refined by a team of investigators in Japan (Watanabe et al. 1988, Wada et al. 1989, and Watanabe et al.1992) and resulted in what is known today as the Unbonded Brace™. The simplicity of its design and the outstanding performance of the unbonded brace has attracted the interest of industry and has been made commercially available by Nippon Steel Corporation.

1.2 Implementation of the Unbonded Brace in the United States

The unbonded brace has been used extensively in Japan since 1987 with nearly 200 buildings currently using the brace. The first project in the United States was the Plant and Environmental Sciences Building at the University of California, Davis. Of the 13 buildings using the brace in the United States, six are owned by the University of California and one by the California Institute of Technology. The other owners include the County of Marin (San Rafael, California), King County (Seattle, Washington), the Federal General Services Administration (Salt Lake City, Utah) as well as Hewlett-Packard (Corvallis, Oregon, and Vancouver, Washington). The current list of buildings with pertinent information on the building, the project team, and the unbonded braces used are given in Table 1-1.

Table 1-1. Implementation of the unbonded brace in the United States

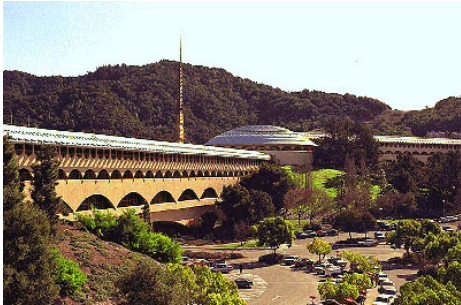
Plant and Environmental Sciences Building — University of California, Davis, California



New steel structure
3-stories + basement, 125,000 sq ft

132 braces
SM490A
 $P_y = 115 - 550$ kips

Marin County Civic Center Hall of Justice — County of Marin, California



Retrofit of reinforced concrete structure
3-6 stories, approx. 600,000 gross sq ft

44 braces
SN400B
 $P_y = 400 - 600$ kips

Broad Center for the Biological Sciences — California Institute of Technology, California



New steel structure
3 stories + basement
118,000 gross sq ft

84 braces
SN490B
 $P_y = 285 - 660$ kips

Hildebrand Hall — University of California, Berkeley, California



Retrofit of reinforced concrete
3 stories + basement
138,000 sq ft

36 braces
SN400B
 $P_y = 200 - 400$ kips

Table 1-1. Continued

Wallace F. Bennett Federal Building — Federal General Services Administration, Salt Lake City, Utah



Retrofit of reinforced concrete structure
8 stories
300,000 sq ft

344 braces
SN490B
 $P_y = 205 - 1905$ kips

Building 5, HP Corvallis Campus — Hewlett-Packard, Corvallis, Oregon



Retrofit of steel structure
2 stories
160,000 sq ft

60 braces
LYP235
 $P_y = 110 - 130$ kips
(photo: Anderson Construction)

Centralized Dining and Student Services Building — University of California, Berkeley, California



New steel structure
4 stories
90,000 sq ft

95 braces
SN490B
 $P_y = 210 - 705$ kips

King County Courthouse — King County, Seattle, Washington



Retrofit of reinforced concrete structure
12 stories
500,000 sq ft

50 braces
SN400B
 $P_y = 200 - 500$ kips

Table 1-1. Continued

Genome and Biomedical Sciences Building — University of California, Davis, California



New steel structure
6 stories + basement
211,000 sq ft

97 braces
SN400B
 $P_y = 150 - 520$ kips

Physical Sciences Building — University of California at Santa Cruz, California



New steel structure
5 stories
136,500 net sq ft

74 braces
SN400B
 $P_y = 150 - 500$ kips

Second Research Building (Building 19B) — University of California, San Francisco, California



New steel structure
5 stories
171,000 sq ft

132 braces
SN400B
 $P_y = 150 - 675$ kips

Kaiser Santa Clara Medical Center Hospital Building Phase I, Kaiser Permanente, Santa Clara, California



New steel construction
3 stories + basement
266,000 sq ft

120 braces
SN400B
 $P_y = 265 - 545$ kips

2 Stability Analysis

2.1 Global Stability of Unbonded Braces under Axial Compression

The global stability of the unbonded brace can be estimated directly from the Euler theory of buckling. Figure 2-1(a) shows the schematic of an unbonded brace in compression, while Figure 2-1(b) and 2-1(c) show the distributed forces on the steel core and the encasing mortar/outer tube in the deformed configuration. The unknown distributed load, $q(x)$, shown in Figure 2-1(b) is the transverse reaction of the outer tube/encasing mortar along the inner steel core. Using the system of axes shown in Figure 2-1, the equilibrium of the inner steel core in its deformed configuration is given by

$$E_i I_i \frac{d^4 y(x)}{dx^4} + P \frac{d^2 y(x)}{dx^2} = -q(x) \quad (2-1)$$

where $y(x)$ is the transverse deflection, P is the axial load, and E_i and I_i are the Young's modulus and the moment of inertia of the inner steel core, respectively. The minus sign on the right-hand side of Equation (2-1) results from the fact that $q(x)$ acts in the direction opposite to the deflection $y(x)$. The equal and opposite distributed load $q(x)$ is loading the encasing mortar/outer tube as shown in Figure 2-1(b). Equilibrium of a segment of the beam gives

$$E_o I_o \frac{d^4 y(x)}{dx^4} = q(x) \quad (2-2)$$

where $y(x)$ is the same transverse deflection appearing in Equation (2-1) and $E_o I_o$ is the flexural rigidity of the encasing mortar/outer tube.

Elimination of the unknown distributed load, $q(x)$, in Equations (2-1) and (2-2) gives

$$E_i I_i \frac{d^4 y(x)}{dx^4} + P \frac{d^2 y(x)}{dx^2} = -E_o I_o \frac{d^4 y(x)}{dx^4} \quad (2-3)$$

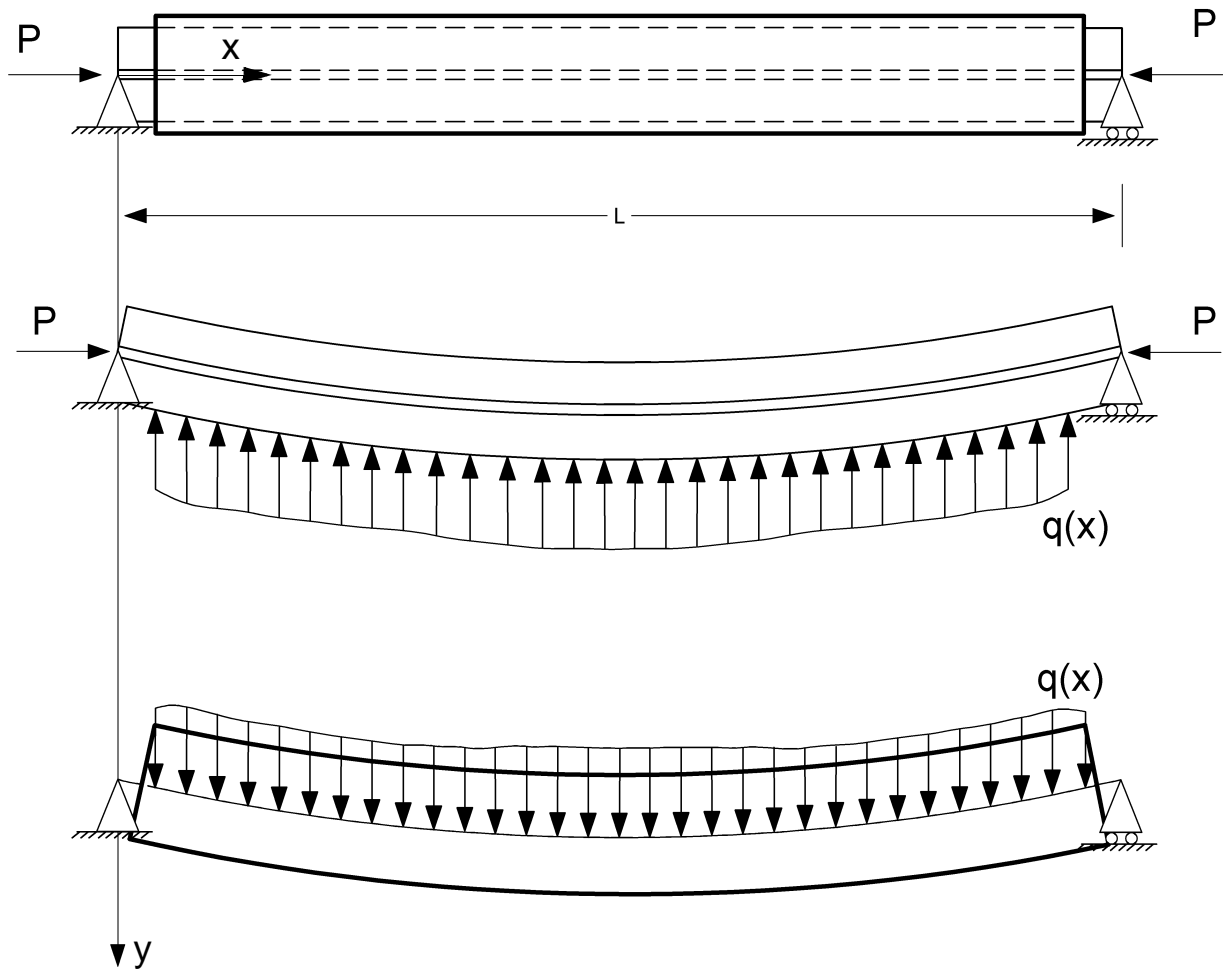


Figure 2-1. (a) Unbonded brace under axial loading, (b) distributed load along the inner core in the deformed configuration and (c) distributed load along the encasing mortar/outer tube.

which, after rearranging terms, yields a homogeneous Euler equation

$$\frac{d^4 y(x)}{dx^4} + \frac{P}{E_i I_i + E_o I_o} \frac{d^2 y(x)}{dx^2} = 0 . \quad (2-4)$$

For a brace with buckling length L , Equation (2-4) yields the critical buckling load of the brace

$$P_{cr} = P_e = \frac{\pi^2}{(KL)^2} (E_i I_i + E_o I_o) \quad (2-5)$$

where KL is the effective (or equivalent) length ($K=1$ for a pinned end condition and $K=2$ for a fixed end condition). Neglecting the bending rigidity of the inner steel core, $E_i I_i$ (which is two to three orders of magnitude smaller than the bending rigidity of the encasing mortar/outer tube, $E_o I_o$), Equation (2-5) simplifies to

$$P_{cr} = P_e \approx \frac{\pi^2 E I_{tube}}{(KL)^2} \quad (2-6)$$

where E and I_{tube} are the elastic Young's modulus and the moment of inertia of the outer tube, respectively. Therefore, Equation (2-6) indicates that the critical load of the unbonded brace is merely the Euler buckling load of the outer tube. Accordingly, the global stability of the brace is ensured when the Euler buckling load of the tube, P_{cr} , exceeds the yielding load of the core, $P_y = \sigma_y A_{core}$.

2.2 Buckling of the Inner Core in Higher Modes

The effectiveness of the unbonded brace is increased when local buckling of the steel core along the restrained length does not occur. Assuming that the reaction of the confining concrete mortar can be approximated by an elastic foundation, the distributed load $q(x)$ exerted along the steel core (see Figure 2-1b) can be expressed by $q(x) = \beta y(x)$, where β is a distributed spring constant with dimension $[F]/[L^2]$ and $y(x)$ is the transverse deflection of the steel core. With this assumption Equation (2-1) gives

$$E_i I_i \frac{d^4 y(x)}{dx^4} + P \frac{d^2 y(x)}{dx^2} + \beta y(x) = 0 . \quad (2-7)$$

The solution of the homogeneous Equation (2-7) can be obtained either by following an energy method or by direct integration. The energy method approach has been presented in the book by Timoshenko and Gere (1961). For this problem the energy method yields the exact critical load; however, it involves the determination of the buckling shape and the number of undulations involved. Herein we present the solution for the critical load by direct integration as it involves a more direct and compact analysis.

Dividing by $E_i I_i$ Equation (2-7) can be expressed as

$$\frac{d^4 y(x)}{dx^4} + 2k^2 \frac{d^2 y(x)}{dx^2} + \zeta^4 y(x) = 0 \quad (2-8)$$

where $k^2 = \frac{1}{2}(P/E_i I_i)$ and $\zeta^4 = \beta/E_i I_i$. A solution to Equation (2-8) is of the form

$$y(x) = A e^{\lambda x} \quad (2-9)$$

which when substituted into Equation (2-8) yields the bi-quadratic equation

$$\lambda^4 + 2k^2 \lambda^2 + \zeta^4 = 0. \quad (2-10)$$

By setting $z = \lambda^2$, Equation (2-10) reduces to a quadratic equation

$$z^2 + 2k^2 z + \zeta^4 = 0 \quad (2-11)$$

with discriminant $\Delta = 2\sqrt{k^4 - \zeta^4}$.

For a given brace, $\zeta = (\beta/E_i I_i)^{1/4}$ is given, whereas $k = \sqrt{P/(2E_i I_i)}$ increases with the load, P .

For the case where $k^4 \leq \zeta^4$, which corresponds to the situation where $P \leq 2\sqrt{\beta E_i I_i}$, the discriminant is imaginary

$$\sqrt{\Delta} = 2ik^2 \sqrt{\frac{\zeta^4}{k^4} - 1} \quad (2-12)$$

and the solutions of Equation (2-11) are

$$z_1 = -k^2(1 - i\delta) \quad (2-13)$$

$$z_1 = -k^2(1 + i\delta) \quad (2-14)$$

where $\delta = \sqrt{\zeta^4/k^4 - 1}$. Recalling that $z = \lambda^2$, the four roots of λ from Equation (2-10) are

$$\lambda_1 = ik(1 - i\delta)^{1/2} \quad (2-15)$$

$$\lambda_2 = -ik(1 - i\delta)^{1/2} \quad (2-16)$$

$$\lambda_3 = ik(1 + i\delta)^{1/2} \quad (2-17)$$

$$\lambda_4 = -ik(1 + i\delta)^{1/2}. \quad (2-18)$$

With the four admissible roots of λ given by Equations (2-15) to (2-18) the general solution of Equation (2-8) is

$$y(x) = A_1 e^{ik(1 - i\delta)^{1/2}x} + A_2 e^{-ik(1 - i\delta)^{1/2}x} + A_3 e^{ik(1 + i\delta)^{1/2}x} + A_4 e^{-ik(1 + i\delta)^{1/2}x}. \quad (2-19)$$

The constants A_1 through A_4 are obtained from the boundary conditions. For a brace that is pinned at both ends, $x = 0$ and $x = L$,

$$y(0) = 0 \quad \text{and} \quad \frac{d^2y(0)}{dx^2} = 0 \quad (2-20)$$

$$y(L) = 0 \quad \text{and} \quad \frac{d^2y(L)}{dx^2} = 0, \quad (2-21)$$

which when applied to Equation (2-19) leads to the homogeneous system

$$\begin{bmatrix} 1 & 1 & 1 & 1 \\ -k^2(1 - i\delta) & -k^2(1 - i\delta) & -k^2(1 + i\delta) & -k^2(1 + i\delta) \\ e^{ik(1 - i\delta)^{1/2}L} & e^{-ik(1 - i\delta)^{1/2}L} & e^{ik(1 + i\delta)^{1/2}L} & e^{-ik(1 + i\delta)^{1/2}L} \\ -k^2(1 - i\delta)e^{ik(1 - i\delta)^{1/2}L} & -k^2(1 - i\delta)e^{-ik(1 - i\delta)^{1/2}L} & -k^2(1 + i\delta)e^{ik(1 + i\delta)^{1/2}L} & -k^2(1 + i\delta)e^{-ik(1 + i\delta)^{1/2}L} \end{bmatrix} \begin{bmatrix} A_1 \\ A_2 \\ A_3 \\ A_4 \end{bmatrix} = \begin{bmatrix} 0 \\ 0 \\ 0 \\ 0 \end{bmatrix}. \quad (2-22)$$

For a non-trivial solution of Equation (2-22), the determinant of the system has to be equal to zero. This can be achieved by setting $\delta = 0$, which makes the first two and last two rows linearly dependent and therefore the determinant vanishes. The requirement for δ to be equal to zero ($k^4 = \zeta^4$) yields a value for the critical load, P_{cr} of

$$P_{cr} = 2\sqrt{\beta E_i I_i} . \quad (2-23)$$

The critical load given by Equation (2-23) is known to the literature (Wada et al. (1989) among others) and can also be obtained from minimization of the strain energy of a beam on an elastic foundation that has assumed m number of local undulations (Timoshenko and Gere 1961).

Equation (2-19) can also be used to obtain the critical buckling load of an unbonded brace with fixed ends at $x = 0$ and $x = L$,

$$y(0) = 0 \quad \text{and} \quad \frac{dy(0)}{dx} = 0 \quad (2-24)$$

$$y(L) = 0 \quad \text{and} \quad \frac{dy(L)}{dx} = 0 . \quad (2-25)$$

When conditions (2-24) and (2-25) are applied to Equation (2-19) one obtains the homogeneous system

$$\begin{bmatrix} 1 & 1 & 1 & 1 \\ ik(1-i\delta)^{1/2} & -ik(1-i\delta) & ik(1+i\delta) & -ik(1+i\delta)^{1/2} \\ e^{ik(1-i\delta)^{1/2}L} & e^{-ik(1-i\delta)^{1/2}L} & e^{ik(1+i\delta)^{1/2}L} & e^{-ik(1+i\delta)^{1/2}L} \\ ik(1-i\delta)^{1/2}e^{ik(1-i\delta)^{1/2}L} & -ik(1-i\delta)^{1/2}e^{-ik(1-i\delta)^{1/2}L} & ik(1+i\delta)^{1/2}e^{ik(1+i\delta)^{1/2}L} & -ik(1+i\delta)^{1/2}e^{-ik(1+i\delta)^{1/2}L} \end{bmatrix} \begin{bmatrix} A_1 \\ A_2 \\ A_3 \\ A_4 \end{bmatrix} = \begin{bmatrix} 0 \\ 0 \\ 0 \\ 0 \end{bmatrix} . \quad (2-26)$$

As before, for a nontrivial solution of Equation (2-26), the determinant of the system must be zero. This is achieved if $\delta = 0$ which makes the first and third, and the second and forth, columns linearly dependent. The requirement that $\delta = 0$ yields a value for the critical load given by Equation (2-23). The above analysis demonstrates that the critical buckling load of the inner core in higher modes is independent of the end conditions of the core.

In order to avoid high order buckling of the inner core, $P_{cr} = 2\sqrt{\beta E_i I_i} \geq \sigma_y A_i$, which requires that

$$\beta \geq \frac{\sigma_y^2 A_i^2}{4E_i I_i} . \quad (2-27)$$

When the inner core has a rectangular cross section, $t \times b$, Equation (2-27) gives

$$\beta > 3 \frac{\sigma_y^2 b}{E_i t} \quad (2-28)$$

whereas, when the inner core is cruciform in cross section, with $A_i \approx 2bt$, Equation (2-27) gives

$$\beta > 12 \frac{\sigma_y^2 t}{E_i b} . \quad (2-29)$$

The value of b/t generally varies from $5 < b/t < 10$ and thus Equation (2-28) requires the highest value of β , which implies that the rectangular inner core requires a larger distributed spring constant to avoid local buckling.

When the inner core has yielded the Young's modulus of the core, E_i , is the tangent modulus, E_t . A value of $E_t = 550ksi$ was found for the tangent modulus from experimental results presented later in this report, while the yield stress was $\sigma_y = 55ksi$. With these values and a value of $b/t = 10$, Equation (2-29) indicates that in order to avoid high-order local buckling, $\beta > 165ksi$.

The value of the distributed spring constant, β , can be estimated by computing the one-dimensional compression modulus of concrete that is confined laterally by the presence of the steel tube and longitudinally by its neighboring concrete. Assuming plane strain conditions

$$\beta = E_c \frac{1 - \nu}{(1 + \nu)(1 - 2\nu)} , \quad (2-30)$$

where E_c and ν are the Young's modulus and Poisson's ratio for the encasing mortar/concrete. For concrete material with a typical value of Young's modulus, $E_c = 21GPa$, and Poisson's ratio, $\nu = 0.35$, the resulting distributed spring constant, $\beta = 33MPa \approx 4780ksi$. Wada et al. (1989) reported a comparable value of $\beta = 4480ksi$. Whatever values for E_c and ν are used in Equation (2-30), the resulting value of β is an order of magnitude larger than the value of β expected from Equation (2-28).

2.3 Torsional Buckling of the Inner Core

Another possible mode of buckling of the unbonded brace is the torsional buckling of the portion of the inner core that protrudes from the encasing concrete/steel tube mantel. The inelastic buckling of a cruciform has been studied extensively in the literature, due in part to the fact that calculations based on the “less respectable” total deformation theory of plasticity correlated favorably with experimental data; whereas, the calculations from the more sophisticated incremental theory of plasticity departed appreciably from experimental results (Batdorf 1949, Bijlaard 1956, Onat and Drucker 1952, Hutchinson 1974, Lubliner 1990, Bazant and Cedolin 1991). A recent study (Makris 2002), summarized herein, shows that if the flanges are slightly deflected the incremental theory of plasticity yields that the shear stress and shear strain at the onset of plastic torsional buckling are indeed related with the tangent shear modulus.

2.3.1 Elastic Buckling of the Cruciform Column

When a cruciform column under compression is sufficiently long it undergoes torsional buckling in which it twists about its vertical axis that remains straight. The critical stress can be evaluated in several ways (Timoshenko and Gere 1961). If the cruciform is not too short, the critical stress, σ_{cr} , can be evaluated by considering the equilibrium of a strip from one flange of the cruciform column as depicted in Figure 2-2 (top). Denoting by $\phi(x)$ the rotation of the cruciform at a distance, x from the origin, the deflection of the flange, $w(x, y)$ is given by

$$w(x, y) = \phi(x)y . \quad (2-31)$$

Equilibrium at the deformed configuration gives that the shearing stress, τ_{13} , is related to the normal stress $\sigma_{11} \approx \sigma$ via the expression

$$\tau_{13} = \sigma_{11} \frac{\partial}{\partial x} w(x, y) . \quad (2-32)$$

The relation between the shear and normal stresses given by Equation (2-32), and shown graphically in Figure 2-2 (bottom), has fundamental significance in this analysis because it is the key element in demonstrating that the incremental theory of plasticity yields that the shear stress and shear strain at the onset of plastic buckling due to a uniaxial compression are related to the *tangent shear modulus*.

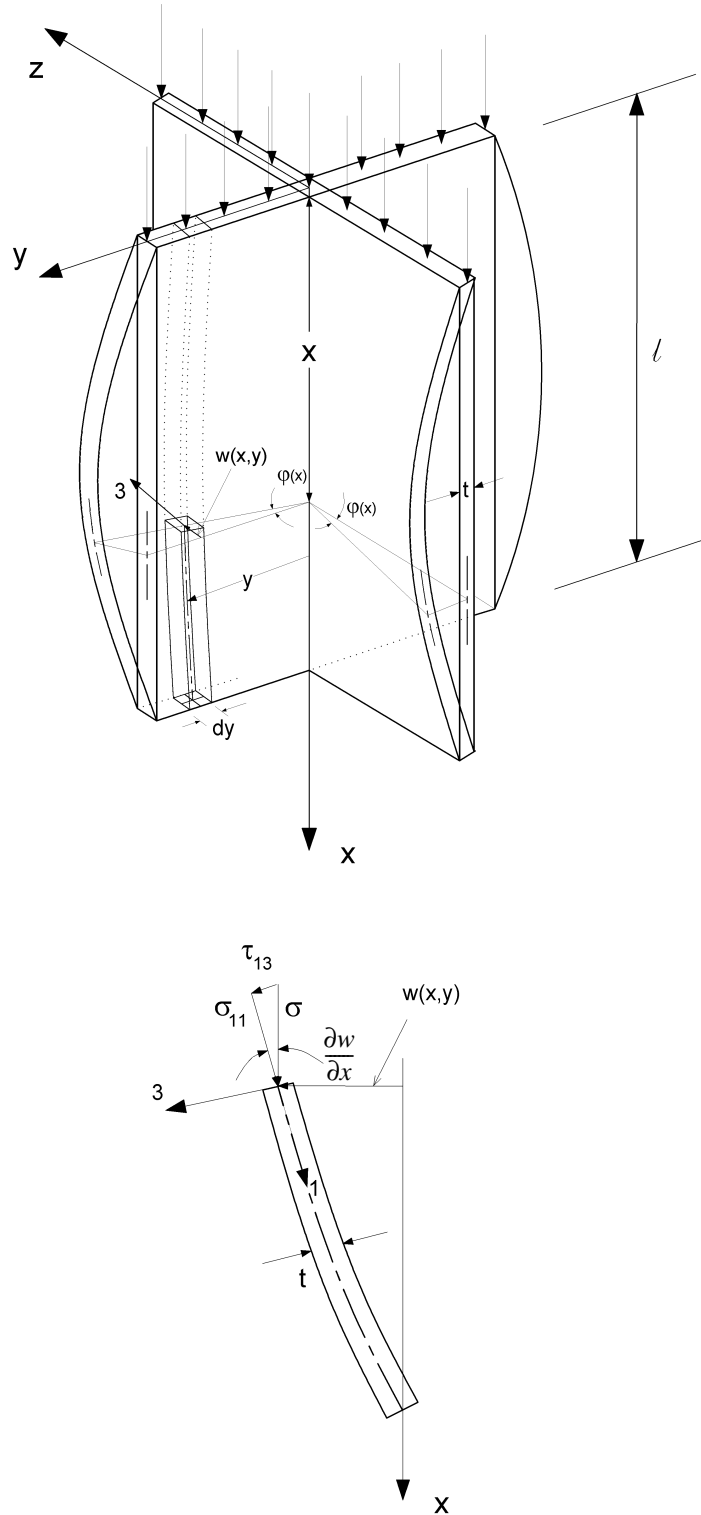


Figure 2-2. Schematic of a cruciform column under axial compression. The geometry of the flanges has bifurcated to a bent position (top). Normal and shear stresses acting on a cross section of a bent flange (bottom).

Once elastic buckling has initiated, the elementary acting torque about the vertical axis is

$$dM^A \approx \tau_{13} t y dy \approx \sigma t y \frac{\partial}{\partial x} w(x, y) dy \quad (2-33)$$

which after using Equation (2-31) and upon integration over the area of the cruciform gives

$$M^A \approx \frac{4}{3} \sigma \frac{d}{dx} \phi(x) t b^3 . \quad (2-34)$$

On the other hand, the resisting torsional moment is (Timoshenko and Gere 1961)

$$M^R = GJ \frac{d}{dx} \phi(x) = \frac{4}{3} G \frac{d}{dx} \phi(x) t^3 b , \quad (2-35)$$

where G is the elastic shear modulus, t is the thickness and b is the width of the flange plates.

Equating the acting and resisting torques given by Equations (2-34) and (2-35), the critical torsional buckling stress is given by

$$\sigma = \sigma_{cr} = G \frac{t^2}{b^2} . \quad (2-36)$$

The critical load given by Equation (2-36) is independent of the length of the protrusion, l , and can be derived by considering the equilibrium of a strip of a flange of the inner core. This consideration accounts only for the resistance of the flanges in twisting and neglects the resistance of the flanges in flexure. To obtain more accurate results, one should consider each flange as a uniformly compressed plate simply supported along three sides and free along the fourth side as shown in Figure 2-3. The differential equation for the displacement, $w(x, y)$, of a thin plate under plane compression that has assumed a bent position is

$$D \left(\frac{\partial^4 w}{\partial x^4} + 2 \frac{\partial^4 w}{\partial x^2 \partial y^2} + \frac{\partial^4 w}{\partial y^4} \right) + \sigma_n t \frac{\partial^2 w}{\partial x^2} = 0 \quad (2-37)$$

where $D = Et^3 / (12(1 - \nu^2))$ is the flexural rigidity of the plate. The solution of Equation (2-37) can be computed either with direct integration or with energy methods (Timoshenko and Gere 1961, Bleich 1952, Salmon and Johnson 1996, among others).

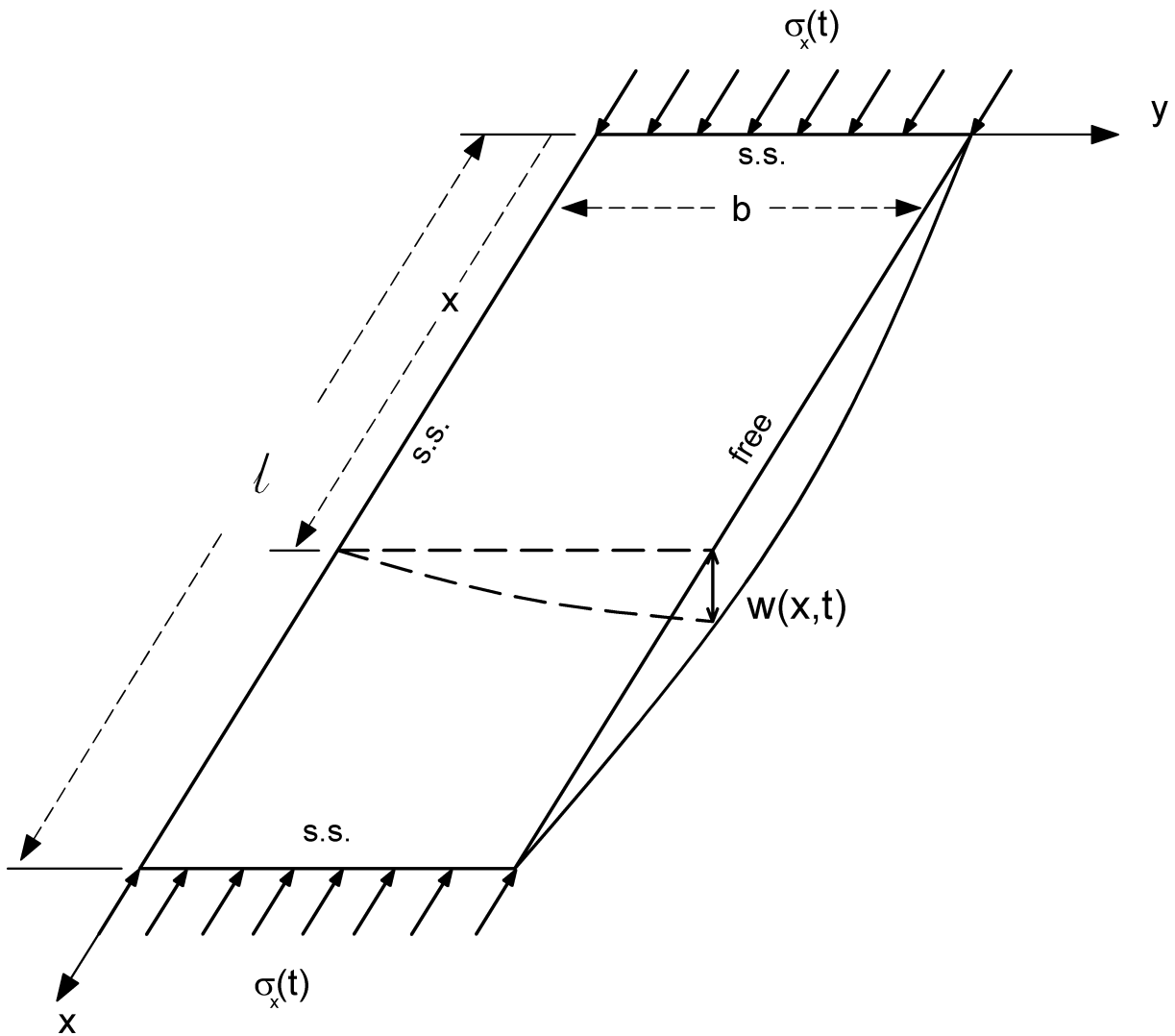


Figure 2-3. Deflected shape of a plate under plane compression with one edge free and the three other edges simply supported.

For the specific boundary conditions of the plate shown in Figure 2-3, the direct integration of Equation (2-37) yields a transcendental equation of the critical stress σ_{cr} (Timoshenko and Gere 1961). Herein the solution of Equation (2-37) is obtained by following the energy method as it allows the separate evaluation of the plate resistance due to twisting and to bending.

When the shape of the compressed plate bifurcates from the plane position to the bent position, the work done by the compressive stresses must equal the strain energy stored in the plate due to bending

$$\frac{1}{2} \iint \sigma_x t \left(\frac{\partial w}{\partial x} \right)^2 dx dy = \frac{1}{2} D \iint \left[\left(\frac{\partial^2 w}{\partial x^2} \right)^2 + \left(\frac{\partial^2 w}{\partial y^2} \right)^2 + 2\nu \frac{\partial^2 w}{\partial x^2} \frac{\partial^2 w}{\partial y^2} + 2(1-\nu) \left(\frac{\partial^2 w}{\partial x \partial y} \right)^2 \right] dx dy. \quad (2-38)$$

A simple deflected shape that satisfies the boundary conditions of the plate shown in Figure 2-3 is

$$w(x, y) = A \frac{y}{b} \sin \frac{\pi x}{l}. \quad (2-39)$$

Substituting the derivatives of Equation (2-39) into (2-38) gives

$$\sigma_x t \int_0^l \int_0^b \left(\frac{\pi y}{lb} \cos \frac{\pi x}{l} \right)^2 dx dy = D \int_0^l \int_0^b \left[\underbrace{\left(\frac{\pi^2 y}{l^2 b} \sin \frac{\pi x}{l} \right)^2}_{\text{resistance due to flexure}} + 2(1-\nu) \underbrace{\left(\frac{\pi y}{lb} \cos \frac{\pi x}{l} \right)^2}_{\text{resistance due to twisting}} \right] dx dy \quad (2-40)$$

which upon integration yields the first critical stress

$$\sigma_{cr} = \sigma_x = \frac{\pi^2 E}{12(1-\nu^2)} \frac{t^2}{b^2} \left[\frac{b^2}{l^2} + \frac{6(1-\nu)}{\pi^2} \right]. \quad (2-41)$$

For long plates where $l \gg b$, the term b^2/l^2 vanishes and Equation (2-41) reduces to

$\sigma_{cr} = \frac{E}{2(1-\nu)} \frac{t^2}{b^2}$ which is the result given by Equation (2-36). Equation (2-41) is well known in

the literature. For $\nu = 0.25$, the second term in the bracket assumes the value of 0.456 and Equation (2-41) takes the form presented by Timoshenko and Gere (1961),

$$\sigma_{cr} = \frac{\pi^2}{6(1-\nu)} G \frac{t^2}{b^2} \left[\frac{b^2}{l^2} + 0.456 \right]. \quad (2-42)$$

For $\nu = 0.3$ the second term in the bracket which corresponds to the resistance of the flange due to twisting assumes the value 0.425, which is the value that appears in the graphs of Bleich (1952) and Salmon and Johnson (1996). The elastic relationship of Equation (2-41) is rewritten in the form

$$\sigma_{cr} = \left[\frac{\pi^2 E}{12(1-\nu^2)} \frac{b^2}{l^2} + G \right] \frac{t^2}{b^2} \quad (2-43)$$

to facilitate discussion of the inelastic buckling strength of the cruciform.

2.3.2 Inelastic Buckling of the Cruciform Column

Consider now that the compressive stress, σ , is appreciable so that the cruciform column has yielded in compression and torsional buckling is imminent. Clearly the work done by the flexural moments along the flange plates (first term in the brackets of Equation (2-41)) will involve the tangent elongation modulus of the material, E_t . As the flange plates buckle they will also twist and significant shearing action is mobilized. The shearing action of the flange plates can be modeled with the total deformation theory of plasticity (Ilyushin 1947, Stowell 1948) or with the more respected incremental theory of plasticity (Handelman and Prager 1948, Onat and Drucker 1952 among others).

2.3.3 Total Deformation Theory of Plasticity

The simplest total strain theory of plasticity is usually referred to as J_2 deformation theory, where

$J_2 = \frac{1}{2} s_{ij} s_{ij}$ is the second invariant of the deviatoric stress tensor, s_{ij} , in Cartesian coordinates.

The stress deviator is $s_{ij} = \sigma_{ij} - \frac{1}{3} \sigma_{kk} \delta_{ij}$, where δ_{ij} is the Kronecker delta and the repeated indices indicate summation. In total deformation theory the total strain can be expressed as

$$\epsilon_{ij} = \frac{1+\nu}{E} \sigma_{ij} - \frac{\nu}{E} \sigma_{kk} \delta_{ij} + h(J_2) s_{ij} \quad (2-44)$$

where E is the elastic Young's modulus and ν is Poisson's ratio. The function $h(J_2)$ can be determined from a simple tension test where $\sigma_{11} \neq 0$ and $\sigma_{22} = \sigma_{33} = 0$. In this case $\epsilon_{11} = \frac{2}{3}\sigma_{11}$ and Equation (2-44) gives

$$\epsilon_{11} = \frac{\sigma_{11}}{E} + h(J_2)\frac{2}{3}\sigma_{11} . \quad (2-45)$$

By defining the secant elongation modulus of the material, $E_s = \frac{\sigma_{11}}{\epsilon_{11}}$, Equation (2-45) gives

$$h(J_2) = \frac{3}{2}\left(\frac{1}{E_s} - \frac{1}{E}\right) . \quad (2-46)$$

With the function $h(J_2)$ established (Hutchinson 1974), Equation (2-44) yields the following expression for the shear strain,

$$\epsilon_{13} = \frac{1+\nu}{E}\tau_{13} + \frac{3}{2}\left(\frac{1}{E_s} - \frac{1}{E}\right)\tau_{13} . \quad (2-47)$$

By defining the secant shear modulus of the material, $G_s = \frac{\tau_{12}}{2\epsilon_{12}}$, Equation (2-47) gives

$$G_s = \frac{E_s}{3 - (1 - 2\nu)\frac{E_s}{E}} . \quad (2-48)$$

When yielding has occurred, $\nu = 0.5$, and Equation (2-48) reduces to $G_s = \frac{E_s}{3}$. Consequently, according to a deformation theory of plasticity where $\nu = 0.5$, the critical buckling stress is given by

$$\sigma_{cr} = \frac{E_t}{3}\left[\frac{\pi^2 b^2}{3 l^2} + \frac{E_s}{E_t}\right]\frac{t^2}{b^2} . \quad (2-49)$$

The adoption of the tangent modulus E_t to express the resistance of the flange in flexure and the secant modulus E_s to express the resistance of the flange in twisting (as is expressed by equations (2-49)) has been proposed by Ilyushin (1947) and Stowell (1948) among others.

Using engineering arguments Bleich (1952) reached an expression similar to Equation (2-49) for the critical stress

$$\sigma_{cr} = \frac{\pi^2 \sqrt{EE_t}}{12(1-\nu^2)} \frac{t^2}{b^2} \left[\sqrt{\frac{E_t}{E}} \frac{b^2}{l^2} + \frac{6(1-\nu)}{\pi^2} \right] \quad (2-50)$$

which for $\nu = 0.5$ simplifies to

$$\sigma_{cr} = \frac{E_t}{3} \left[\frac{\pi^2 b^2}{3 l^2} + \sqrt{\frac{E_t}{E}} \right] \frac{t^2}{b^2} . \quad (2-51)$$

In comparing Equations (2-51) and (2-49), one observes that the solution offered by Bleich differs from the solutions of Ilyushin and Stowell only in the shearing resistance of the flange.

2.3.4 Incremental Theory of Plasticity

In an incremental or flow-type theory of plasticity the incremental strain is expressed as

$$d\varepsilon_{ij} = \frac{1+\nu}{E} d\sigma_{ij} - \frac{\nu}{E} d\sigma_{kk} \delta_{ij} + f(J_2) s_{ij} dJ_2 \quad (2-52)$$

where again $s_{ij} = \sigma_{ij} - \frac{1}{3} \sigma_{kk} \delta_{ij}$ is the stress deviator and $J_2 = \frac{1}{2} s_{ij} s_{ij}$ is the second invariant of the deviatoric stress tensor. The function $f(J_2)$ is determined from a simple tension test where $\sigma_{11} \neq 0$

and $\sigma_{22} = \sigma_{33} = 0$. In this case $s_{11} = \frac{2}{3} \sigma_{11}$, $J_2 = \frac{\sigma_{11}^2}{3}$ and $dJ_2 = \frac{2\sigma_{11}}{3} d\sigma_{11}$. With these expressions

Equation (2-52) gives

$$d\varepsilon_{11} = \frac{1}{E} d\sigma_{11} + \frac{4}{3} f(J_2) \frac{\sigma_{11}^2}{3} dJ_2 . \quad (2-53)$$

By defining the tangent elongation modulus, $E_t = \frac{d\sigma_{11}}{d\varepsilon_{11}}$ and after replacing $\frac{\sigma_{11}^2}{3}$ with J_2 , Equation

(2-53) gives

$$f(J_2) = \frac{3}{4J_2} \left[\frac{1}{E_t} - \frac{1}{E} \right] . \quad (2-54)$$

Equation (2-54) is well known in the literature (Onat and Drucker 1952, Haajer 1958, Hutchinson 1974).

Several modern monographs and books (Hutchinson 1974, Lubliner 1990, Bazant and Cedolin 1991, among others) conclude that the increments of shear stress and shear strain at the onset of plastic buckling due to a uniaxial compression are related to the elastic shear modulus; therefore, the resistance in twisting is unaffected by axially-induced plasticity—an untenable conclusion. This is indeed the result obtained by computing the tensor of the tangent elasto-plastic moduli of a perfectly straight column under axial compression (for example, Simo and Hughes 1998). The apparent shortcomings of the incremental theory of plasticity were addressed rigorously in a recent paper (Papadopoulos and Lu 1998) by way of finite elasto-plasticity based on the theory of Green and Nagdi (1965). The Papadopoulos and Lu finite element calculations showed that in reality the incremental theory of plasticity yields results which are in good agreement with experimental data and resolved the “troublesome paradox” reported by Onat and Drucker (1952).

In a recent paper the plastic torsional buckling of the cruciform was revisited by way of a simple analysis and small-strain theory (Makris 2002). It was shown analytically that for a slightly deflected flange, the incremental theory of plasticity yields that the shear stress and shear strain at the onset of plastic buckling due to a uniaxial compression are related with the *tangent shear modulus* and therefore, the resistance of the cruciform in twisting is indeed affected by plasticity.

When the flanges of the cruciform column are slightly deflected the tangent shear modulus of the column that has yielded in compression can be evaluated from Equation (2-52) in association with

(2-54). With $J_2 = \frac{\sigma_{11}^2}{3} + \tau_{13}^2$, $dJ_2 = 2\left(\frac{\sigma_{11}d\sigma_{11}}{3} + \tau_{13}d\tau_{13}\right) > 0$ and the shear strain increment according to Equation (2-52) is

$$d\varepsilon_{13} = \frac{1+\nu}{E}d\tau_{13} + \frac{3}{2J_2}\left[\frac{1}{E_t} - \frac{1}{E}\right]\tau_{13}\left(\frac{\sigma_{11}d\sigma_{11}}{3} + \tau_{13}d\tau_{13}\right). \quad (2-55)$$

Now, using that $\varepsilon_{13} \approx \frac{\partial}{\partial x}w(x, y)$, the differentiation of Equation (2-32) gives

$$d\tau_{13} = 2\sigma_{11}d\varepsilon_{13} + 2\varepsilon_{13}d\sigma_{11} \quad (2-56)$$

from which

$$d\sigma_{11} = \frac{d\tau_{13} - 2\sigma_{11}d\varepsilon_{13}}{2\varepsilon_{13}}. \quad (2-57)$$

Substitution of Equation (2-57) into (2-55) yields

$$d\varepsilon_{13} = \frac{1+\nu}{E}d\tau_{13} + \frac{3}{2J_2}\left[\frac{1}{E_t} - \frac{1}{E}\right]\left(\frac{\sigma_{11}^2}{3} + \tau_{13}^2\right)d\tau_{13} - \frac{1}{J_2}\left[\frac{1}{E_t} - \frac{1}{E}\right]\sigma_{11}^3d\varepsilon_{13}. \quad (2-58)$$

After cancelling J_2 in the second term of the right-hand side and moving the last term to the left-hand side, Equation (2-58) yields

$$\frac{d\varepsilon_{13}}{d\tau_{13}} = \frac{\frac{1+\nu}{E} + \frac{3}{2}\left[\frac{1}{E_t} - \frac{1}{E}\right]}{1 + \frac{\sigma_{11}^3}{J_2}\left[\frac{1}{E_t} - \frac{1}{E}\right]}. \quad (2-59)$$

Now, recognizing that for slightly deflected flanges yielding in compression, $\tau_{13} = \varepsilon_{13}\sigma_{11} \ll \sigma_{11}$,

therefore $\frac{\sigma_{11}^3}{J_2} \approx 3\sigma_Y$. By defining the tangent shear modulus, $G_t = \frac{d\tau_{13}}{2d\varepsilon_{13}}$, Equation (2-59) gives

$$G_t \approx \left(1 + \frac{3\sigma_Y}{E_t} - \frac{3\sigma_Y}{E}\right) \frac{E_t}{3 - (1 - 2\nu)\frac{E_t}{E}}. \quad (2-60)$$

Other than the multiplication factor in the parenthesis, Equation (2-60) is of the same form as Equation (2-48) that was derived using the total deformation theory; however now, the secant modulus, E_s is replaced with the tangent modulus, E_t . When yielding has prevailed, $\nu = 0.5$, and since $E_t \ll E$, Equation (2-60) reduces to

$$G_t \approx \left(1 + \frac{3\sigma_Y}{E_t}\right) \frac{E_t}{3}. \quad (2-61)$$

The foregoing analysis shows that for a slightly bent flange, $\frac{\partial}{\partial x}w(x, y) \neq 0$, the incremental theory of plasticity yields that at the onset of plastic torsional buckling due to axial compression, the

shear stress and the shear strain are related with the tangent shear modulus given by Equation (2-61). Consequently, according to the analysis presented herein, the critical compression stress that induces plastic torsional buckling of the cruciform column is given by Equation (2-43) after replacing E with E_t and G with G_t ,

$$\sigma_{cr} = \frac{E_t}{3} \left[\frac{\pi^2 b^2}{3 l^2} + 1 + 3 \frac{\sigma_Y}{E_t} \right] \frac{t^2}{b^2} . \quad (2-62)$$

The critical plastic buckling strength given by (2-62) was computed by examining the equilibrium of the flange at its deformed configuration—in the same manner that one computes the elastic buckling strength given by Equations (2-36) or (2-43).

Figure 2-4 (top) plots a segment of the force-displacement loop recorded during the testing of the unbonded brace. Figure 2-4 (bottom) plots the value of the critical stress, σ_{cr} , as a function of the protruding length of the cruciform, l . The two capacities shown are computed with the total and incremental theories of plasticity given by Equations (2-49) and (2-62), respectively. When the loading cycle reverses and compression initiates, the secant modulus, E_s , and the tangent modulus, E_t , are initially as high as the elastic Young's modulus of the steel $E=29,000$ ksi (right hand side of the graphs). As the compression progresses, the steel core yields and the tangent modulus, E_t , reduces more rapidly than the secant modulus, E_s . This leads to a rapid reduction of the critical stress. At the same time, as the cruciform contracts under compression the exposed/protruding length, l , reduces and the critical stress increases again. Figure 2-4 (bottom) shows that the incremental theory of plasticity (Equation (2-62)), predicts a lower capacity of the cruciform to sustain plastic torsional buckling than that given by the total deformation theory (Equation (2-49)). Figure 2-4 shows that the reduced capacity according to the incremental theory is close to the compressive stress demand that results by dividing the recorded compressive force on the inner core by its area.

Figure 2-5 shows the brace at full extension and at the onset of compression. The unsupported length of the brace shown in the figure is approximately 3.5 in. while $b/t \approx 5$. The dark region of the exposed inner core is the unbonding material that separates the inner core from the confining mortar.

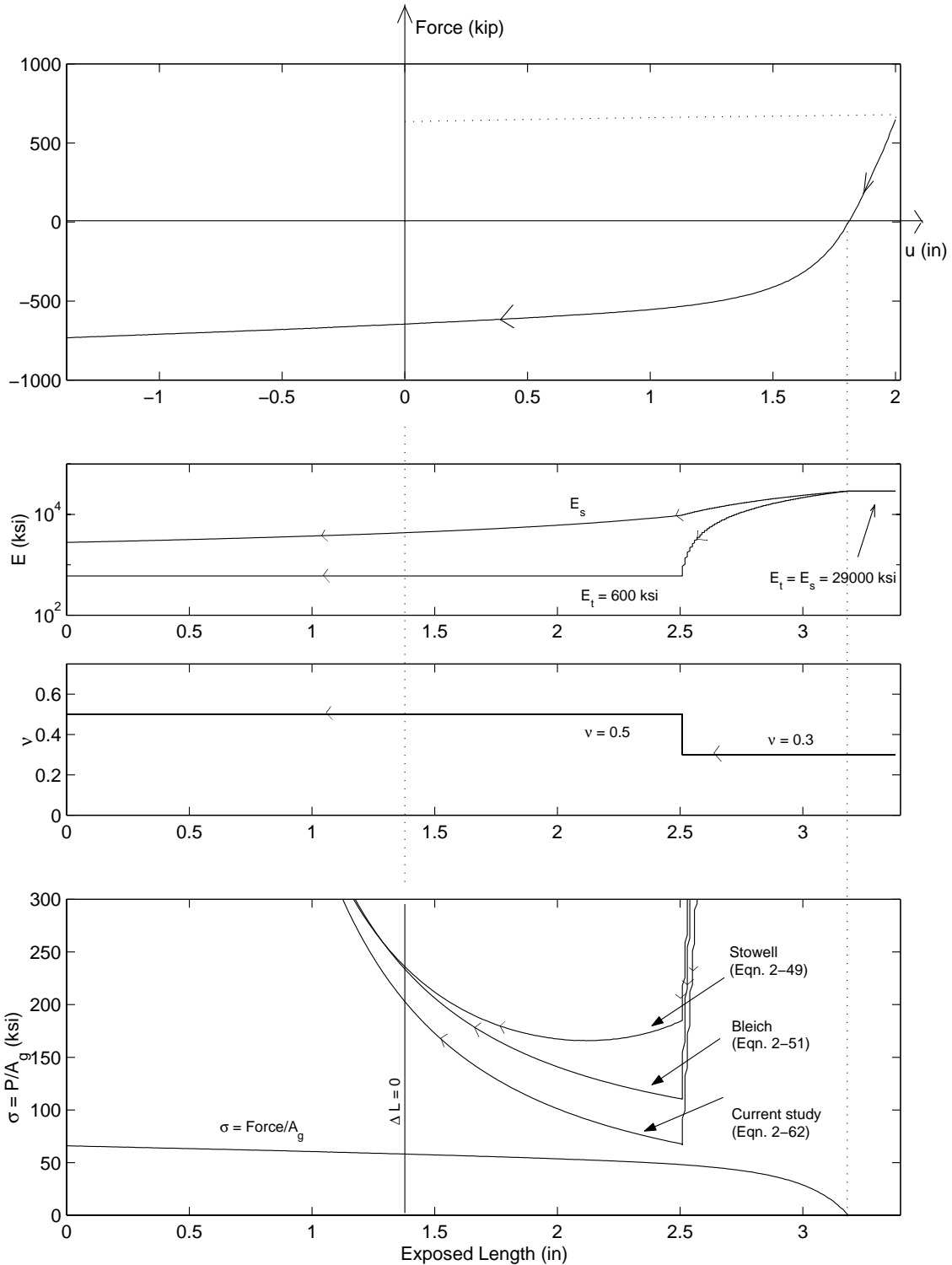


Figure 2-4. Recorded force-displacement curve (top). Values of the secant modulus, tangent modulus and Poisson ratio as the inner core contracts (center plots). Torsional buckling stresses computed with the total deformation (Equation (2-49)) and the incremental (Equation (2-62)) theories of plasticity (bottom). The results given by the intuitive formulation proposed by Bleich are also shown.

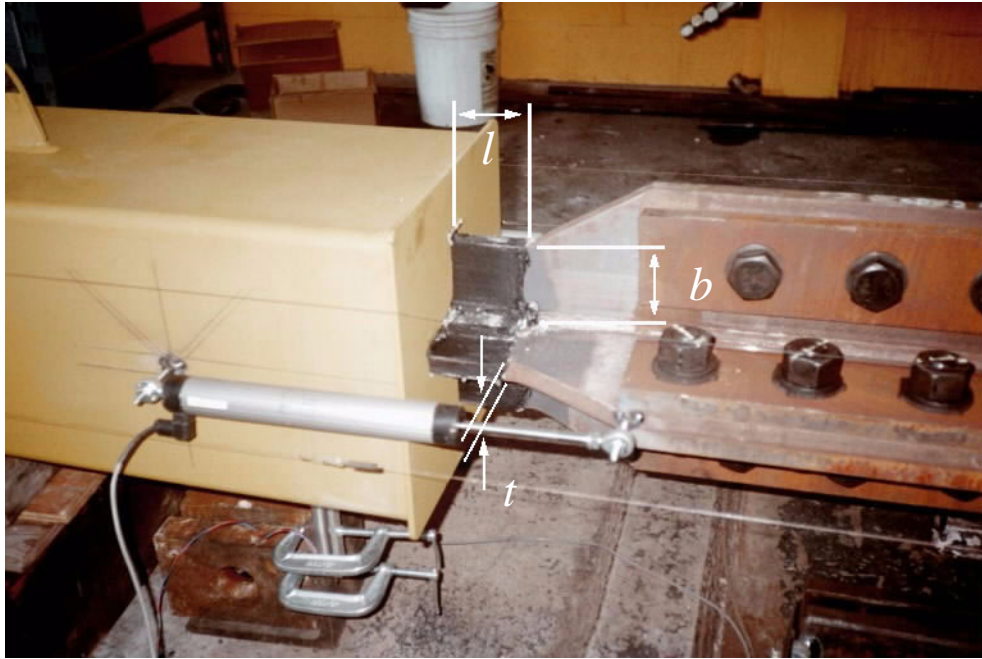


Figure 2-5. Brace at maximum elongation showing unsupported length (approximately 3.5"). The dark material covering the brace is the unbonding material layer.

3 Past Experimental Studies on Unbonded Braces

While a vast amount of proprietary test data generated by Nippon Steel Corporation in the course of their research and development of the unbonded brace have not been published, four major tests by Japanese investigators have been reported in the literature.

Watanabe et al. (1988) and subsequently Wada et al. (1989) and Watanabe et al. (1992) describe the testing of five braces conducted in Japan in the late 1980s. All of the braces tested had the same size steel core but each had a different outer tube configuration. Figure 3-1(a) presents a scale drawing of the different configurations investigated in these tests. The testing was conducted with the brace in the inclined position as shown in Figure 3-2(a). The motivation for the tests was to study the effect of various outer tube configurations and flexural capacities on the overall load capacity of the brace. The steel core material is SS41 steel according to the Japanese Industrial Standard (JIS). It has a specified minimum yield stress of $\sigma_y = 2800 \text{ kg/cm}^2$ (40 ksi). The outer tube steel is JIS TSK50 and with a specified yield stress of $\sigma_y = 3700 \text{ kg/cm}^2$ (60 ksi). The inner core was coated with a vinyl/mastic tape to accommodate the transverse expansion of the inner core. Table 3-1 summarizes the section properties, the critical loads and the yield loads of the braces tested by Watanabe et al. (1988). The yield load $P_y = \sigma_y A_i$, where σ_y is the yield stress of the inner steel core and A_i is the cross-sectional area of the core. The various outer tube configurations presented in Table 3-1 provide levels of buckling stability ranging from half the yield load of the steel core to over three times the yield load ($0.55 \leq P_e/P_y \leq 3.53$), where P_e is the Euler buckling load of the outer tube. The test results showed that the full axial load of the steel core can be developed regardless of the outer tube configuration as long as the tube provides sufficient buckling strength ($P_e/P_y > 1.0$). For the cases when the yield load of the steel core exceeded the buckling load of the outer tube, the brace failed in a global buckling mode.

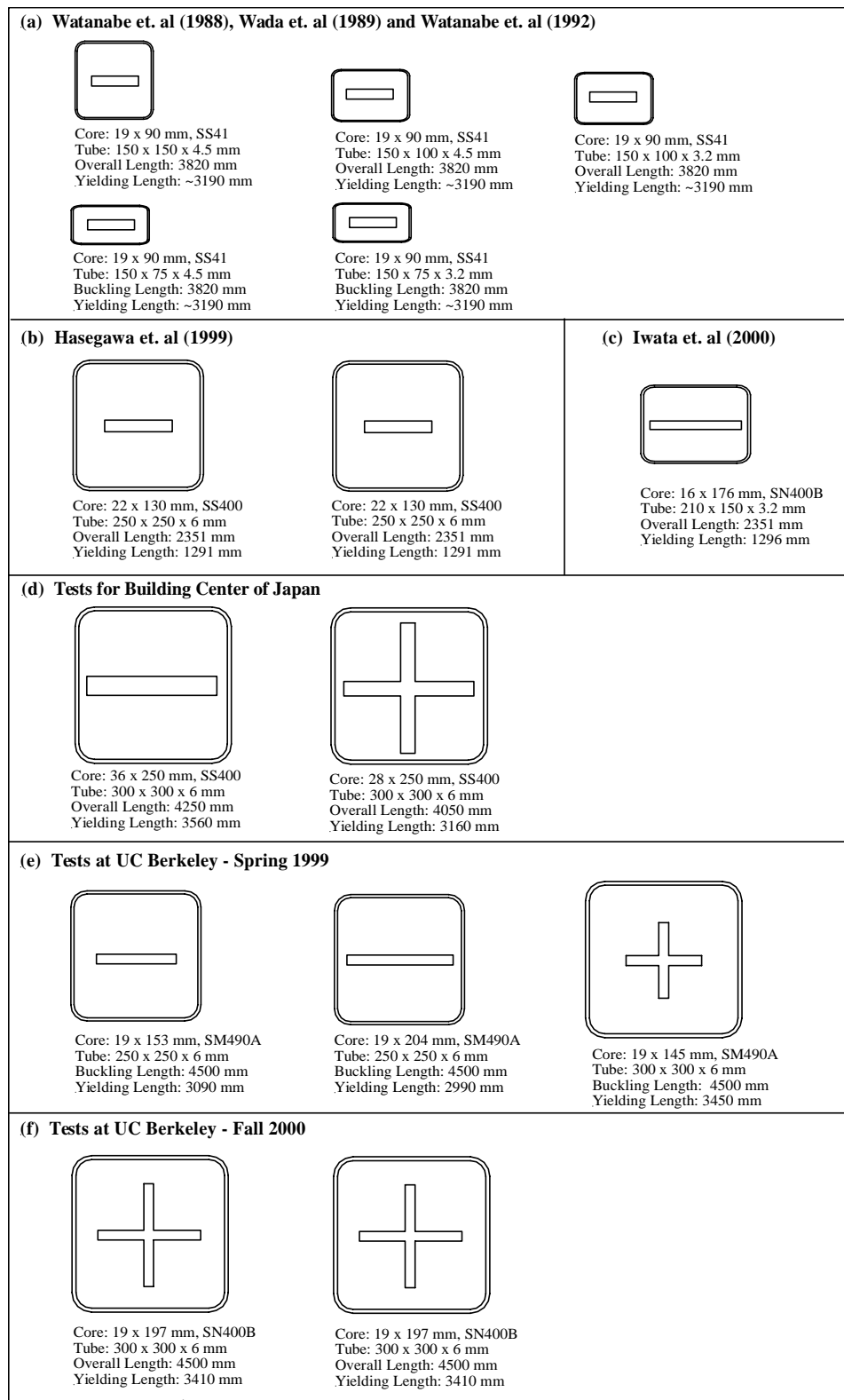
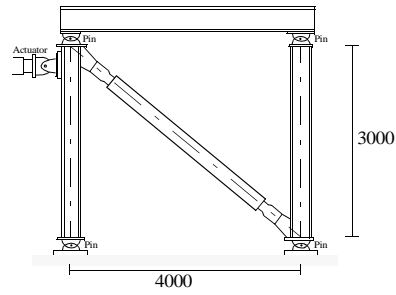
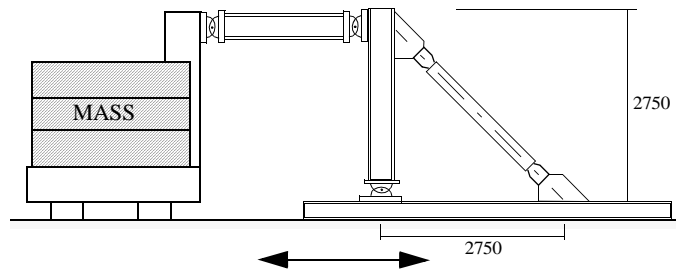


Figure 3-1. Unbonded braces tested in Japan (figures a through d) and at UC Berkeley (figures e and f). Brace sizes are shown to scale.

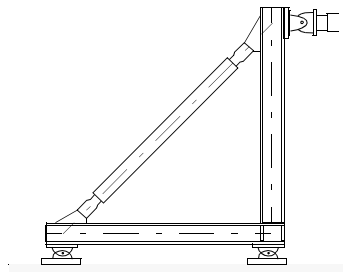
(a) Watanabe et al. (1988), Wada et al. (1989) and Watanabe et al. (1992)



(b) Hasegawa et al. (1999)



(c) Konomi et al. (1999)



(d) Iwata et al. (2000)

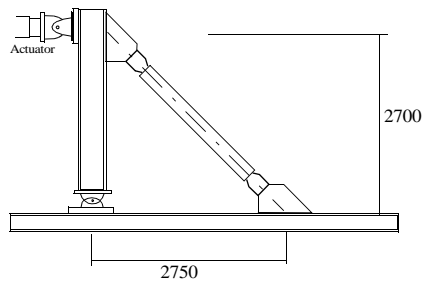


Figure 3-2. Previous testing configurations.

Table 3-1. Comparison of unbonded braces tested (Watanabe et al. (1988), Wada et al. (1989) and Watanabe et al. (1992))

Specimen No.	Core Member				Outer Tube		
	$b \times t$ (mm)	Cross-sectional Area, A (mm ²)	Yield Load, P_y (KN)	Local Buckling $P_m = 2\sqrt{\beta EI_o}$ ($\beta = 4500ksi$) (KN)	Tube Dimension B x D x T (mm)	Buckling Load, P_e (KN)	$\frac{P_e}{P_y}$
1	90 x 19	1684	476	1625	150 x 150 x 4.5	1677	3.53
2	90 x 19	1684	476	1625	150 x 100 x 4.5	661	1.39
3	90 x 19	1688	477	1625	150 x 100 x 3.2	492	1.03
4	90 x 19	1684	476	1625	150 x 75 x 4.5	343	0.72
5	90 x 19	1662	469	1625	150 x 75 x 3.2	257	0.55

Figure 3-3 summarizes the computed elastic buckling curves of the braces tested by Watanabe et al. (1988). The critical load is obtained from Euler buckling (Equation (2-6)), with E being the elastic modulus of the outer tube. The contributions of the encasing mortar and the steel core to the buckling resistance of the brace have been neglected.

Hasegawa et al. (1999) describe shake table testing of two braces (Figure 3-1(b)). These tests were conducted in Japan in the 1990s. For these tests, the brace was inclined with one end of the brace attached to the shake table and the other attached to the top of a vertical column pinned to the shake table (Figure 3-2(b)). The dynamic force applied to the test brace was generated by accelerating a large mass which rested on isolators and was attached to the vertical column through a rigid horizontal link. The earthquakes used were the Kobe Marine Observatory Record from the 1995 Kobe and the 1940 El Centro, earthquake records. Each earthquake record was scaled to produce desired velocity levels ranging from 5 cm/sec to 90 cm/sec. For this brace configuration the ultimate level corresponds to an axial strain of 7.2 percent which was achieved at an equivalent story deformation angle of 1/20. The authors report that the braces exhibited stable hysteresis throughout the testing.

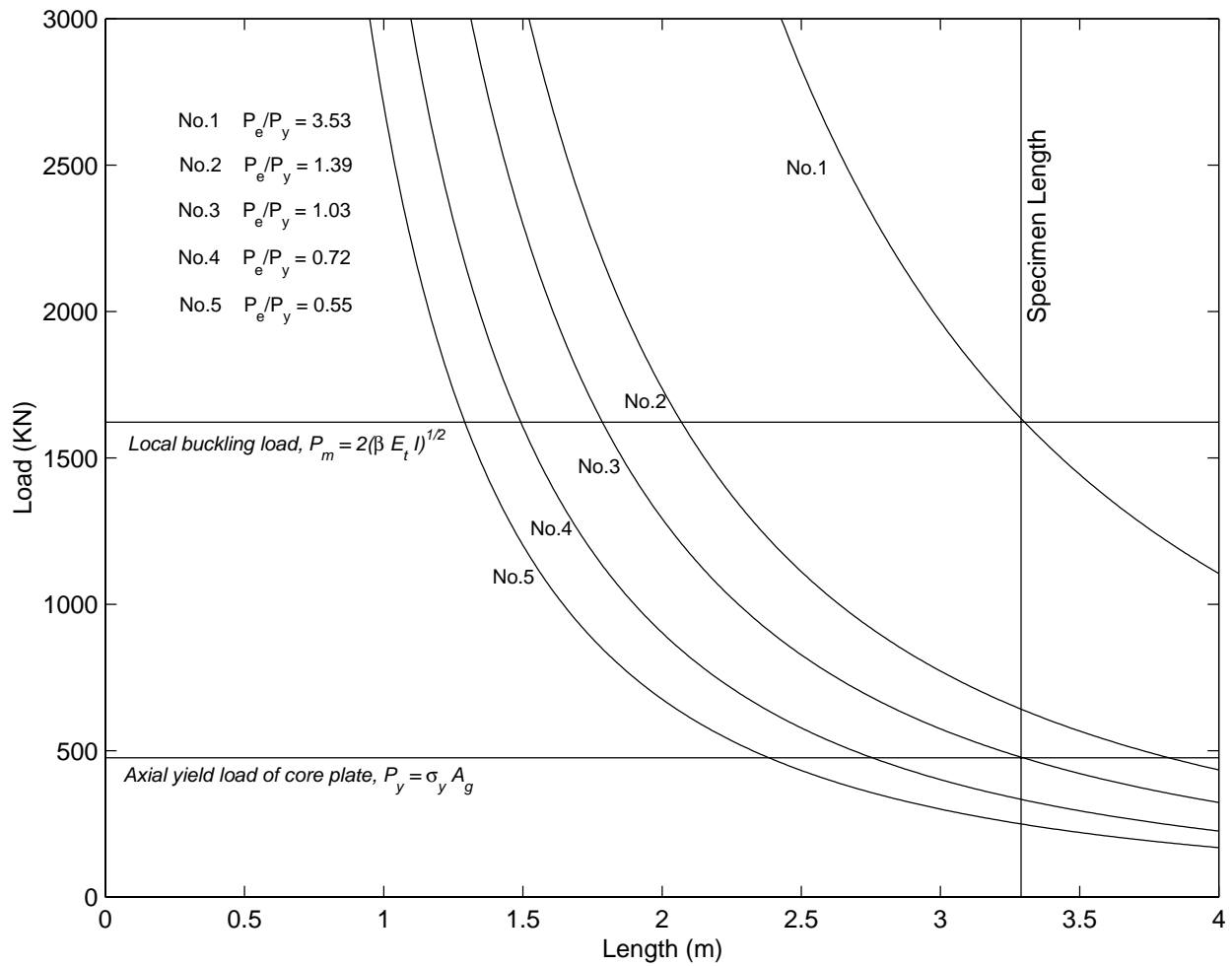


Figure 3-3. Euler buckling curves of five unbonded braces that have the same inner core (19x90 mm) but different outer tube sizes tested by Watanabe et al. (1988), Wada et al. (1989) and Watanabe et al. (1992).

Konami et al. (1999) describe extensive testing of 12 unbonded braces. These tests were conducted in Japan in the mid-to-late 1990s. The brittle fracture of moment connections observed after the 1994 Northridge and 1995 Kobe earthquakes demonstrated that welded connections are not always capable of achieving their full capacities and adequately absorbing seismic energy through plastic deformation. The motivation for the study reported by Konami et al. (1999) was to investigate the effect of adding elements to moment-resisting frames which are specifically included to dissipate energy hysterically through plastic deformation to moment-resisting frames. Two moment-resisting frames were tested — one with and one without an unbonded brace. To make meaningful comparisons, the beam and column sizes of the braced moment-resisting frame were chosen such that the yield load of both frames was the same. In addition to the tests performed in the partial frame configuration (Figure 3-2(c)), braces were also tested in pure axial loading. The same loading applied in the partial frame configuration was applied in the brace axial direction based on the output obtained from the displacement measured during the partial frame tests. By comparing the response of the frame with the unbonded brace and the brace alone, it was concluded that the braces provided nearly all of the energy dissipation in the system and that the effect of the brace end moments present in the frame configurations had little effect on the performance of the brace. The authors also reported that for loading to equivalent levels of displacement, the energy dissipated by the frame with the unbonded brace was much greater than that of the frame without the brace.

Iwata et al. (2000) describe tests which compared four commercially available types of buckling-restrained braces. The testing was conducted with the braces in an inclined configuration, as shown in Figure 3-2(d). All the braces tested had the same steel core area (yield force) and approximately the same buckling capacity. Of the four configurations tested one was an unbonded brace (Figure 3-1(c)). It is reported that all braces behaved well up to 1 percent strain but at larger strain levels, the unbonded brace behaved the most favorably.

A number of tests of unbonded braces have been conducted by the Building Center of Japan. Although not much information is available on the testing protocol or results, the brace cross sections are shown in Figure 3-1(d). Figures 3-1(e) and 3-1(f) show the cross section of the braces tested at UC Berkeley.

4 Component Testing of Unbonded Braces

4.1 Description of Braces

The first tests of the unbonded brace in the United States were conducted at UC Berkeley during the spring of 1999 and fall of 2000. The geometrical characteristics and the critical loads of these braces are summarized in Table 4-1 and the Euler buckling curves are shown in Figure 4-1. The

Table 4-1. Unbonded braces tested at UC Berkeley in spring 1999 and fall 2000

Specimen	Steel Core					Outer Tube			
	Cross section Type and Dimension	Area	Yield Length	Steel Grade and Yield Stress ^a	P_y	Cross Section	Length	Steel Grade and Yield Stress	$P_{cr} = P_e$ (Pinned End ^b)
	mm (in)	mm ² (in ²)	mm (in)	MPa (ksi)	kN (kips)	mm (in)	mm (in)	MPa (ksi)	kN (kips)
UC Davis Plant and Environmental Sciences Building (Spring 1999)									
99-1	(-) 19 x 153 (3/4 x 6)	2,907 (4.5)	3,090 (121.7)	JIS SM490A 418.5 (60.7)	1,217 (273.2)	250 x 250 x 6 (9.8 x 9.8 x 0.24)	3,390 (133.5)	JIS STKR400 317.2 (46)	5,666 (1,273)
99-2	(-) 19 x 204 (3/4 x 8)	3,876 (6.0)	2,990 (117.7)	JIS SM490A 418.5 (60.7)	1,622 (364.2)	250 x 250 x 6 (9.8 x 9.8 x 0.24)	3,390 (133.5)	JIS STKR400 317.2 (46)	5,666 (1,273)
99-3	(+) 19 x 145 (3/4 x 5.71)	5,149 (8.0)	3,450 (135.8)	JIS SM490A 418.5 (60.7)	2,155 (485.6)	300 x 300 x 6 (9.8 x 9.8 x 0.24)	3,390 (133.5)	JIS STKR400 317.2 (46)	9,910 (2,228)
Kaiser Santa Clara Medical Center (Fall 2000)									
00-11	(+) 19 x 197 (3/4 x 7-3/4)	7,125 (11.04)	3,410 (134.3)	JIS SN400B 285.4 (41.1)	2,033 (453.7)	300 x 300 x 6 (9.8 x 9.8 x 0.24)	3,340 (131.5)	JIS STKR400 317.2 (46)	9,910 (2,228)
00-12	(+) 19 x 197 (3/4 x 7-3/4)	7,125 (11.04)	3,410 (134.3)	JIS SN400B 285.4 (41.1)	2,033 (453.7)	300 x 300 x 6 (9.8 x 9.8 x 0.24)	3,340 (131.5)	JIS STKR400 317.2 (46)	9,910 (2,228)

a. Value obtained from coupon test of steel core material

b. Buckling length taken as total end-to-end length of steel core — 4500 mm for all specimens

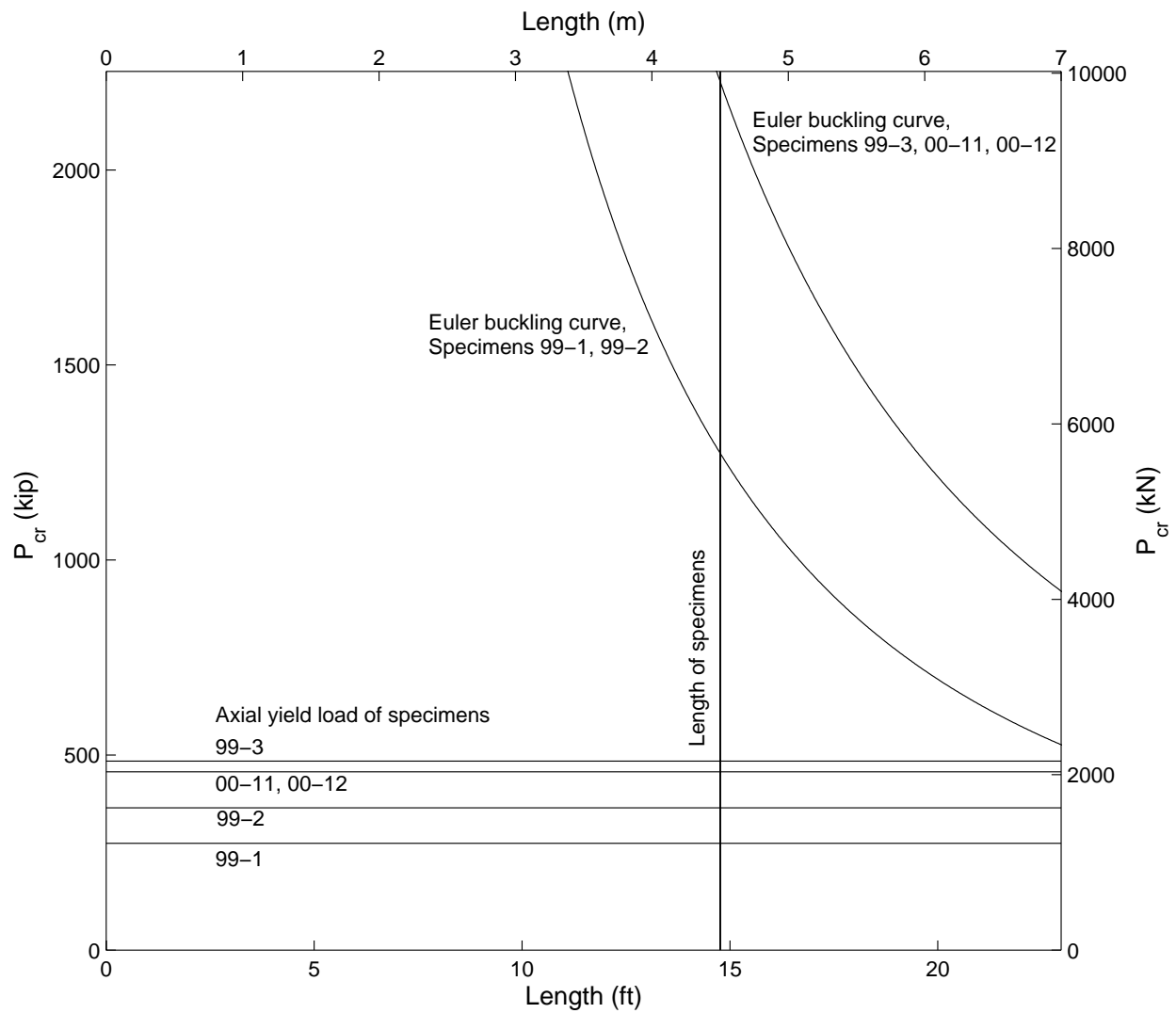


Figure 4-1. Euler buckling curves for the specimens tested at UC Berkeley. Lines indicating the steel core axial yield loads are included for comparison.

three unbonded braces tested in spring 1999 (Specimens 99-1, 99-2 and 99-3) are representative of unbonded braces designed for the UC Davis Plant and Environmental Science Building. Two of the specimens had steel core members with rectangular cross sections and one specimen had a cruciform cross section. All core members consist of Japanese Industrial Standard (JIS) grade SM490A which is similar to ASTM A572/50 with a nominal yield stress of 45.7 ksi. The tube steel was JIS grade STKR400, a steel grade similar to ASTM 500. The unbonded braces tested in fall 2000 (Specimens 00-11 and 00-12) are representative of the braces designed for the Kaiser Santa Clara Medical Center. The specimens tested had identical cruciform core members of JIS grade SN400B steel with $34.1 \text{ ksi} \leq \sigma_y \leq 51.5 \text{ ksi}$. The tube steel was JIS STKR400. Figures 4-2 through 4-5 present schematic drawings of the unbonded braces tested at UC Berkeley.

The design of the bolted connection for the test specimens was identical to the braces in the actual structures. The bolts were 1-inch diameter, ASTM grade A490 and the splice plates were JIS grade SM490A steel which is approximately equivalent to ASTM A572/50. The connections were slip-critical and thus it was important to ensure that correct bolt tightening force was achieved.

4.2 Experimental Setup

The spring 1999 tests were conducted at the UC Berkeley Department of Civil and Environmental Engineering Structures Laboratory in Davis Hall, and the fall 2000 tests were conducted at the Richmond Field Station of the University of California, Berkeley. Both series of tests comprised two reaction frames anchored to the laboratory strong floor. A hydraulic actuator with a capacity of 1000 kips in compression and 700 kips in tension was used for cyclic loading of the test specimens. The actuator had a displacement capacity of +/- 6 in., and was displacement-controlled via a linear variable displacement transducer mounted on the actuator. The test set-up was designed so that there was no slip between the reaction frames and the laboratory floor. Figure 4-6 shows a schematic diagram of the experimental setup used for both tests, while Figure 4-7 shows views of the experimental setup used for the fall 2000 tests.

4.3 Instrumentation

The force and displacement quantities of interest were measured with a digital data acquisition system. The force was measured via an in-line load cell and the ten displacements of interest were measured with wire potentiometers and direct current displacement transducers. Figure 4-8 shows a schematic diagram of the displacement instrumentation for the spring 1999 tests (top) and the fall 2000 test (bottom). It consists of

- Four Novotechnik LWG 150 ± 3 in. stick potentiometers (accuracy 0.1 percent full scale), two at each end of the test specimen (one on each side of the tube in a horizontal plane), to measure the relative displacement between the steel core that protrudes from the end of the tube and the end of the tube itself (channels 7 – 10 in Figure 4-8).
- Two Celesco PT 101-15A ± 15 in. wire potentiometers (accuracy 0.1 percent full scale), one on each side of the brace in a horizontal plane, to measure the relative displacement between the two ends of the steel core (channels 1 and 2 in Figure 4-8).
- Two Celesco PT 101-15A ± 15 in. wire potentiometers (accuracy 0.1 percent full scale), one on each side of the test specimen in a horizontal plane, to measure the relative displacement between the left-hand end and right-hand end connection pieces to which the test specimen was bolted (channels 3 and 4 in Figure 4-8).
- Two displacement transducers located at the mid-point of the test specimen, one horizontally and one vertically, to measure the out-of-plane movement of the outer tube during loading (channels 5 and 6 in Figure 4-8). Spring 1999: Two Novotechnik TRS 50A 502 ± 1 in. stick potentiometers (accuracy 0.1 percent full-scale). Fall 2000: Two Trans Tek 243-000 ± 0.5 in. direct current differential transformers (accuracy 0.5 percent full scale).

4.4 Testing Protocols

Both the spring 1999 and fall 2000 test programs consisted of two phases. First, each brace was subjected to a standard loading protocol that was agreed on by the design engineers of the UC Davis Plant and Environmental Services Building for the spring 1999 tests and the Office of Statewide Health, Planning and Development (OSHPD) for the fall 2000 tests. These tests were followed by additional tests including large-deformation, low-cycle fatigue tests and simulated earthquake displacement tests.

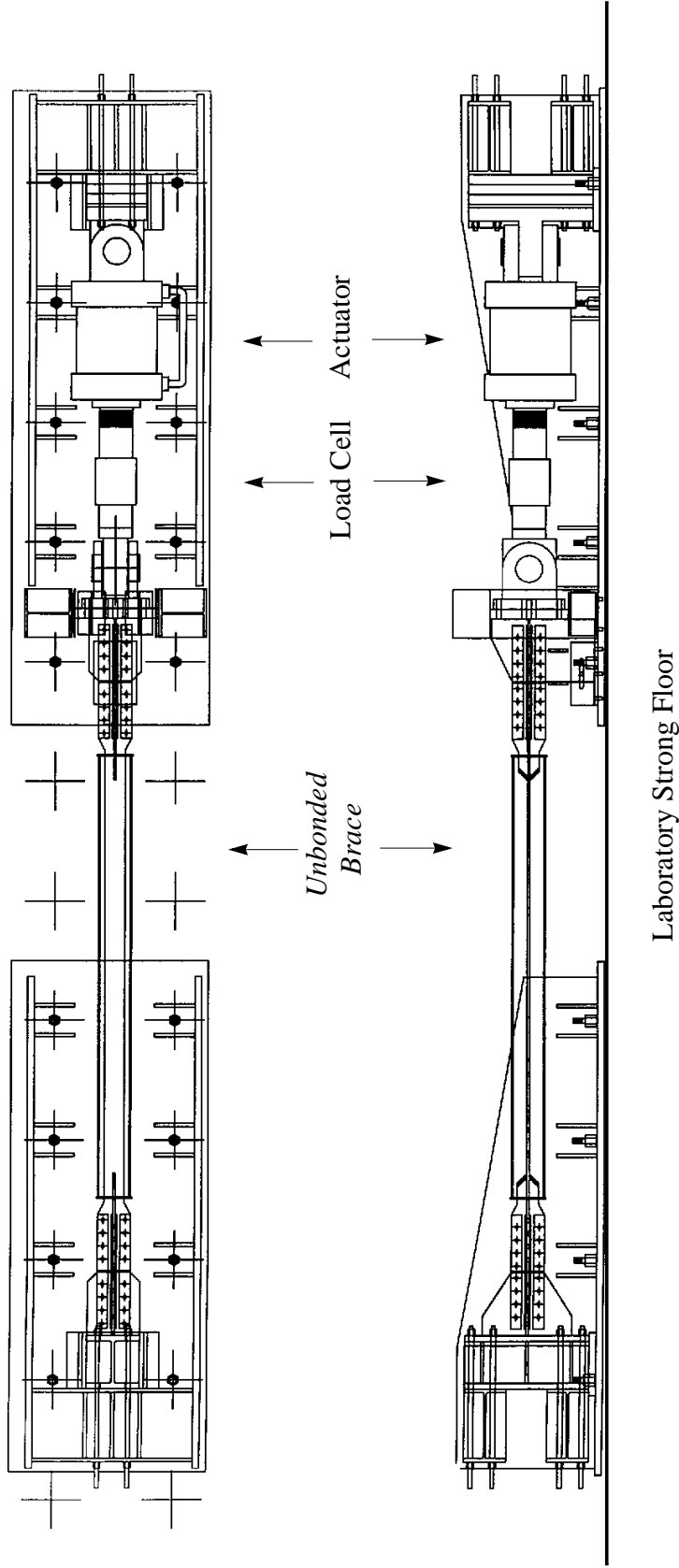


Figure 4-6. Plan and elevation views of the setup for unbonded brace test.



Figure 4-7. Views of the unbonded brace mounted on the fall 2000 test setup.

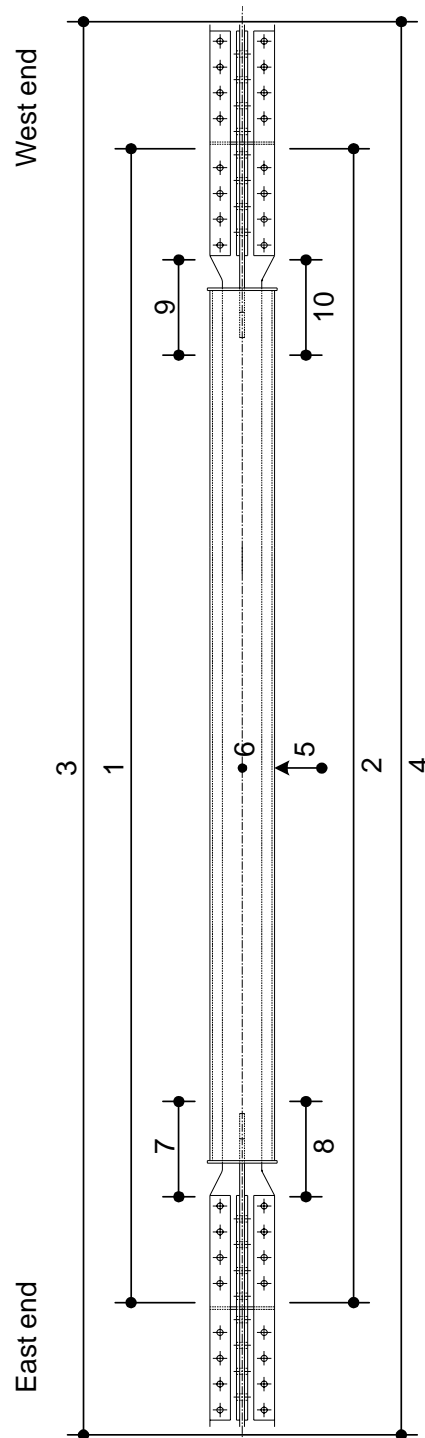
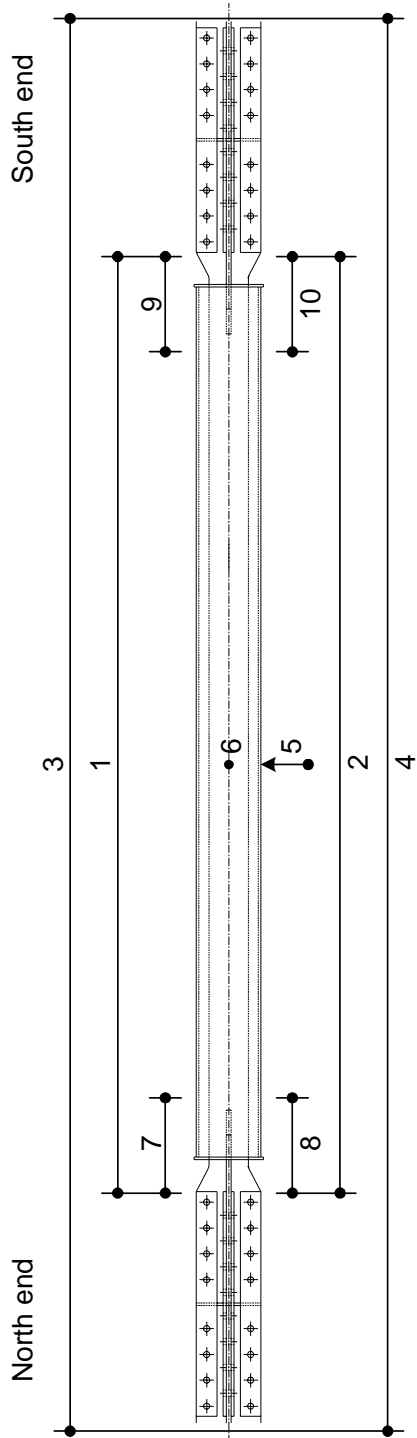


Figure 4-8. Location of potentiometers that measure brace displacements for spring 1999 tests (top) and fall 2000 tests (bottom).

4.4.1 Spring 1999 Test Protocol

Two phases of testing were conducted on each of the three specimens tested in spring 1999. The first phase consisted of a sequence of cyclic tests as recommended by SAC¹ for the testing of welded steel moment connections. This sequence of tests is referred to as the *SAC basic loading history*. The primary parameter used to define the test program was the brace cyclic axial displacement (strain). These quantities were determined to correspond to specific building interstory drift ratios in accordance with the SAC basic loading history. The tests consisted of pre- and post-yield fully reversed saw-tooth displacement cycles. The specific details of the SAC basic loading history for each specimen are given in Table 4-2 and a typical displacement history is shown in Figure 4-9.

Table 4-2. SAC basic loading history for spring 1999 test specimens

Test Number	Amplitude Specimen 99-1 [inch]	Amplitude Specimen 99-2 [inch]	Amplitude Specimen 99-3 [inch]	Max. Brace Strain [%]	Story Drift Ratio [%]	No. of Cycles	Comments
a	± 0.07	± 0.06	± 0.07	0.06	-	2	elastic (0.25 x dy)
b	± 0.13	± 0.12	± 0.14	0.11	-	2	elastic (0.50 x dy)
c	± 0.19	± 0.18	± 0.21	0.16	-	2	elastic (0.75 x dy)
1	± 0.31	± 0.30	± 0.35	0.26	0.375	6	brace ductility = 1.25
2	± 0.42	± 0.41	± 0.47	0.35	0.50	6	brace ductility = 1.67
3	± 0.63	± 0.61	± 0.70	0.52	0.75	6	brace ductility = 2.5
4	± 0.84	± 0.81	± 0.94	0.69	1.0	4	brace ductility = 3.3
5	± 1.26	± 1.22	± 1.41	1.04	1.5	2	brace ductility = 5.0
6	± 1.67	± 1.62	± 1.87	1.38	2.0	2	brace ductility = 6.7
7	± 2.51	± 2.44	± 2.81	2.07	3.0	2	brace ductility = 10.0

1. SAC Joint Venture (a partnership of: Structural Engineers Association of California, Applied Technology Council, California Universities for Research in Earthquake Engineering), *A Program to Reduce the Earthquake Hazards of Steel Moment Frame Structures*, funded by the Federal Emergency Management Agency.

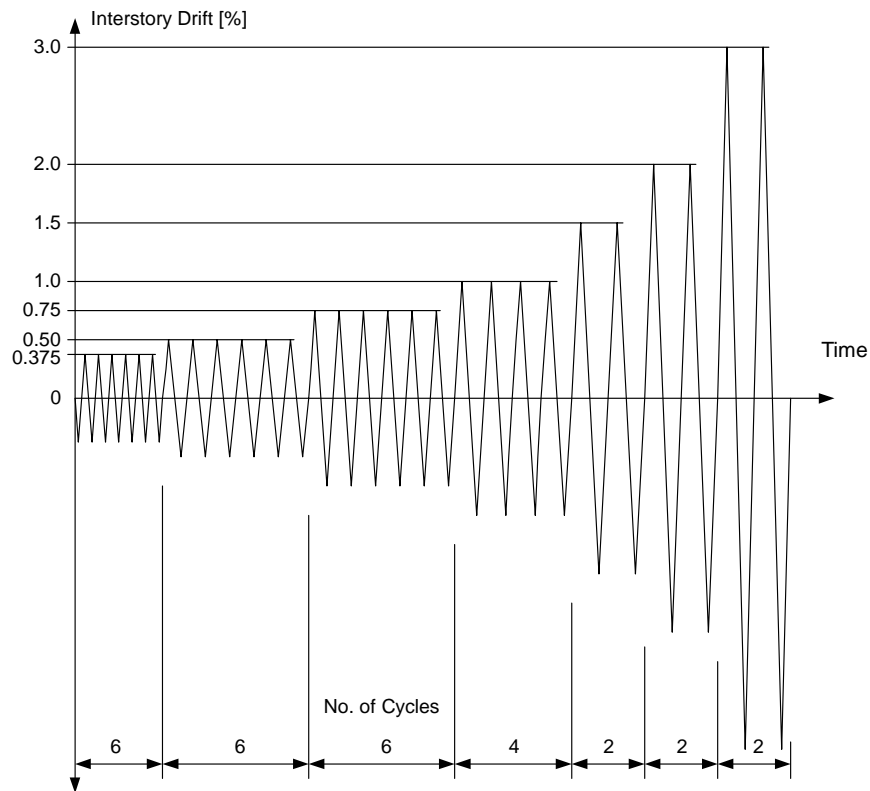


Figure 4-9. SAC basic loading history used for spring 1999 test specimens.

Specimen 99-1

Following the SAC basic loading history Specimen 99-1 was subjected to the *SAC near-field loading history* which consists of one-half cycle to a displacement corresponding to two percent story drift, a half-cycle reversal to an offset of four percent story drift in the opposite direction, followed by three fully reversed cycles corresponding to an amplitude of two percent story drift about the offset position. The details of this loading history are shown in Figure 4-10.

Specimen 99-2

For Specimen 99-2, the SAC basic loading history was followed by a large-deformation, low-cycle fatigue test consisting of fully reversed displacement cycles at an amplitude of 2.44 in. (corresponding to 3 percent story drift) as shown in Figure 4-11.

Specimen 99-3

In addition to the SAC basic loading history, Specimen 99-3 was subjected to earthquake displacement histories derived from the interstory drift of a typical building subjected to earthquake

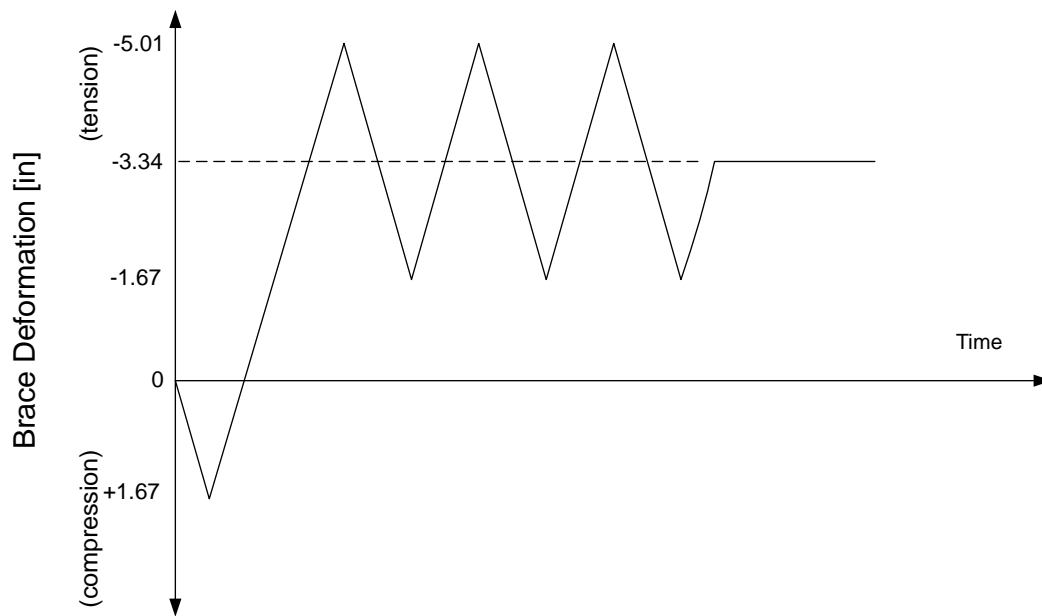


Figure 4-10. SAC near-field loading protocol imposed on Specimen 99-1.

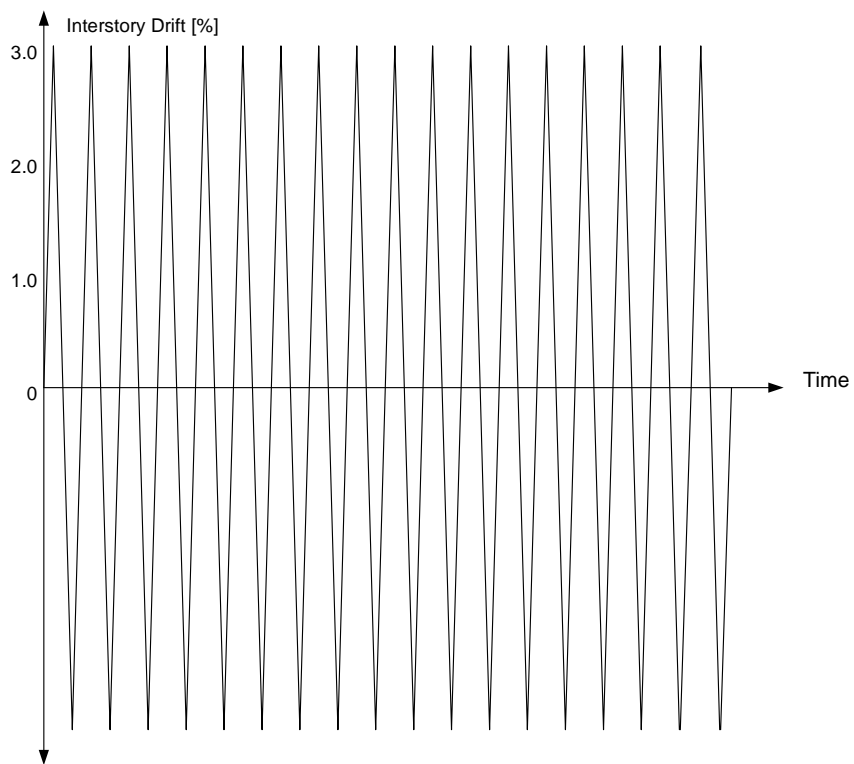


Figure 4-11. Low-cycle fatigue test imposed on Specimen 99-2.

loading. The earthquake motions shown in Figure 4-12 were derived from the nonlinear analysis of an idealized five-story steel building with unbonded braces, subjected to the 1994 Sylmar N-S and the 1940 El Centro N-S ground motions. The computed interstory displacement time histories were subsequently scaled up to produce a displacement record with a maximum value approximately equal to the maximum displacement capacity of the specimen. It is worth mentioning that (a) each computed displacement history was applied to the specimen at a reduced rate of loading, such that the 10-sec-long earthquake was stretched to a 100-sec duration to compensate for the dynamic response limitations of the servo-hydraulic system and (b) the displacement histories as shown do not start at zero, rather the tests began with zero load applied to the specimen.

4.4.2 Fall 2000 Test Protocol

The two specimens tested in the fall of 2000 were subjected to a loading program consisting of increasing amplitude elastic and post-yield cycles of displacement, similar to the SAC basic loading history used for the spring 1999 tests. This brace loading history, referred to as the OSHPD brace loading history, was designed to subject the test specimens to maximum deformations and cumulative plastic deformations that exceeded the largest earthquake considered in the design of the Kaiser Santa Clara Medical Center. The primary parameter used to define the test program was the brace cyclic axial strain. The strains used to define the protocol correspond to building interstory drift ratios of 0.5, 1.0, 1.5, 2.0 and 2.25 percent. The loading sequence is detailed in Table 4-3 and shown in Figure 4-13. The acceptance criteria established to evaluate the adequacy of the brace behavior are summarized in Appendix A.

In addition to the OSHPD brace loading history, one specimen was subjected to a low-cycle fatigue test similar to the one conducted in the spring 1999 test (shown in Figure 4-11) with an amplitude corresponding to 1 percent story drift, while the other specimen was subjected to two earthquake-induced displacement histories. The histories (shown in Figure 4-14) were derived from nonlinear dynamic analyses performed as part of the project design and were representative of the most severe displacement histories for the 10 percent in 50 year, Design Basis Earthquake (DBE) and the 10 percent in 100 year, Upper Bound Earthquake (UBE) analyses.

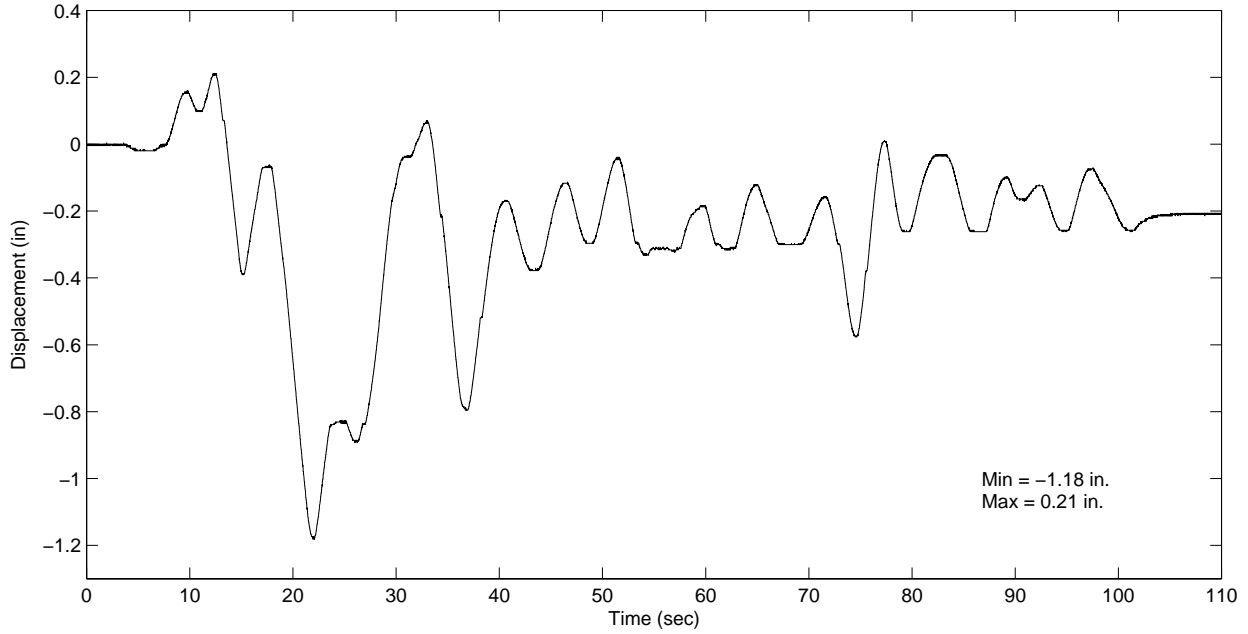
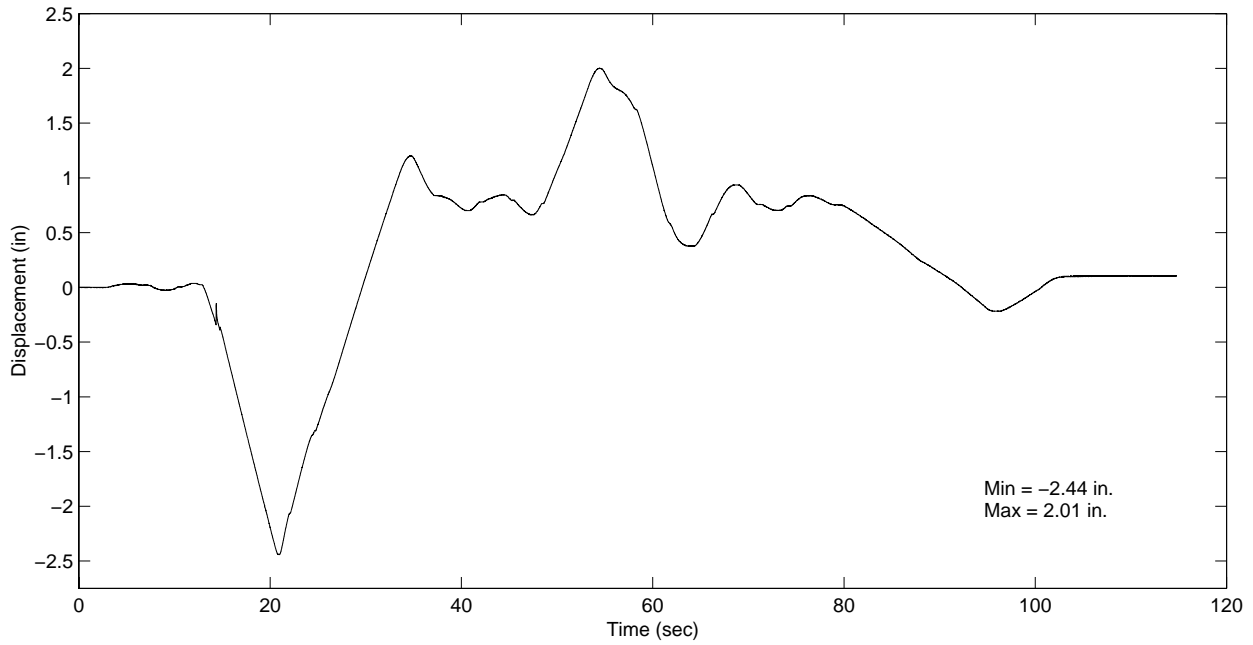


Figure 4-12. Brace displacement histories computed for an idealized five-story building that is subjected to the 1994 Sylmar record (top) and the 1940 El Centro record (bottom). These histories were used as displacement histories on Specimen 99-3.

Table 4-3. OSHPD brace loading history for fall 2000 test specimens

Test Number	Amplitude [inch]	Maximum Brace Strain [%]	Story Drift Ratio [%]	Number of Cycles	Comments
a	± 0.046	0.035	-	2	elastic, = 0.25 x d _y
b	± 0.093	0.069	-	2	elastic, = 0.50 x d _y
c	± 0.139	0.104	-	2	elastic, = 0.75 x d _y
d	± 0.185	0.138	-	2	to yield, 1.0 x d _y
1	± 0.62	0.46	0.5	2	brace ductility = 3.3
2	± 1.23	0.92	1.0	2	brace ductility = 6.7
3	± 1.85	1.38	1.5	2	brace ductility = 10.0
4	± 2.47	1.84	2.0	2	brace ductility = 13.3
5	± 2.76	2.07	2.25	2	brace ductility = 15.0

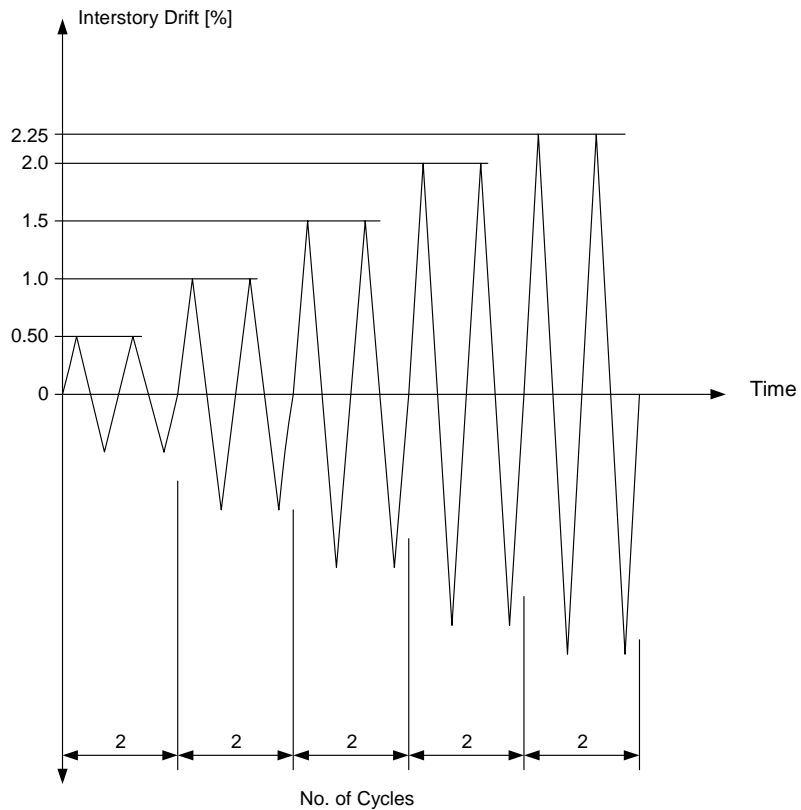


Figure 4-13. OSHPD brace loading history for fall 2000 test specimens.

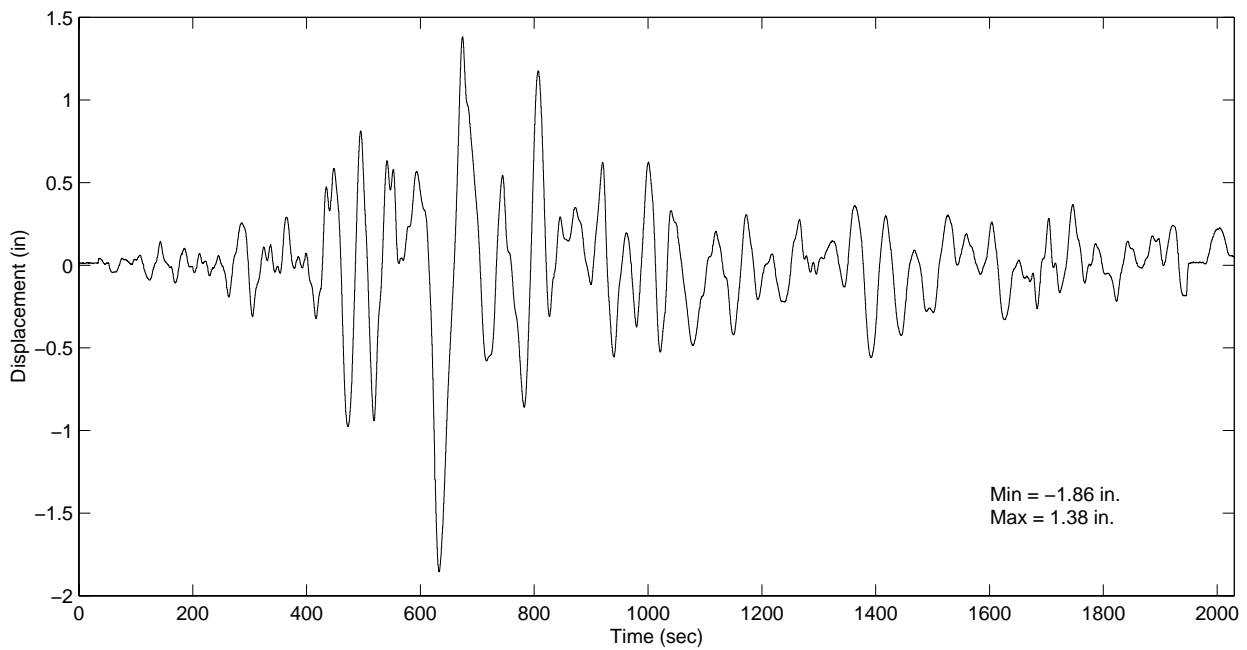
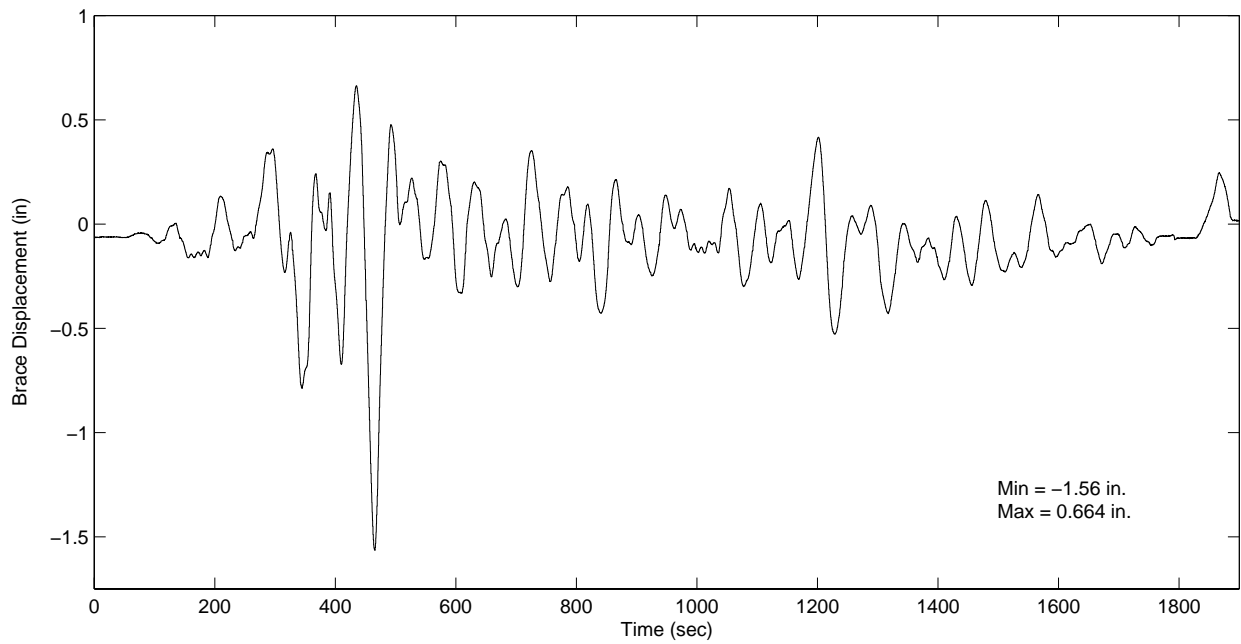


Figure 4-14. Drift-induced displacement histories determined from nonlinear structural analyses of a steel structure. They are representative of the most severe brace displacement histories for the Design Basis Earthquake (top) and Upper Bound Earthquake (bottom) used in the design of the Kaiser Santa Clara Medical Center.

4.5 Experimental Results

4.5.1 Spring 1999 Test Results

Results from the spring 1999 tests are presented in Figures 4-15 through 4-21. For each test, or set of tests, the imposed relative end displacement history is shown above the corresponding measured force-displacement loops.

Specimen 99-1

Figure 4-15 (top) shows the SAC basic loading history. Figure 4-15 (center) plots the recorded force in the brace versus the total displacement measured across the yielding portion which was calculated by adding the displacements recorded by potentiometers 7, 8, 9, and 10 and dividing by two. Figure 4-15 (bottom) plots the brace force against the displacement measured across the entire brace including the connections (displacements recorded by potentiometers 3 and 4 were added and divided by two). It is seen that the brace exhibits stable cyclic behavior at all testing amplitudes. The flexibility of the connection is responsible for the slightly larger maximum displacements appearing in Figure 4-15 (bottom). A discussion on the effect of the connection to the overall stiffness is presented in Section 4.6.

The maximum compressive force in Figure 4-15 is seen to be slightly greater than the maximum tension force. In Test 7 for example, the maximum compressive load was 341.3 kips compared with the maximum tension force of 314.5 kips, a difference of 8.5 percent. This relatively small difference is assumed to be related to confinement interaction and is dependent on the deformation level.

The SAC near-field loading history and the recorded force-displacement loops for Specimen 99-1 are given in Figure 4-16. Figure 4-16 (center) plots the force against the displacement measured across the yielding portion of the brace. The brace exhibited stable cyclic behavior even while cycled about an offset displacement of 3.34 in. The maximum tension displacement in the offset position was 4.84 in. (4.1 percent strain) which corresponds to approximately twice the maximum brace design displacement. Figure 4-16 (bottom) plots the force against the displacement of the inner core relative to each end of the outer tube. The displacement in Figure 4-16 (bottom-left) is obtained by adding the displacements recorded by potentiometers 7 and 8 and dividing by 2;

whereas, the displacement in Figure 4-16 (bottom-right) is obtained by adding the displacements recorded by potentiometers 9 and 10 and dividing by two. Figures 4-16 (bottom) indicate that the deformation across the core is essentially symmetric.

Specimen 99-2

The SAC basic loading history imposed on Specimen 99-2 is shown in Figure 4-17 (top) along with the corresponding measured force-displacement loops (bottom). It is seen that the brace exhibits stable cyclic behavior for all displacement amplitudes. Once again, the maximum brace force in compression is seen to be slightly higher than in tension. For test 7, the maximum force in compression was 446.8 kips compared with the maximum tension force of 416.5 kips, a difference of 7.3 percent.

The force-displacement loops resulting from the low-cycle fatigue test performed on Specimen 99-2 are shown in Figure 4-18. The brace exhibited very stable hysteretic behavior for all cycles up to failure. Failure occurred in the second half of the 15th cycle as the steel core fractured inside the encasing mortar/outer tube. These 15 cycles combined with the 2 cycles performed previously for Test 7 of the SAC basic loading history, gives a total of 17 cycles at ± 2.24 in. (2 percent strain) without any appreciable degradation in the hysteretic behavior.

Specimen 99-3

The SAC basic loading history and the corresponding force-displacement loops of Specimen 99-3 are shown in Figure 4-19. Once again it is seen that the brace exhibited stable cyclic behavior for all displacement amplitudes. Slippage of the bolted connection was observed in Tests 6 and 7 as evidenced by the spikes seen in the force-displacement loops. For this brace, the maximum compressive force in Test 7 was 627.9 kips, 9.5 percent greater than the maximum tension force of 573.2 kips.

After completion of the SAC basic loading history, Specimen 99-3 was subjected to additional earthquake loading histories. The histories are derived from the response of an idealized five-story building to the 1940 El Centro N-S ground motion (ELC) and the Sylmar motion (SYL) record during the 1994 Northridge earthquake. In the SYL test shown in Figure 4-20, the maximum brace displacement was 2.41 in. corresponding to a maximum brace strain of 1.77 percent. For the

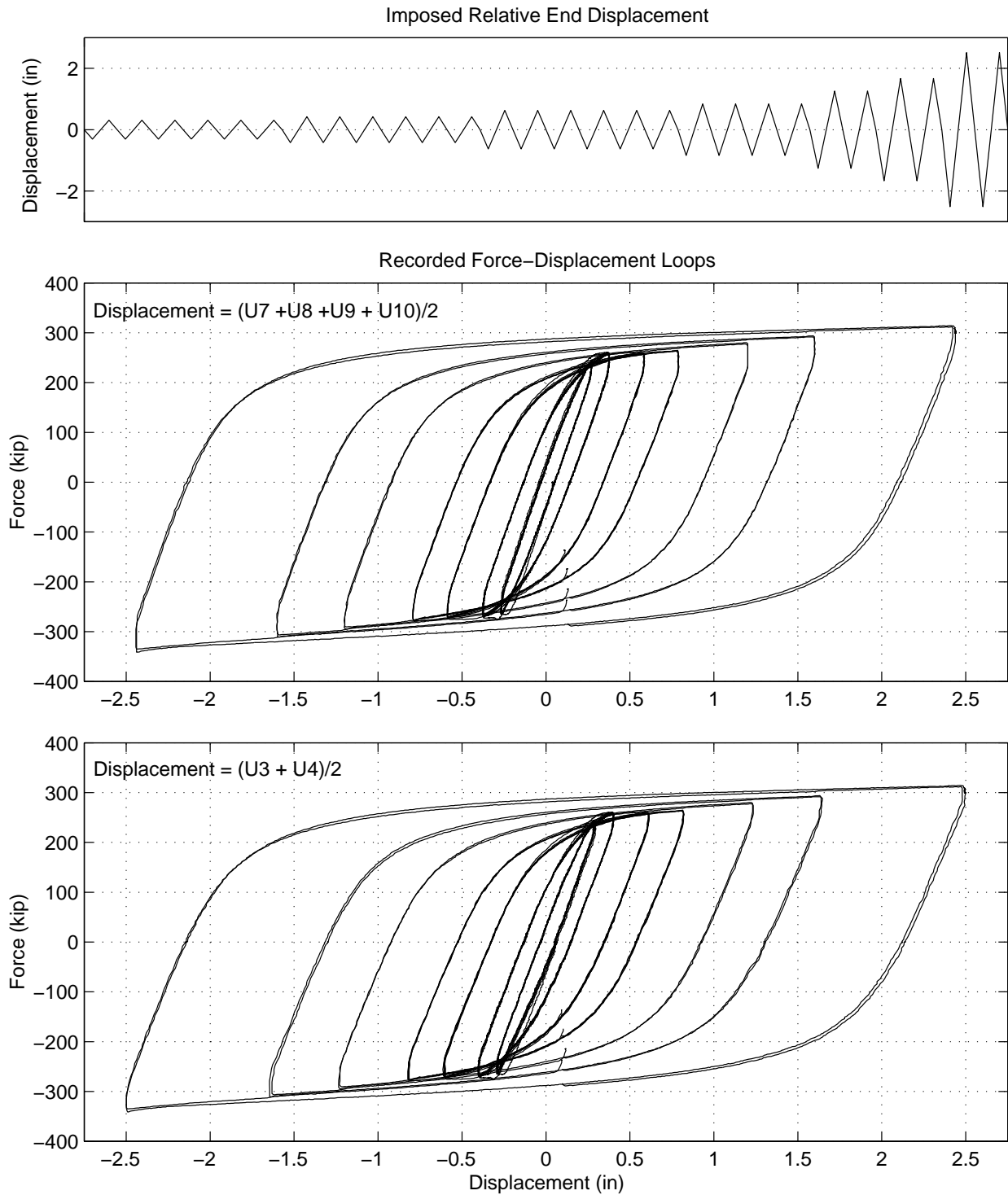


Figure 4-15. Top: SAC basic loading history. Center: The recorded force is plotted versus the displacement of the yielding portion (Specimen 99-1). Bottom: The recorded force is plotted versus the displacement of the entire brace (i.e., flexibility of connections included).

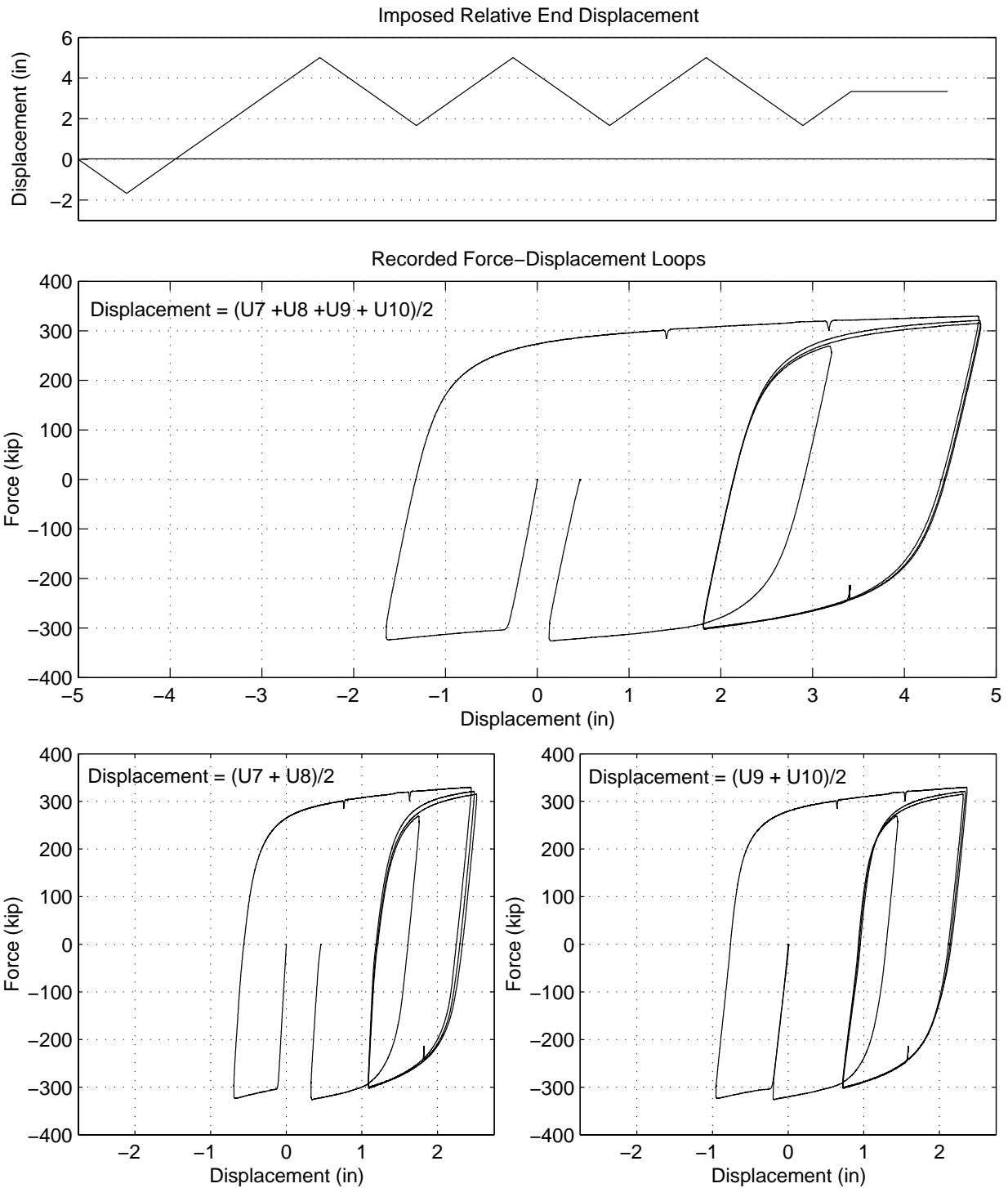


Figure 4-16. Top: SAC near-field protocol. Center: The recorded force is plotted against the displacement measured across the yielding portion (Specimen 99-1). Bottom: The recorded force is plotted versus the displacement of the inner core relative to each end of the tube.

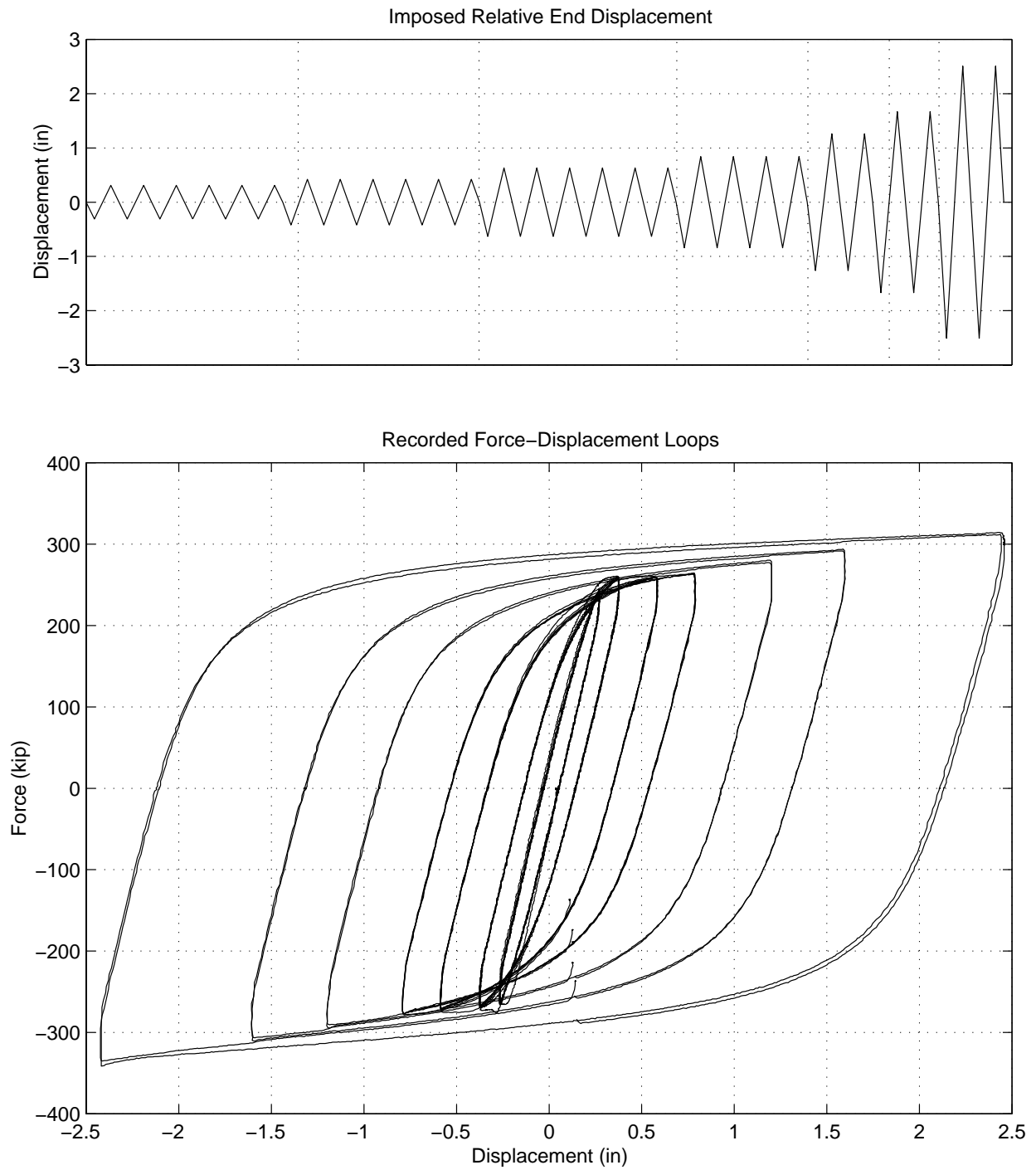


Figure 4-17. SAC basic loading history (top) and recorded force-displacement loops for Specimen 99-2.

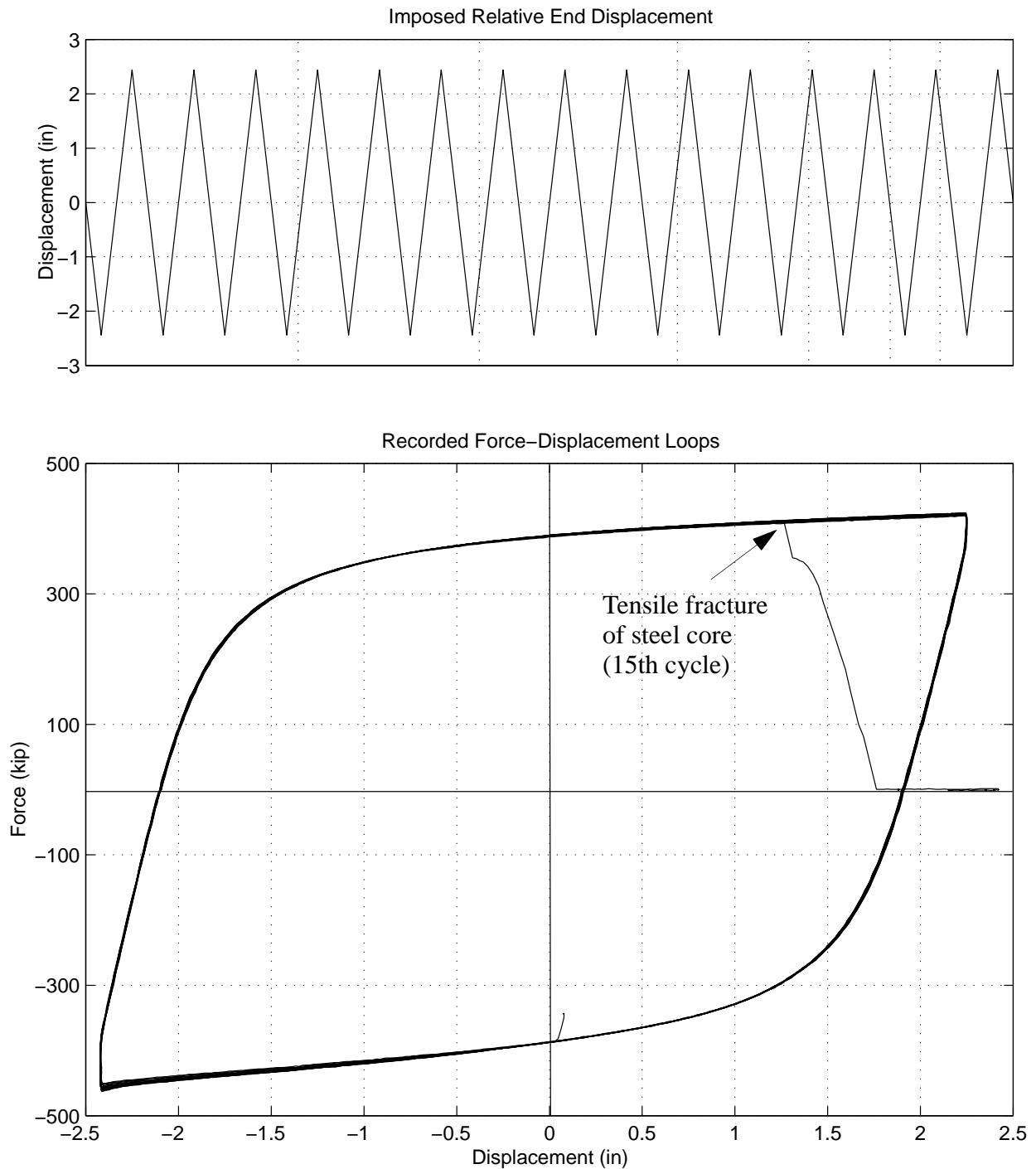


Figure 4-18. Low-cycle fatigue displacement history consisting of 15 cycles (top) and recorded force-displacement loops of Specimen 99-2. The brace exhibits stable, repeatable behavior without any signs of degradation until the 15th cycle when fracture occurs.

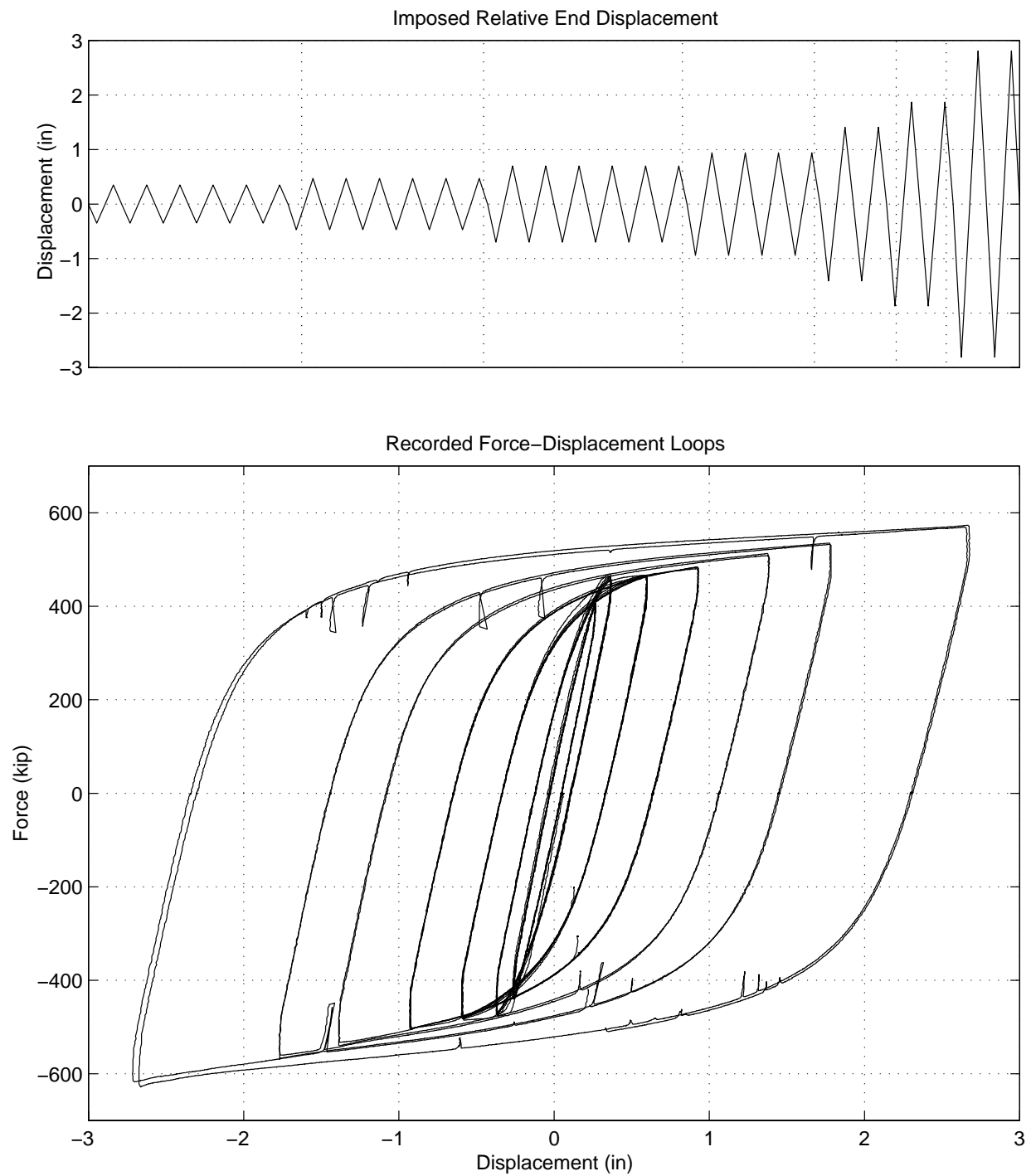


Figure 4-19. SAC basic loading history (top) and recorded force-displacement loops for Specimen 99-3.

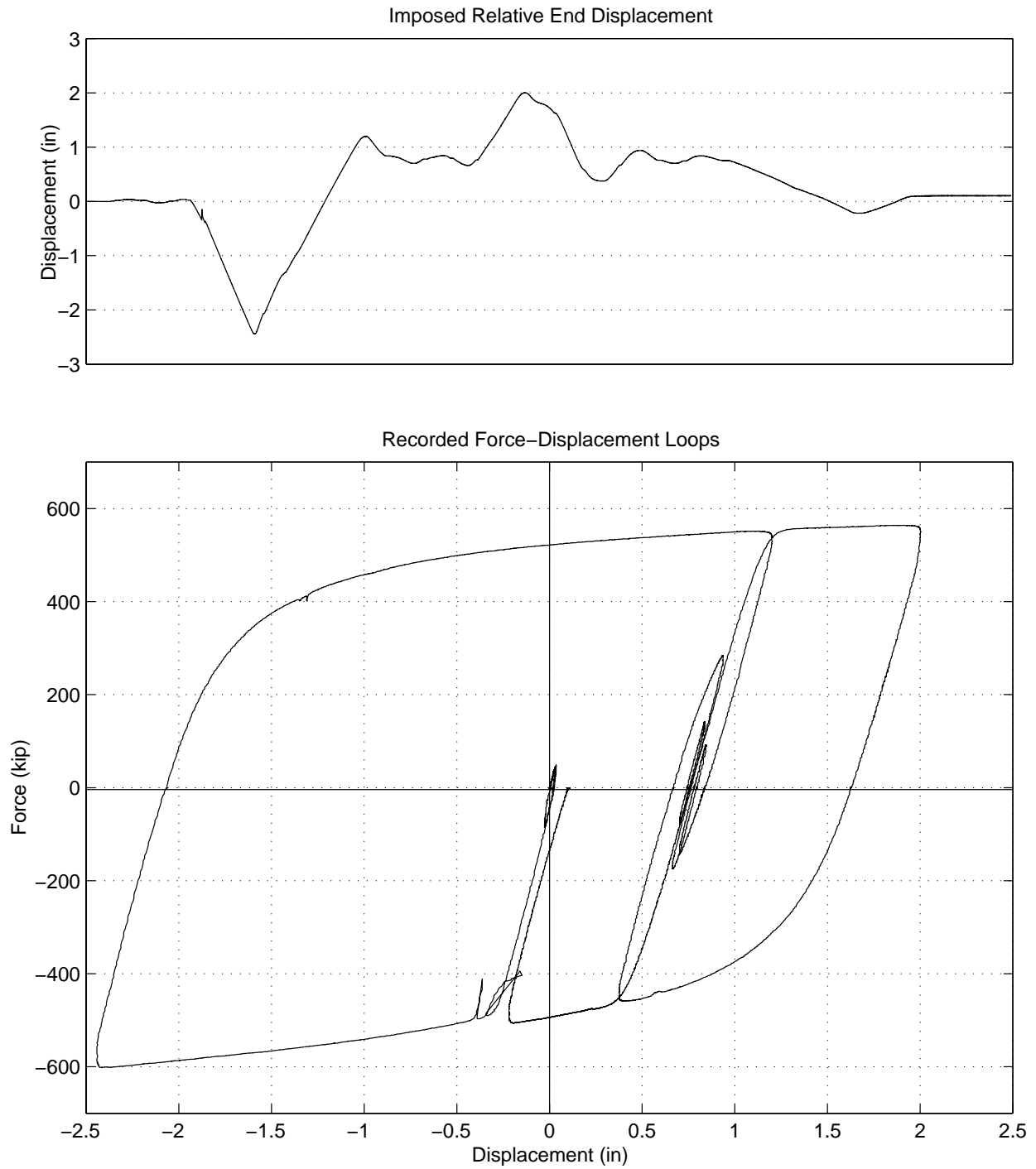


Figure 4-20. Imposed displacement history derived from the computed interstory drift of an idealized five-story building subjected to the 1994 Northridge earthquake Sylmar motion (top) and the force-displacement loops recorded from Specimen 99-3 (bottom).

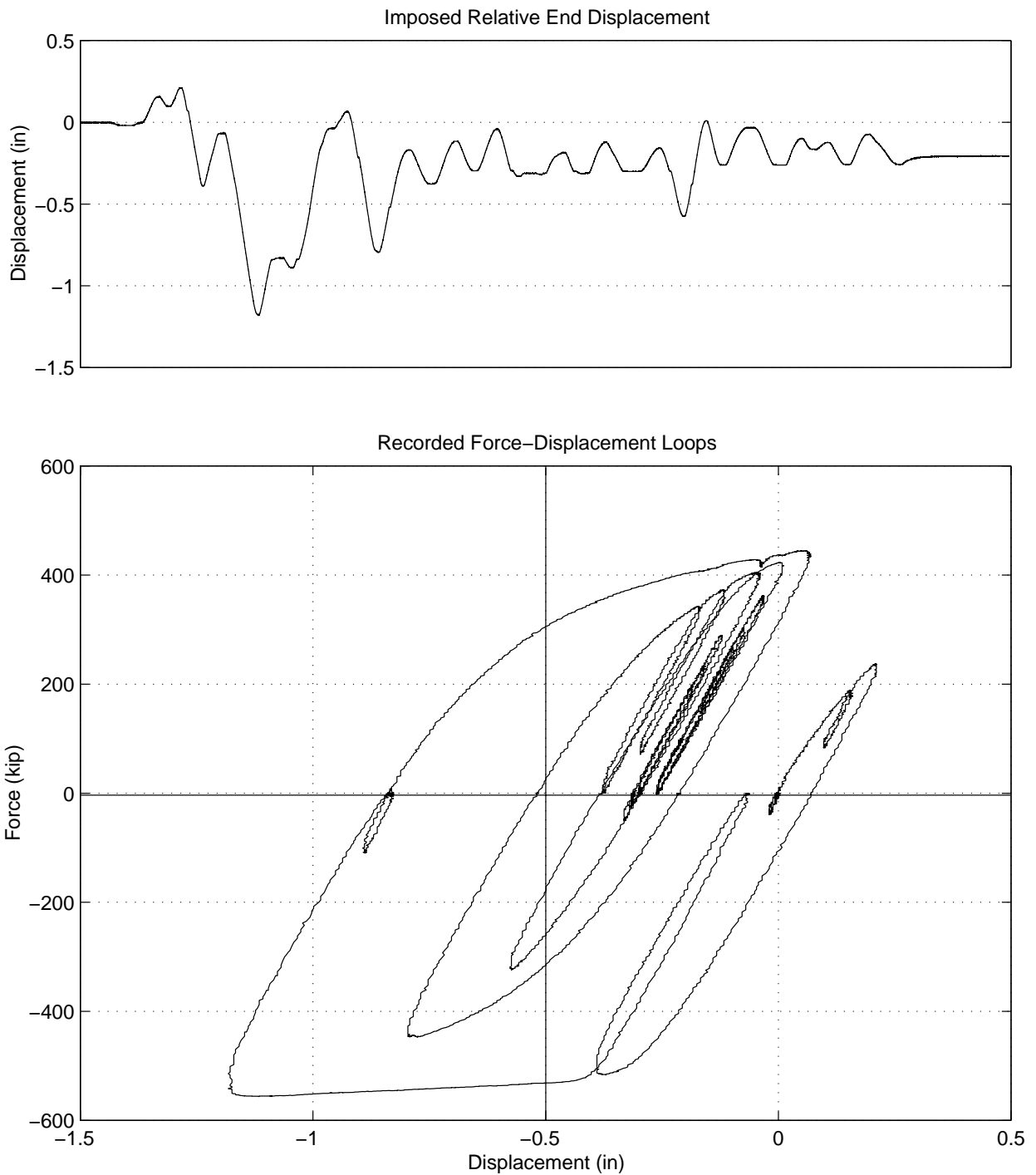


Figure 4-21. Imposed displacement history derived from the computed interstory drift of an idealized five-story building subjected to the 1994 Northridge earthquake Sylmar motion (top) and the force-displacement loops recorded from Specimen 99-3 (bottom).

ELC test shown in Figure 4-21, a maximum displacement of only 0.72 in. (0.53 percent strain) was achieved due to a servo-control system lag. The brace exhibited stable hysteretic behavior in both earthquake displacement tests.

4.5.2 Fall 2000 Test Results

The results of the fall 2000 tests are presented in Figures 4-22 through 4-26. For each test, or set of tests, the imposed displacement history is shown above the corresponding hysteresis loops.

The *OSHPD brace loading history* comprised five loading phases, each corresponding to a set of post-elastic cycles at a constant amplitude. Each test phase was started with zero force and displacement and ended with zero displacement but still under residual load. Upon completion of each test phase — performed under automated displacement control — the specimen was then manually offset by a displacement equal to the yield displacement and subsequently unloaded to return the specimen to zero load at zero displacement. The transition from automatic to manual control is evidenced in the hysteresis loops by small spikes in the region of zero displacement and maximum tension (positive) force.

Specimen 00-11

Figure 4-22 shows the OSHPD brace loading history imposed on Specimen 00-11 and the recorded force-displacement loops. Figure 4-22 (center) plots the recorded force in the brace versus the total displacement measured across the yielding portion of the brace. It is seen that the brace exhibited stable hysteretic behavior for all displacement amplitudes. Figure 4-22 (bottom) plots the recorded force versus the displacement of the inner core relative to the outer tube measured separately at each end of the brace. The loops from the displacement at each end are nearly identical indicating that yielding is uniformly distributed over the length of the steel core. The maximum brace force was 675.6 kips in tension and 764.3 kips in compression, a difference of 13 percent.

The force-displacement loops for the low-cycle fatigue test of Specimen 00-11 are shown in Figure 4-23 (center and bottom). The test consisted of a total of 31 cycles with the brace exhibiting stable hysteretic behavior for the entire test. The initial intention was to conduct the test to failure which was anticipated to occur at roughly 20 cycles. This value was exceeded and subsequently

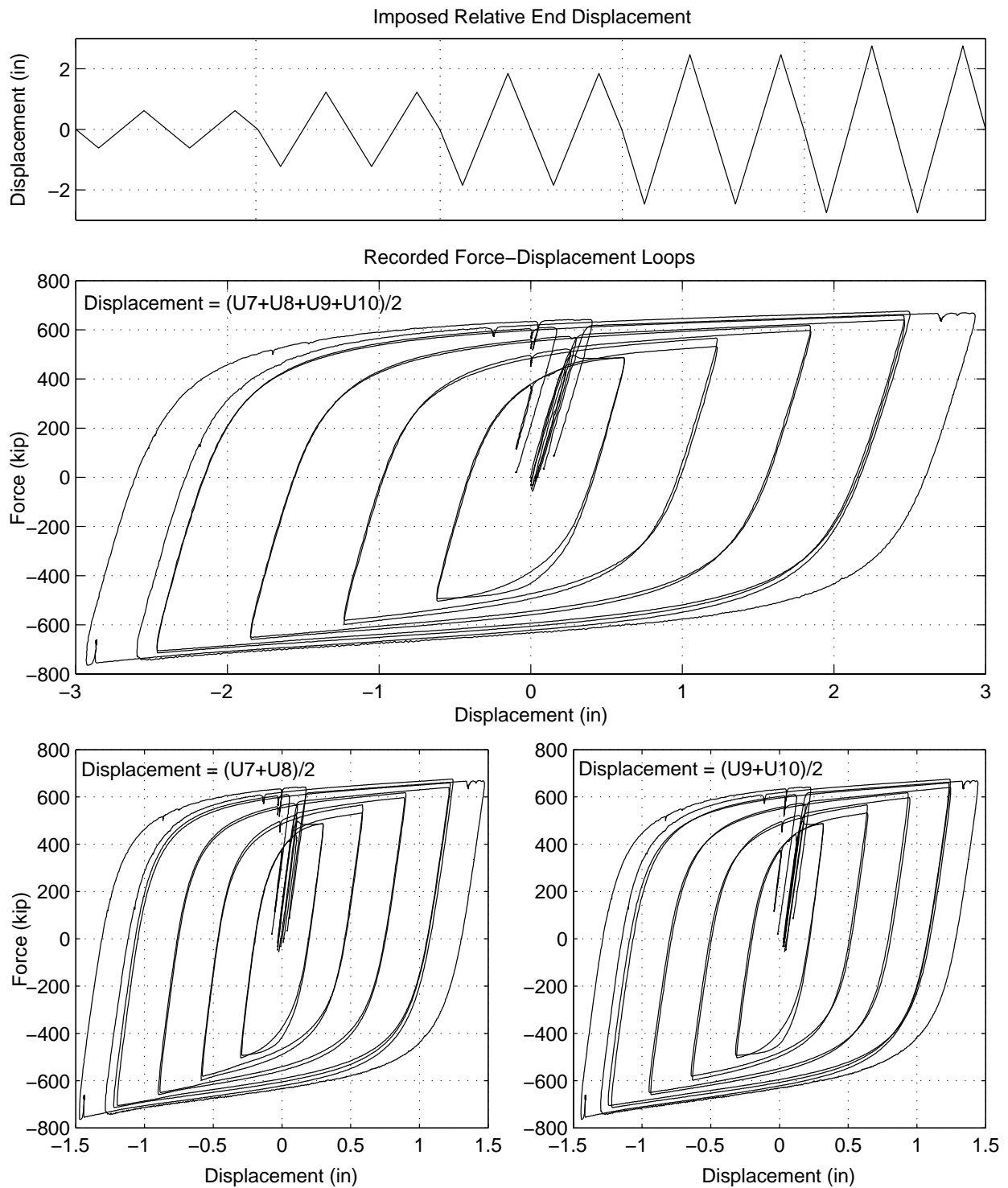


Figure 4-22. Top: OSHPD brace loading history. Center: The recorded force is plotted against the displacement measured across the yielding portion (Specimen 00-11). Bottom: The recorded force is plotted versus the displacement of the inner core relative to each end of the tube.

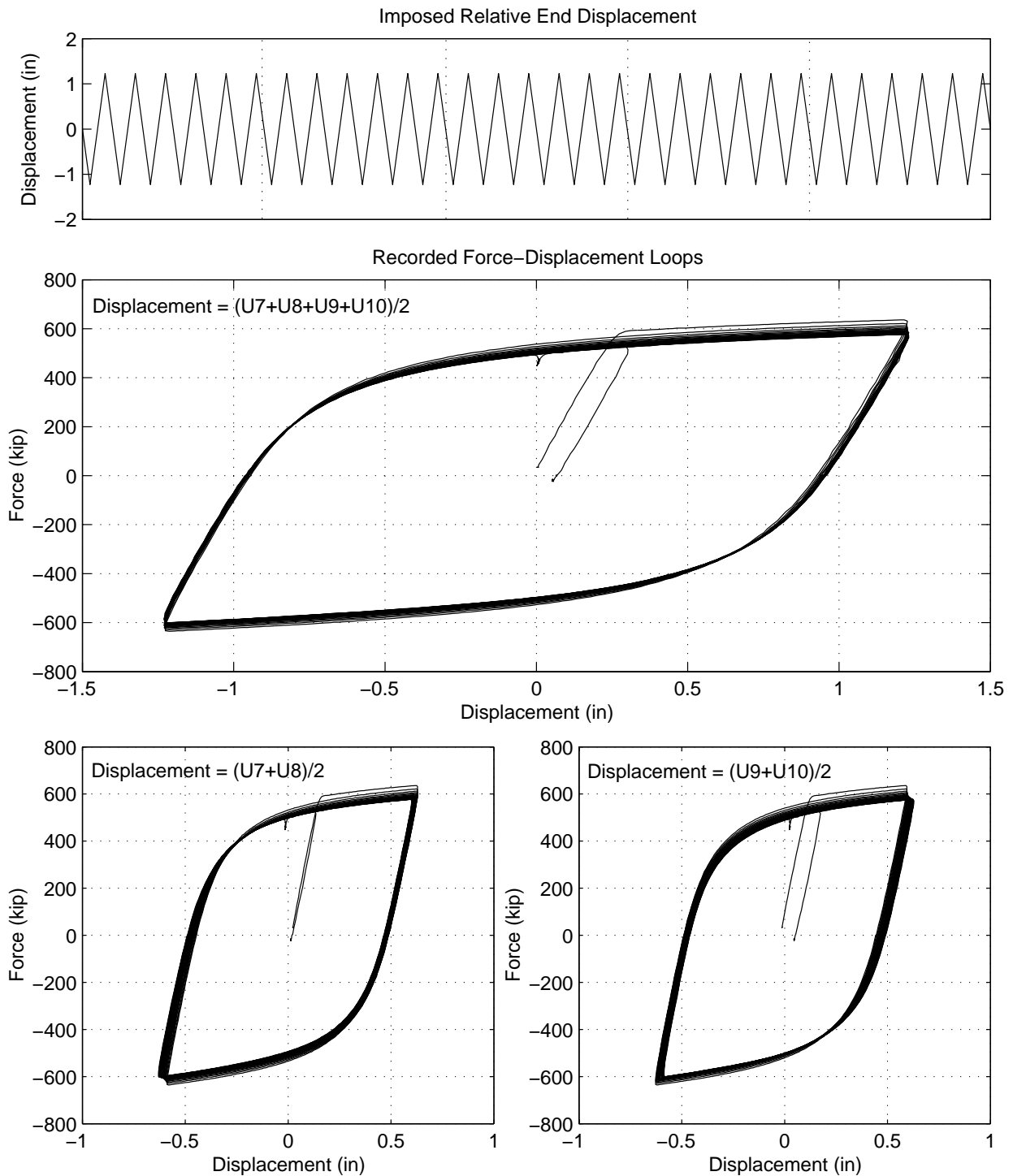


Figure 4-23. Bottom: Low-cycle fatigue test. Center: The recorded force is plotted against the displacement measured across the yielding portion (Specimen 00-11). Bottom: The recorded force is plotted versus the displacement of the inner core relative to each end of the tube.

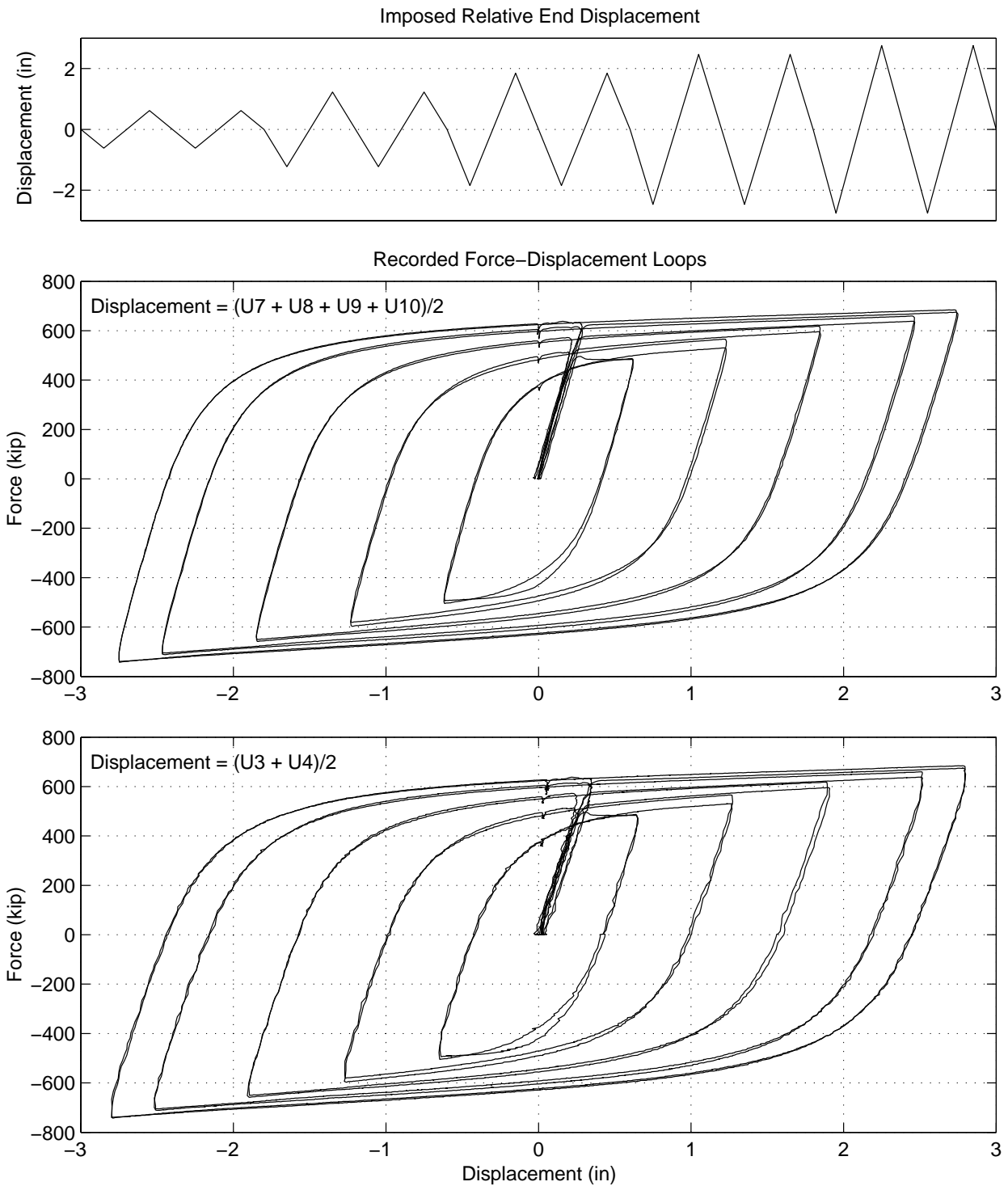


Figure 4-24. Top: OSHPD basic displacement history. Center: The recorded force is plotted versus the displacement of the yielding portion (Specimen 00-12). Bottom: The recorded force is plotted versus the displacement of the entire brace (i.e., flexibility of connections included).

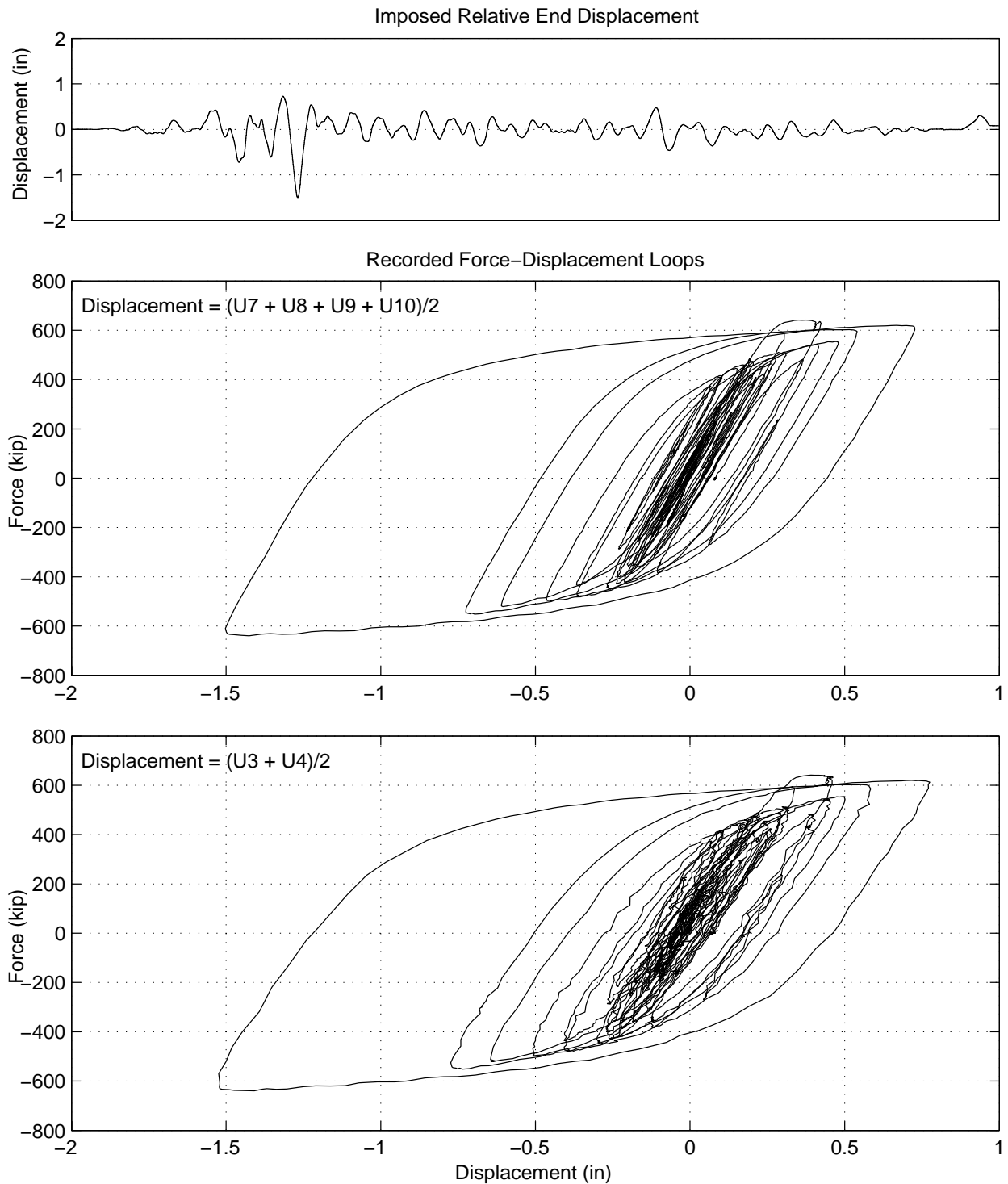


Figure 4-25. Top: Displacement loading history that approximates the interstory drift of a structure subjected to the DBE earthquake. Center: The recorded force is plotted versus the displacement of the yielding portion (Specimen 00-12). Bottom: The recorded force is plotted versus the displacement of the entire brace (i.e., flexibility of connections included).

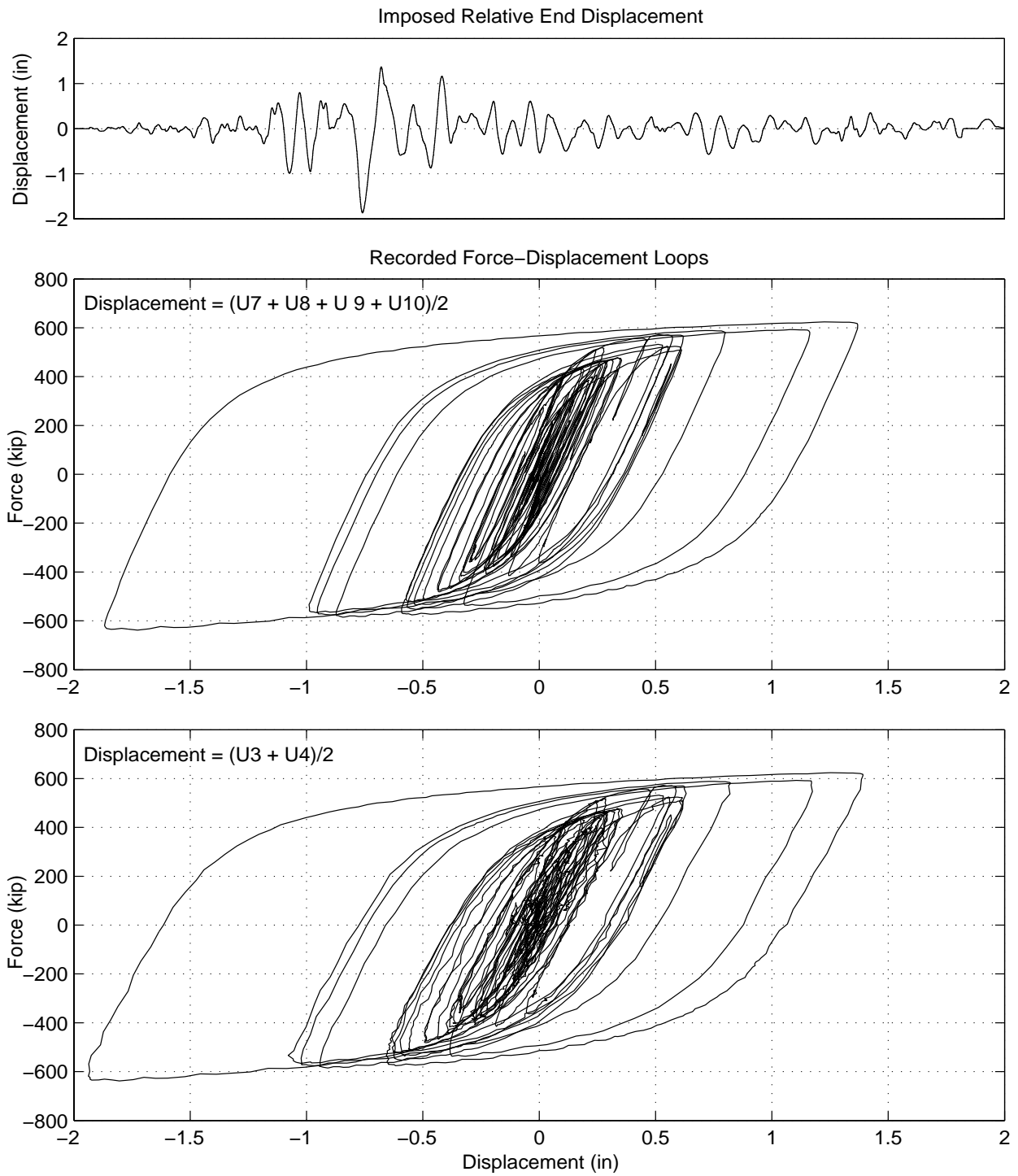


Figure 4-26. Top: Displacement loading history that approximates the interstory drift of a structure subjected to the MCE earthquake. Center: The recorded force is plotted versus the displacement of the yielding portion (Specimen 00-12). Bottom: The recorded force is plotted versus the displacement of the entire brace (flexibility of connections included).

the test was stopped at 31 cycles (without failure) in order to avoid potential damage to the instrumentation or test setup.

Specimen 00-12

Force-displacement loops showing the response of Specimen 00-12 to the OSHPD brace loading history cyclic tests are shown in Figure 4-24. As with Specimen 00-11, the brace showed stable hysteretic behavior for all displacement amplitudes.

Upon completion of the OSHPD brace loading history, Specimen 00-12 was subjected to two simulated earthquake motions. The earthquake history corresponding to the Design Basis Earthquake (DBE) is shown in Figure 4-25 (top), while Figure 4-25 (bottom) shows the resulting force-displacement loops. During the DBE, the maximum brace displacement was -1.49 in. corresponding to a strain of 1.11 percent. Figure 4-26 shows the earthquake history corresponding to the Upper Bound Earthquake (UBE) and the resulting force-displacement loops. For this earthquake, the maximum brace displacement was -1.86 in. corresponding to a maximum brace strain of 1.38 percent.

4.6 Comparison of Measured and Computed Stiffness Values

In this section the experimental data are used to identify the elastic and secondary stiffnesses of the brace. In addition to comparing the measured and computed elastic stiffness values, the contributions of the different portions of the brace to the overall stiffness are also examined.

4.6.1 Elastic (Pre-yielding) Stiffness of the Brace

Measured Stiffness

Figure 4-27 shows simple schematic diagrams of the inner core of unbonded braces along with the location of the instrumentation. The inner core shown in Figure 4-27 (top) is representative of Specimens 99-3, 00-11 and 00-12, which have a cruciform steel core cross section throughout. Figure 4-27 (bottom) shows the inner core of Specimens 99-1 and 99-2 which has a third portion where the steel core transitions from a flat-plate to a cruciform cross section. The length and area of the yielding portion of the brace are denoted by L_i and A_i , respectively, and likewise, L_{con} and A_{con} , are the length and area of the connection portion. The transition zone in Figure 4-27 (bot-

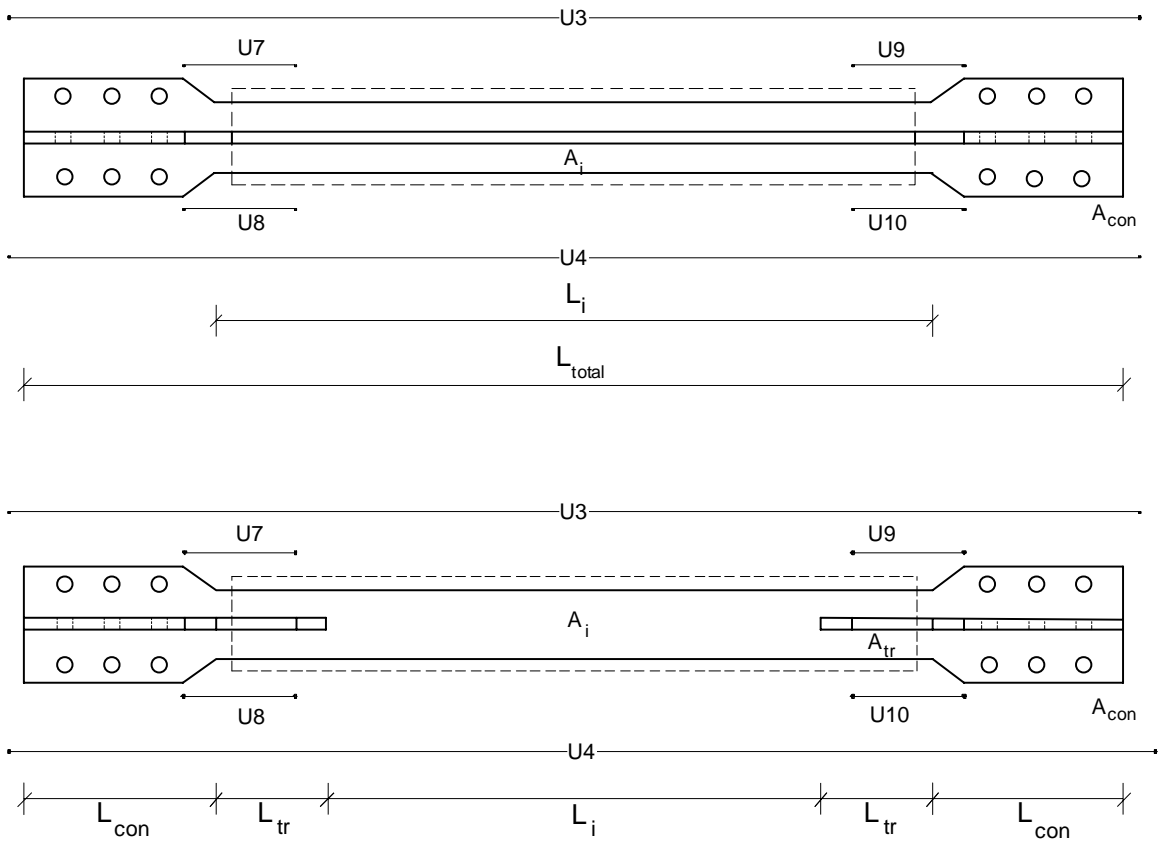


Figure 4-27. Possible unbonded brace steel core configurations. Top: configuration of Specimens 99-3, 00-11 and 00-12. Bottom: configuration of Specimens 99-1 and 99-2.

tom) has length L_{tr} and area A_{tr} . The lines labelled $U3$, $U4$, $U7$, $U8$, $U9$ and $U10$ show the location of potentiometers 3, 4, 7, 8, 9 and 10 shown in Figure 4-23.

The measured stiffness values are extracted from the elastic portions of the recorded loops using the relation

$$K^e = \frac{2F}{U7 + U8 + U9 + U10}, \text{ where } F < \sigma_Y A, \quad (4-1)$$

for the portion of the brace within the tube and

$$K_{total}^e = \frac{2F}{U3 + U4}, \text{ where } F < \sigma_Y A, \quad (4-2)$$

for the entire brace including connections, where F is the measured force and the superscript e indicates that the values were obtained from experimental data.

The stiffness value K^e from Equation (4-1) corresponds to the stiffness of the yielding portion of the brace denoted K_i for Specimens 99-3, 00-11, and 00-12; whereas, the measured stiffness K^e for Specimens 99-1 and 99-2 (Figure 4-27 bottom) includes the transition zone and hence is slightly higher than K_i .

Figure 4-28 shows the force-displacement loops recorded from the three spring 1999 specimens subjected to Test C of the SAC basic loading history, as well as one of the fall 2000 specimens subjected to Test C of the OSHPD brace loading history. The elastic stiffness values shown in each plot represent the average elastic stiffness values as calculated according to Equation (4-1) by fitting a straight line to the measured force-displacement loops (using a least squares approximation).

Computed Stiffness

The total elastic stiffness of the brace is the in-series sum of the individual stiffnesses of the different brace segments

$$K_{total} = \frac{1}{\left(\frac{1}{K_i} + 2 \frac{1}{K_{con}} + 2 \frac{1}{K_{tr}} \right)} \quad (4-3)$$

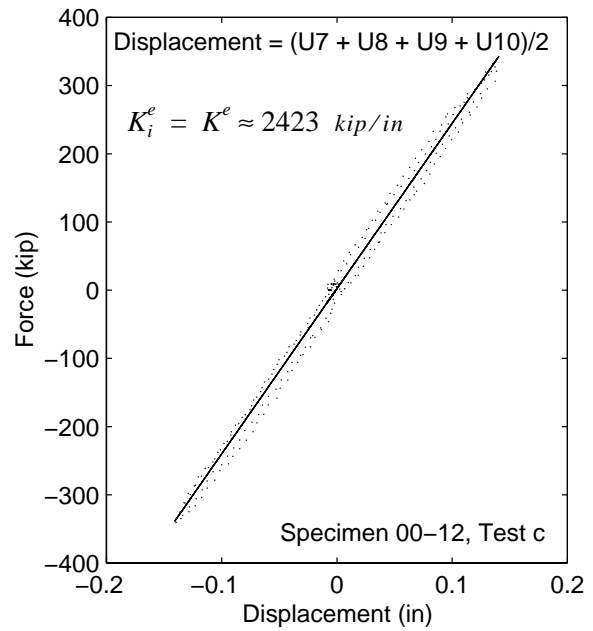
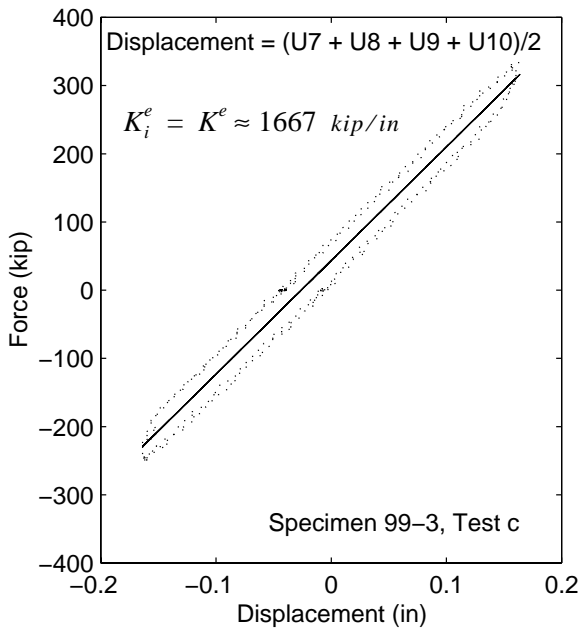
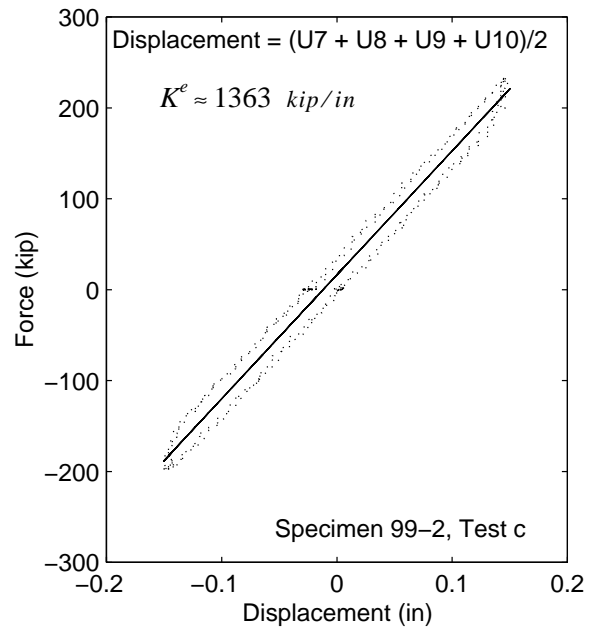
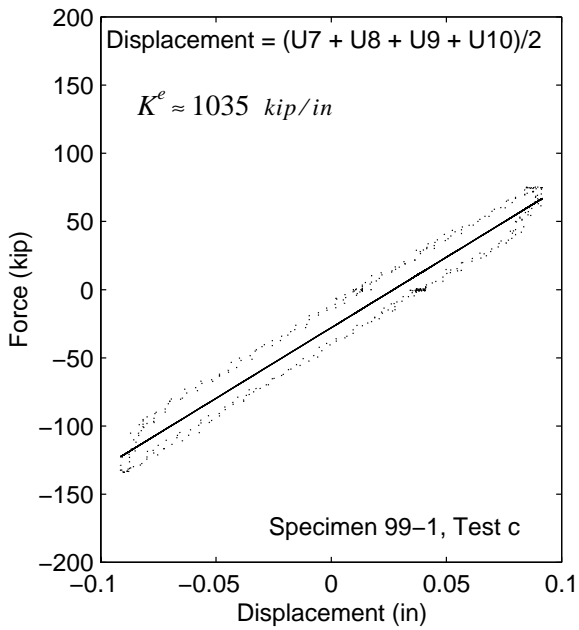


Figure 4-28. Force-displacement loops for the different brace sizes tested along with the estimated stiffness values K^e .

where $K_i = EA_i/L_i$ is the elastic stiffness of the yielding portion, $K_{con} = EA_{con}/L_{con}$ is the stiffness of the connection portion and $K_{tr} = EA_{tr}/L_{tr}$ is the stiffness of the transition portion (if present).

As an example, the computed stiffness values for the yielding and connection portions of Specimens 00-11 and 00-12 are respectively

$$K_i^c = \frac{A_i \cdot E}{L_i} \approx \frac{7125 \text{ mm}^2 \cdot 210 \text{ GPa}}{3410 \text{ mm}} = 439 \frac{\text{kN}}{\text{mm}} = 2506 \frac{\text{kip}}{\text{in}}, \text{ and} \quad (4-4)$$

$$K_{con}^c = \frac{A_{con} E}{L_{con}} \approx \frac{A_{con} \cdot E}{(L_{total} - L_i)/2} = \frac{11225.8 \text{ mm}^2 \cdot 210 \text{ GPa}}{(4500 - 3410)/2} = 4326 \frac{\text{kN}}{\text{mm}} = 24707 \frac{\text{kip}}{\text{in}}. \quad (4-5)$$

With the above values, the total stiffness, K_{total}^c , given by Equation (4-3) is 2083 kip/in.

Table 4-4 lists the measured stiffness, computed stiffness and the difference between these values for each test specimen. The measured values given in columns 2 and 3 were computed by fitting a straight line to the largest elastic level deformations of each brace (as shown in Figure 4-28). The computed stiffness values given in columns 4, 5 and 6 were obtained from Equations (4-4), (4-5) and (4-3), respectively.

Table 4-4. Comparison of measured and theoretical elastic stiffness values

Specimen	Measured Stiffness (kips/in)		Computed Stiffness (kips/in)			Difference	
	K_i^e Eqn. (4-1)	K_{total}^e Eqn. (4-2)	K_i^c Eqn. (4-4)	K_{con}^c Eqn. (4-5)	K_{total}^c Eqn. (4-3)	K_i	K_{total}
99-1	not available ^a	950	1128	20874	976	NA	-2.7%
99-2	not available	1227	1554	20874	1265	NA	-3.0%
99-3	1667	1499	1790	20874	1528	-6.9%	-1.9%
00-11	2367	2072	2506	24707	2083	-5.5%	-0.5%
00-12	2423	2070	2506	24707	2083	-3.3%	-0.6%

a. The value obtained from Eqn. (4-1) is not K_i as it includes the transition zone

Table 4-4 indicates that the flexibility of the connection portion of the brace has an appreciable contribution to the overall stiffness. For Specimen 00-12 for example, the connection reduces the

overall stiffness by 15 percent. Ideally the stiffness values used in the design should account for both portions of the brace. If the stiffness is calculated assuming that the cross-sectional area is equal to A_i , and constant over the entire length, the stiffness for Specimen 00-12 is underestimated by 9 percent.

4.6.2 Secondary (Tangent) Stiffness

The force-displacement loops shown in Figures 4-15 for the SAC basic loading history and 4-22 for the OSHPD brace loading history indicate that the secondary stiffness decreases with each increasing amplitude test phase. Figure 4-29 shows tests 1, 3 and 5 from the OSHPD brace loading history performed on Specimen 00-12. The estimated value for the secondary stiffness is highest for the first yielding cycle (Test 1), with a value of 100 kip/in, and subsequently decreases reaching a minimum of approximately 22 kips/in for Test 5. Table 4-5 lists the average tangent moduli for the cases considered in Figure 4-29 with values ranging from 1208 ksi to 266 ksi for Tests 1 and 5, respectively. An average value for the tangent modulus for A36 steel is between 700 and 900 ksi (Salmon and Johnson, 1996).

Table 4-5. Secondary (tangent) stiffness values for Specimen 00-12

Test phase of <i>OSHPD Basic Loading History</i>	Post-yielding Ratio $\alpha = \frac{K_2}{K_i} = \frac{E_t}{E}$	Secondary Stiffness K_2
1	4.2%	22 kip/in
3	2.1%	50 kip/in
5	1.0%	100 kip/in

4.7 Cumulative Plastic Ductility Demands

A measure used in practice to describe the plastic demand on a buckling-restrained brace element is the cumulative plastic strain or alternatively, the Cumulative Plastic Ductility (CPD). The CPD, which is a normalized expression of the cumulative plastic deformation is defined by

$$CPD = \sum_i \frac{|u_{p_i}^{max} - u_{p_i}^{min}|}{u_y} \quad (4-6)$$

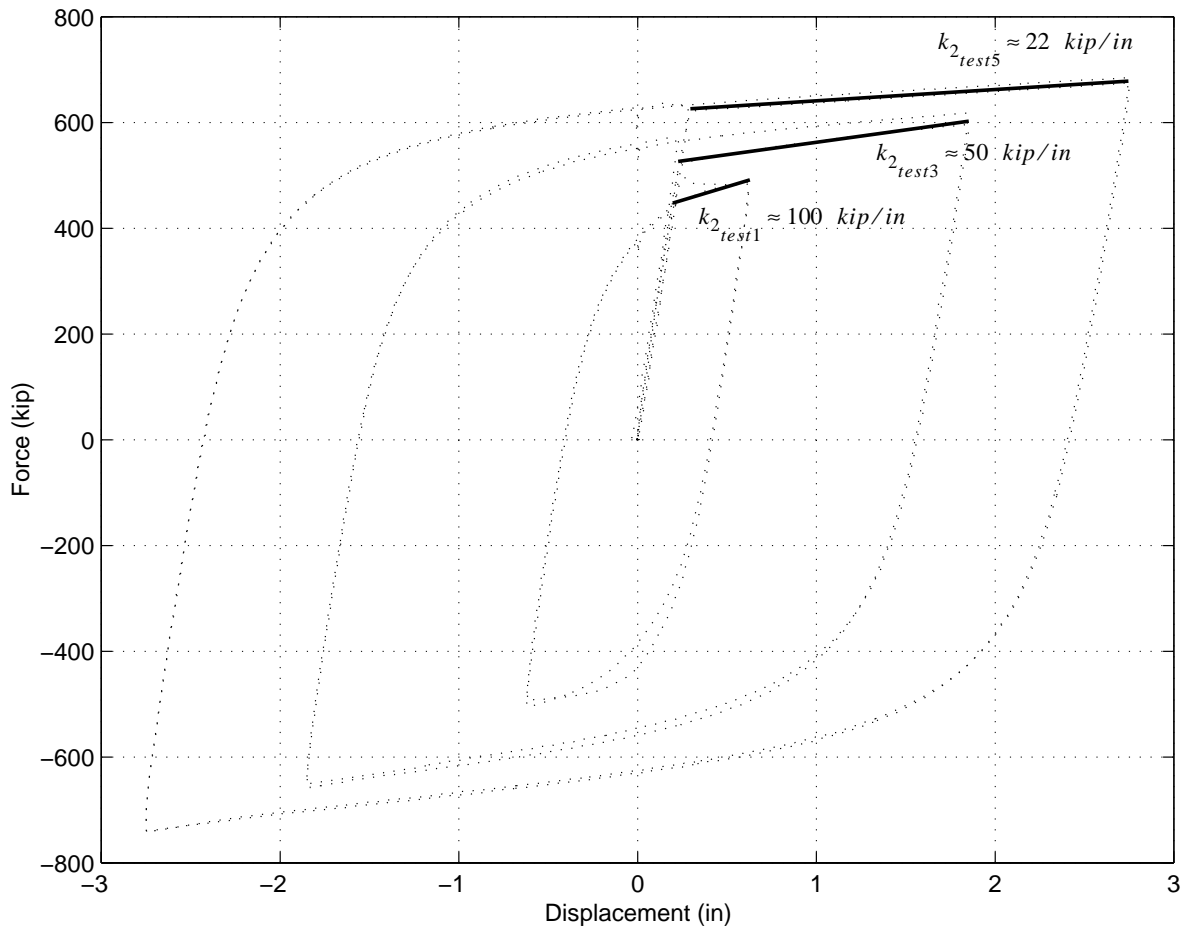


Figure 4-29. Plot showing estimated secondary stiffness values calculated from Tests 1, 3 and 5 of the OSHPD brace loading history for Specimen 00-12.

where $u_{p_i}^{max}$ and $u_{p_i}^{min}$ are the maximum and minimum *plastic* displacements during each visit i into the inelastic range and u_y is the yield displacement of the brace.

For example, a single monotonic displacement that reaches a ductility of eight results in a CPD of seven. That is, the inelastic brace deformation is seven times the yield displacement (eight total minus one elastic). Furthermore, if the loading is reversed and the displacement brought back to zero the CPD would be 13. The CPD of the fall 2000 Specimens under the OSHPD brace loading history is shown in Table 4-6.

An example of the calculation of CPD is given in Figure 4-30. Figure 4-30 (top) shows the loading history from Test Phase 1 (second line in Table 4-3). The heavy line segments indicate those portions of the history during which inelastic deformation occurs. The center plot of Figure 4-30 shows the successive visits to the inelastic range on an idealized force-displacement loop, while the bottom plot depicts the increase of Cumulative Plastic Ductility with time.

Table 4-6. Cumulative Plastic Ductility calculations for the OSHPD brace loading history

Test Phase	No. of Cycles n	Brace Displacement δ_{br}	Ductility μ	Plastic Ductility μ_p	Cumulative Plastic Ductility Total $\sum_n \mu_p$
d	2	0.19	1	0	0
1	2	0.61	3.3	2.33	17.64
2	2	1.24	6.66	5.66	63.0
3	2	1.85	10	9.0	135.0
4	2	2.47	13.33	12.33	233.6
5	2	2.78	15.0	14.0	345.6

Figure 4-31 (top) plots the Design Base Earthquake loading history used for the testing of Specimen 00-12; while Figure 4-31 (bottom) depicts the increase of Cumulative Plastic Ductility with time under this loading. The calculation of the CPD was achieved with an algorithm that detects local peaks and valleys in the displacement history and examines whether or not the brace has experienced plastic straining (i.e., an inelastic visit).

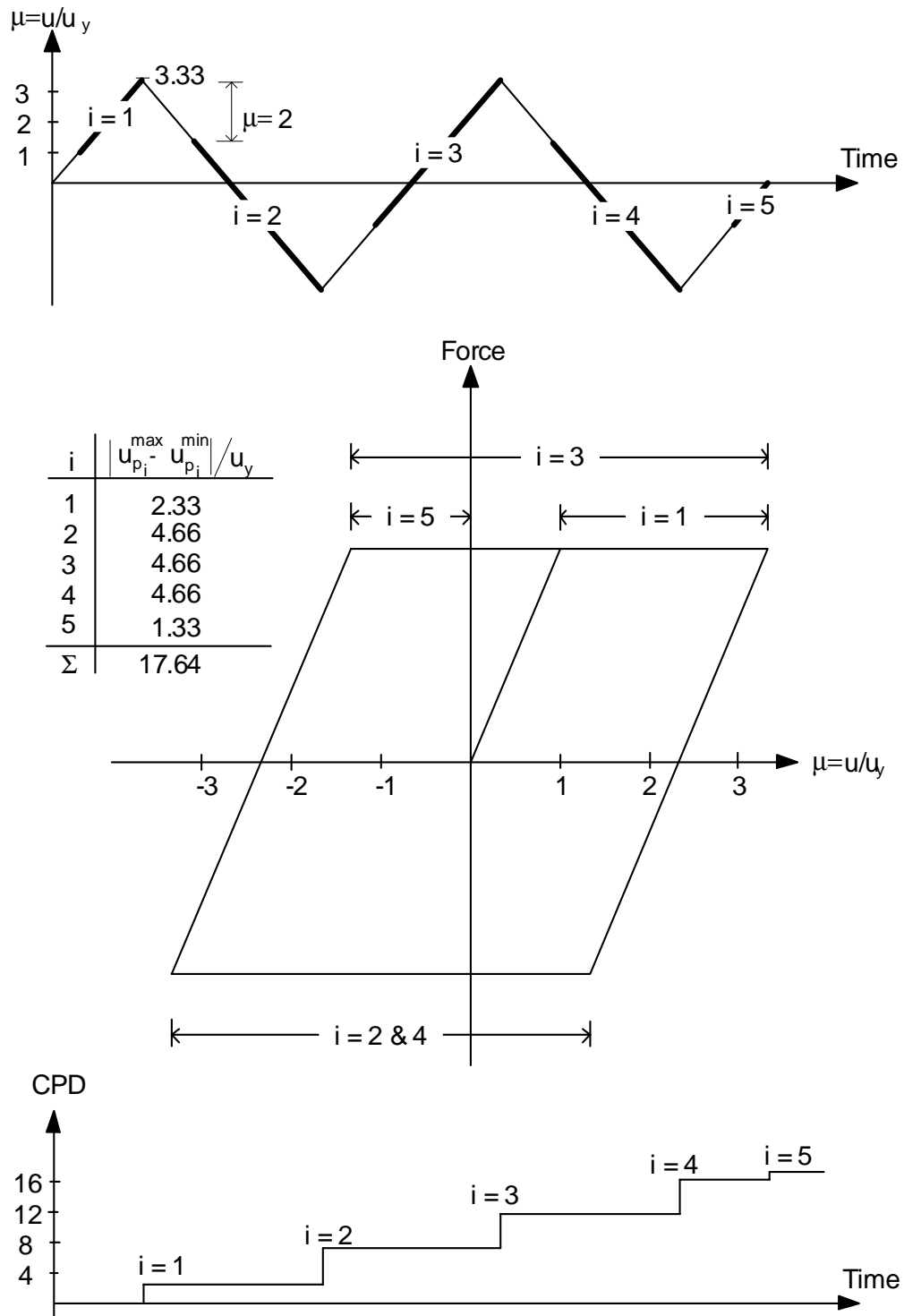


Figure 4-30. Top: Loading history normalized to the yield displacement. Thick segments indicate inelastic deformation. Center: Force-displacement loop. The successive visits in the inelastic range are counted with the index i . Bottom: Increase of Cumulative Plastic Ductility with time.

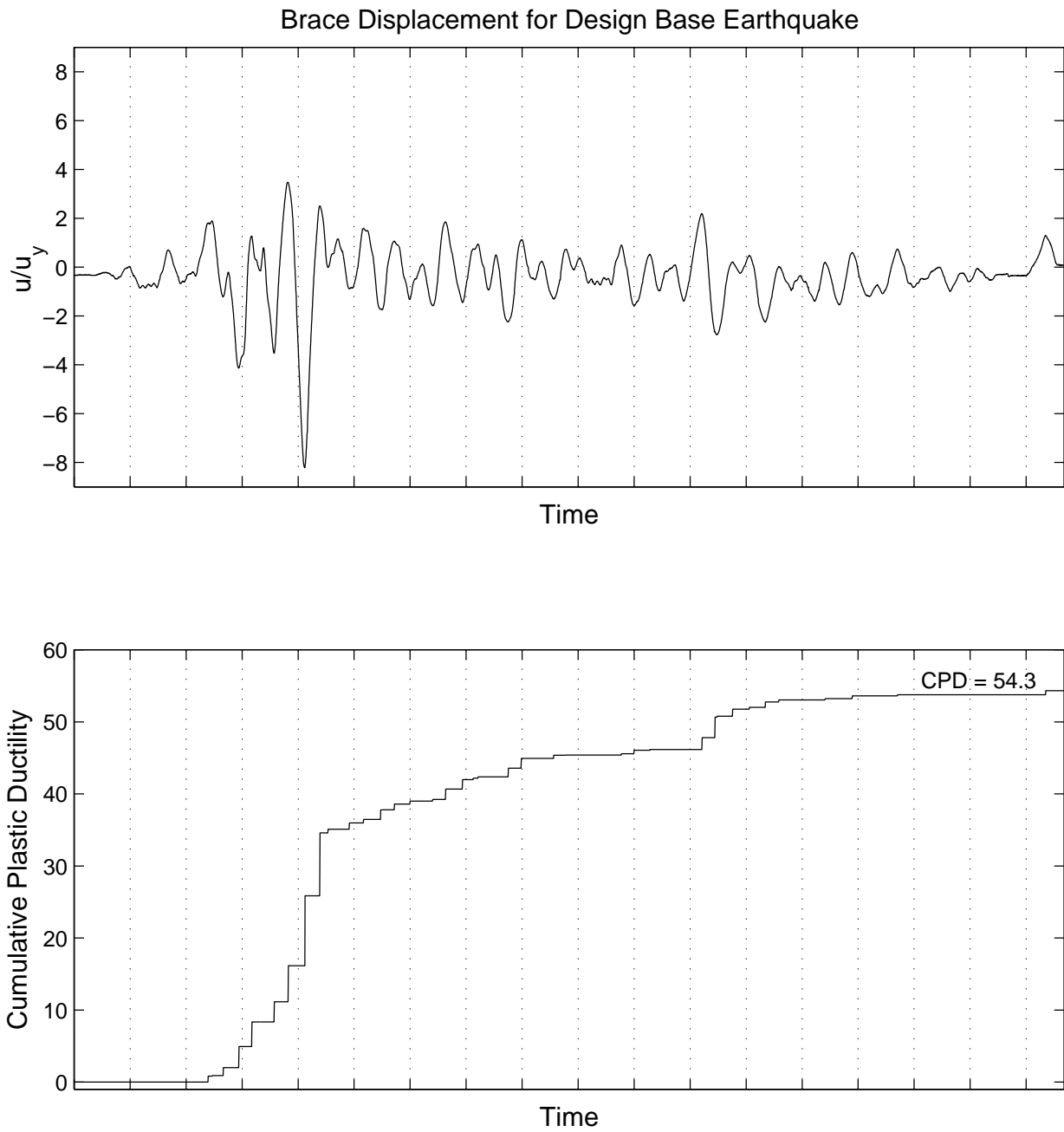


Figure 4-31. Drift-induced displacement history for the DBE earthquake used to test Specimen 00-12 (top) and the running value of the Cumulative Plastic Ductility (bottom).

The CPD values for all tests are summarized in Table 4-7. Both the CPD for each individual test and the total CPD that a given brace experienced throughout the entire testing protocol are given. It is noted that the CPD of the brace during the testing protocol exceeds, by far, the CPD demand of the Upper Bound Earthquake.

Table 4-7. Cumulative Plastic Ductility of tests performed at UC Berkeley

Specimen	Test Description	Maximum Ductility μ_{max}	Cumulative Plastic Ductility	Total CPD For Brace
UC Davis Plant and Environmental Sciences Building (Spring 1999)				
99-1	SAC basic loading history	10.0	243.5	323.8
	SAC near-field protocol	20.0	80.3	
99-2	SAC basic loading history	10.0	243.5	879
	Low-cycle fatigue tests	10.0	636.5	
99-3	SAC basic loading history	10.0	243.5	278.7
	Displacement derived from Sylmar motion	2.35	8.6	
	Displacement derived from El Centro motion	8.30	26.6	
Kaiser Santa Clara Medical Center (Fall 2000)				
00-11	OSHPD brace loading history	15.0	345.4	1045
	Low cycle fatigue test	6.7	699.6	
00-12	OSHPD brace loading history	15.0	345.4	537.7
	Record derived from Design Basis Earthquake	3.49	54.3	
	Record derived from Upper Bound Earthquake	7.26	138.0	

A recent study (Sabelli 2001) looked at the response of braced frame steel structures to various earthquake ground motions. The structures considered in this study included six conventionally braced and five buckling-restrained braced frames, ranging in height from three to six stories. The yield force of the braces at the first level was 243 kips for the three-story building and 382 kips for the six-story structure. The approximate building periods for the three- and six-story structures were assumed to be 0.31 sec and 0.55 sec, respectively. The analysis considered a suite of 20 probabilistic ground motion time-histories specified by SAC, generated for the Los Angeles, California, area (Woodward-Clyde Federal Services 1997). It was found that for the 20 ground motions considered, the maximum brace ductility for any single brace in the buckling-restrained

braced structures was 23.2. The maximum Cumulative Plastic Ductility for a single brace was 203.7. The record which produced this maximum CPD was the so-called LA01 record which was derived originally from the 1940 Imperial Valley, El Centro record scaled to achieve a hazard level corresponding to a 10-percent probability of exceedance in 50 years.

Table 4-8 presents selected results reported in the study. The average Cumulative Plastic Ductility for all records as well as the maximum values of the brace ductility are shown for two structures, a three-story and a six-story structure braced in a chevron configuration. The different hazard levels shown in Column 2 correspond to different probabilities of exceedance in a 50-year period. For the three-story structure, results are presented for the suite of ground motions scaled to achieve a hazard level corresponding to a 10-percent probability of exceedance in 50 years. For the six-story structure, results for three different hazard levels (2, 10 and 50 percent in 50 years) and a near-field record are presented.

Table 4-8. Average, maximum response quantities of buckling-restrained braces for ground motions considered at each hazard level. (Adapted from Sabelli, 2000)

Structure	Hazard Level (% in 50 years)	Maximum Brace Ductility	Cumulative Plastic Ductility
3-Story Chevron	10%	9.7	39
6-Story Chevron	10%	10.7	83
6-Story Chevron	50%	6.6	45
6-Story Chevron	2%	17.4	139
6-Story Chevron	Near Field	14.6	95

By comparing Tables 4-7 and 4-8 it is seen that the average values reported by Sabelli are similar to the values imposed on the braces during testing. The DBE and UBE used to test Specimen 00-12, for example, are close to the maximum response quantities in the 10- and 2- percent hazard levels, respectively. It is noted that the total Cumulative Plastic Ductility imposed on each brace over the course of testing exceeds by far the demand values reported by Sabelli, indicating that the unbonded brace has a plastic fatigue life that is substantially greater than the demand represented by a single design- or maximum-level earthquake.

5 Characterization of Mechanical Behavior

In this section the force-displacement relation of an unbonded brace is characterized at the macroscopic level via the Bouc-Wen model. This approach is selected since the force, $P(t)$, of the brace is given as a function of the displacement and velocity of its attachments, a formulation that can be directly incorporated in structural analysis software. The calibration of the model parameters is based on the experimental data presented in Chapter 4.

5.1 Macroscopic Modeling of Hysteretic Behavior

A suitable model to approximate the nonlinear hysteretic behavior of an unbonded brace is

$$P(t) = \alpha K u(t) + (1 - \alpha) K u_y z(t) \quad (5-1)$$

where $u(t)$ is the axial deformation of the brace, K is the brace elastic stiffness, α is the ratio of the post-yielding to elastic stiffness, u_y is the yield displacement, and $z(t)$ is a hysteretic dimensionless quantity governed by the differential equation

$$u_y \dot{z}(t) + \gamma |\dot{u}(t)| z(t) |z(t)|^{n-1} + \beta \dot{u}(t) |z(t)|^n - \dot{u}(t) = 0. \quad (5-2)$$

In the above equation β , γ , and n are dimensionless quantities that control the shape of the hysteretic loop. The hysteretic model, expressed by Equations (5-1) and (5-2), was originally proposed by Bouc (1971) for $n = 1$, and subsequently extended by Wen (1975, 1976) and used in random vibration studies of inelastic systems. When parameter n assumes large values (say $n > 10$) the transition from the elastic to the post-yielding regime is sharp and the Bouc-Wen model reasonably models bilinear behavior.

The parameters K , α and u_y are uniquely determined from the geometrical and material properties of the brace. The values of β and γ are constrained through the relation $\beta + \gamma = 1$, which leaves two fitting parameters, β and n (or γ and n).

When interested in modeling the hysteretic behavior of the yielding portion of the brace, the stiffness in the Bouc-Wen model is taken as

$$K = K_i = A_i E / L_i, \quad (5-3)$$

whereas, in the case that the flexibility of the connections is also incorporated, $K = K_{total}$, given by Equation (4-3). The yield displacement, u_y , is estimated by

$$u_y = \varepsilon_y L_i = \frac{\sigma_y}{E} L_i \quad (5-4)$$

and the post-yield to elastic stiffness is given by

$$\alpha = K_2 / K_i = E_t / E. \quad (5-5)$$

The parameters of the Bouc-Wen model are shown graphically in Figure 5-1. The figure also compares the prediction of the Bouc-Wen model with the data recorded for the first inelastic cycle (Test Phase 1) on Specimen 00-12. The parameters used in Figure 5-1 are listed in Table 5-1.

Table 5-1. Parameters used in Bouc-Wen Model

Parameter	Symbol	Value
Elastic stiffness	K	2367 kips/in
Ratio of post-yield to elastic stiffness	α	0.025
Yield displacement	$u_y = \frac{\sigma_y}{E} L_i$	0.19 in
Bouc-Wen parameter	β	0.55
Bouc-Wen parameter (1- β)	γ	0.45
Bouc-Wen parameter	n	1

Figure 5-2 compares the prediction of the Bouc-Wen model with force-displacement loops recorded during subsequent phases of the test on Specimen 00-12. In each test phase the specimen experiences appreciable inelastic deformations and thus strain hardens. This strain hardening increases the yield force and displacement in subsequent cycles. To account for this in the Bouc-Wen model the yield displacement is modified to

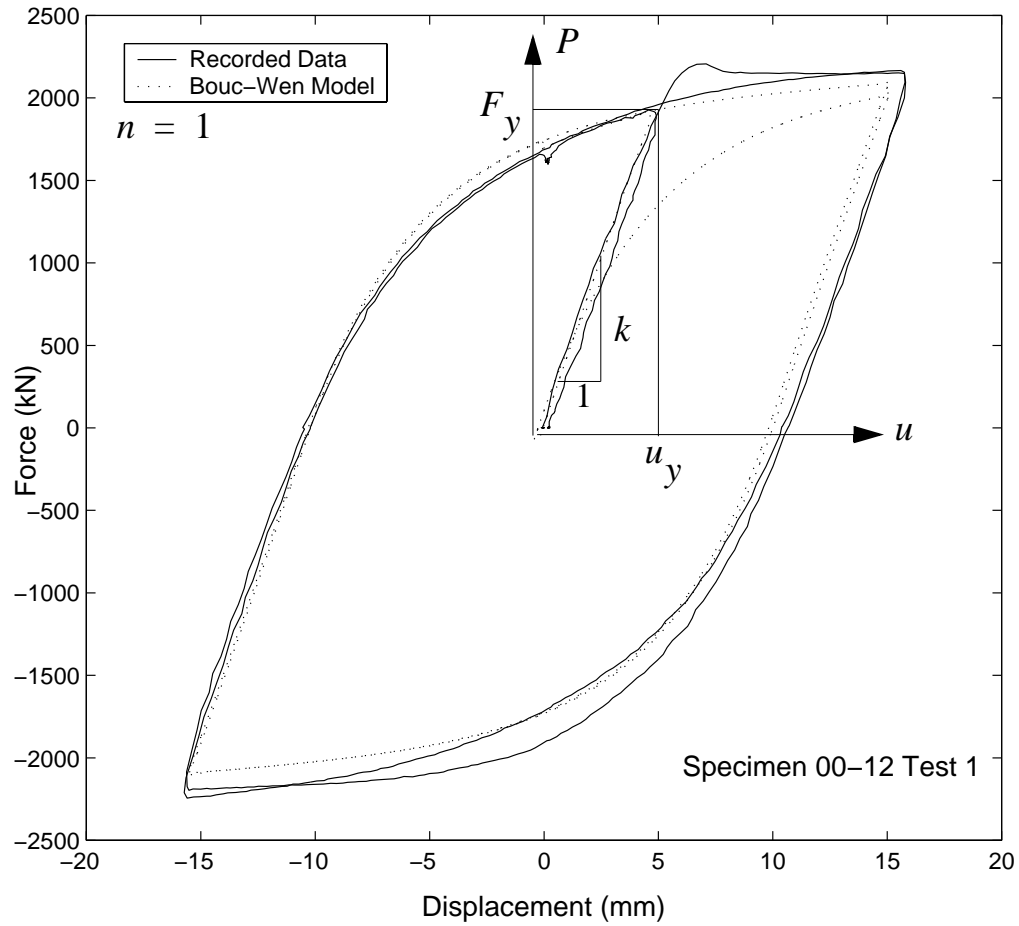


Figure 5-1. Comparison of recorded hysteresis loops obtained from the first inelastic test of Specimen 00-12 (Test 1, OSHPD Brace Loading History) and those obtained by the calibrated Bouc-Wen model.

$$u_y = 1.25 \frac{\sigma_y}{E} L_i. \quad (5-6)$$

The 25 percent increase in the yield displacement was chosen as an average value and corresponds approximately to the yield displacement expected in Test 4. Using a bilinear force-deformation approximation, the fractional change in the yield displacement for a given maximum ductility value, μ_{max} , is given by¹ $\Delta u_y / u_y = \alpha(\mu_{max} - 1)$. From Table 4-3, the maximum ductility in Test Phase 3 is 10 and thus $\Delta u_y / u_y = 0.025(10 - 1) = 0.23$. This result indicates that the brace yield displacement in Test 4 will be roughly 25 percent greater than a brace which has not been strain hardened. Figure 5-2 (bottom-left plot) confirms this value experimentally with the close agreement between the measured data for Test 4 and the Bouc-Wen model using the yield displacement given by Equation (5-6).

Figure 5-3 compares the prediction of the Bouc-Wen model with the force-displacement loops recorded during the DBE and the UBE respectively. The values used in the Bouc-Wen model are given in Table 5-1 with u_y given by Equation (5-6).

5.2 Estimation of Structural Response

With the macroscopic constitutive equation given by Equation (5-1) one can proceed with the dynamic analysis of a structure containing unbonded braces. Figure 5-4 portrays a frame with elastic lateral stiffness, K_o , and damping constant C_o , which supports a mass m . The frame includes an unbonded brace at an angle θ . The analysis presented here investigates the effect of the yielding brace on a linear structure. The analysis of a real structure should include the inelastic behavior of the frame together with the effect of the end moments on the brace. When the elastic frame is subjected to a ground excitation, $\ddot{u}_g(t)$, dynamic equilibrium gives

$$m\ddot{u}(t) + C_o\dot{u}(t) + K_o u(t) + P(t)\cos(\theta) = -m\ddot{u}_g(t) \quad (5-7)$$

where $u(t)$ is the lateral displacement of the frame and $P(t)$ is the axial force resulting from the inclined brace given by

1. Derivation of this formula is presented in Appendix B.

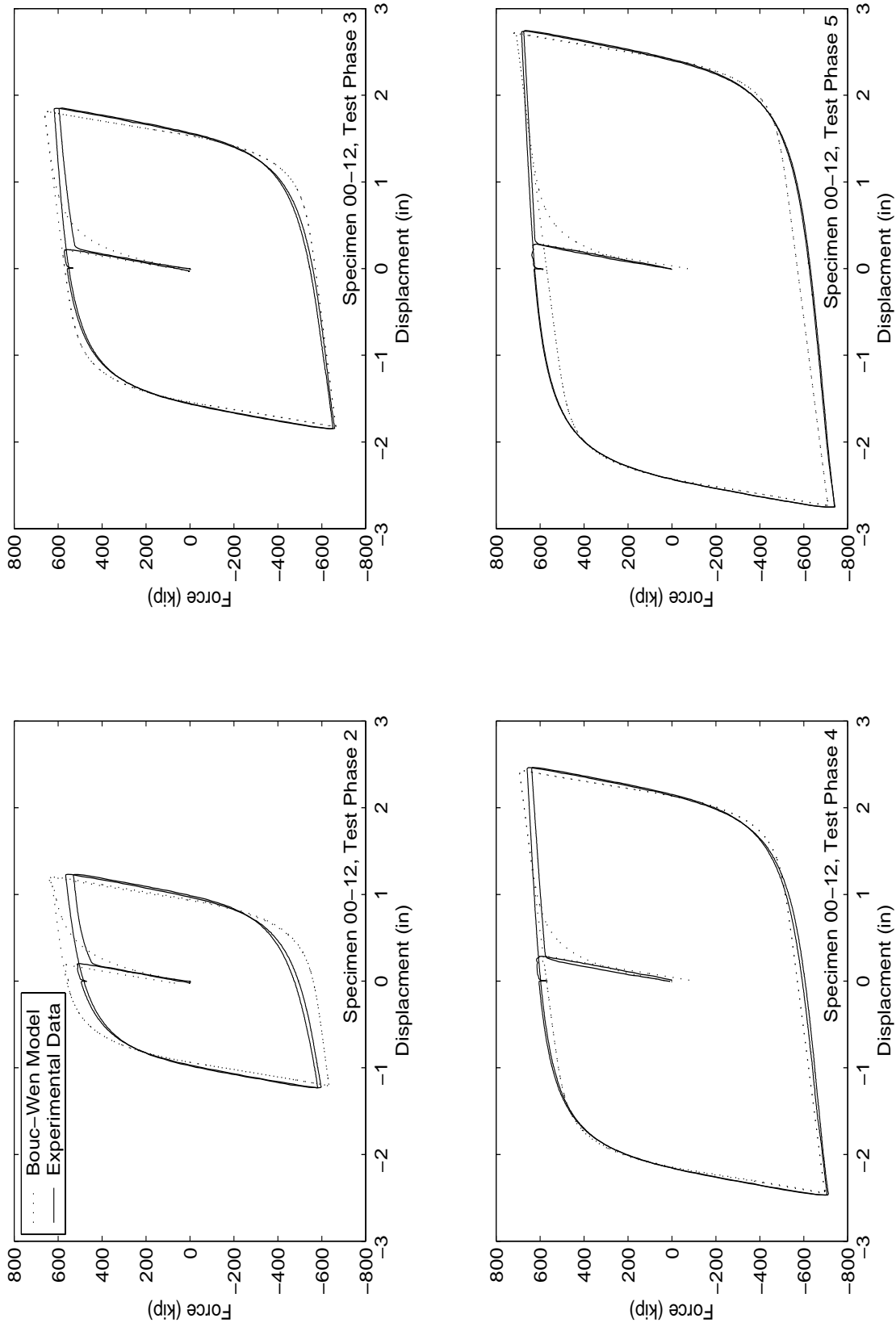


Figure 5-2. Comparison of experimental hysteresis loops from Specimen 00-12 and the Bouc-Wen approximation. The model has been calibrated to Test 4 (bottom-left).

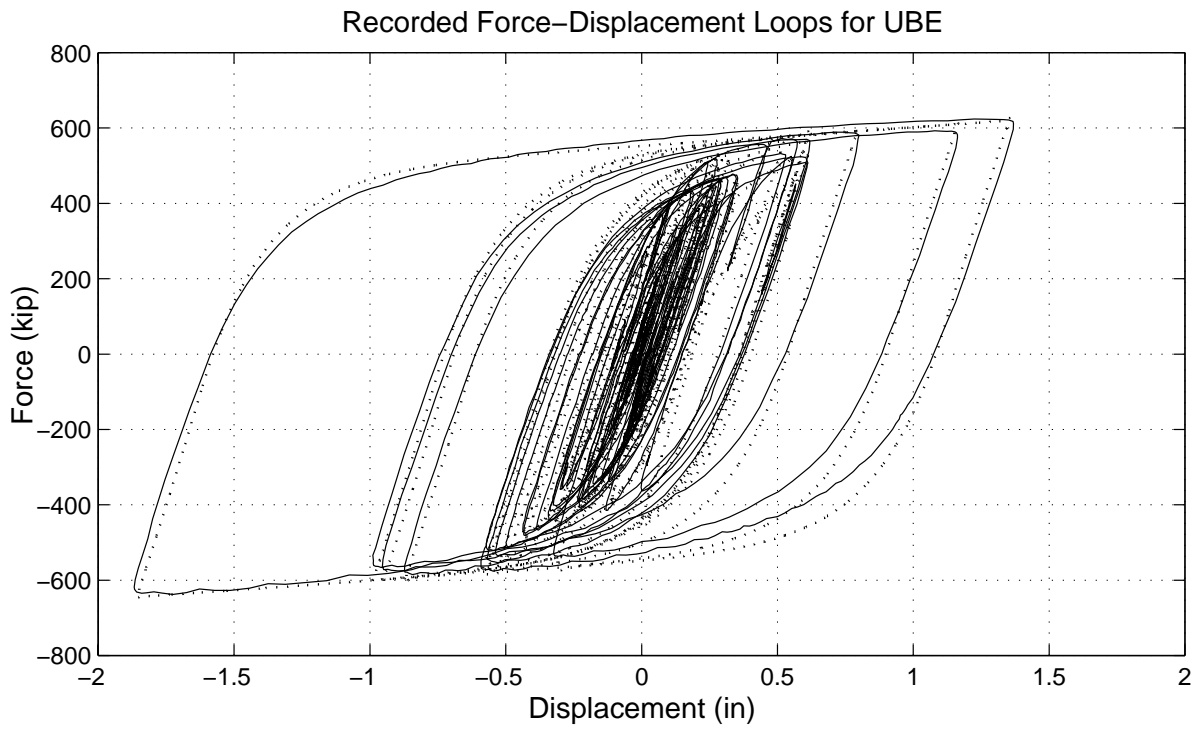
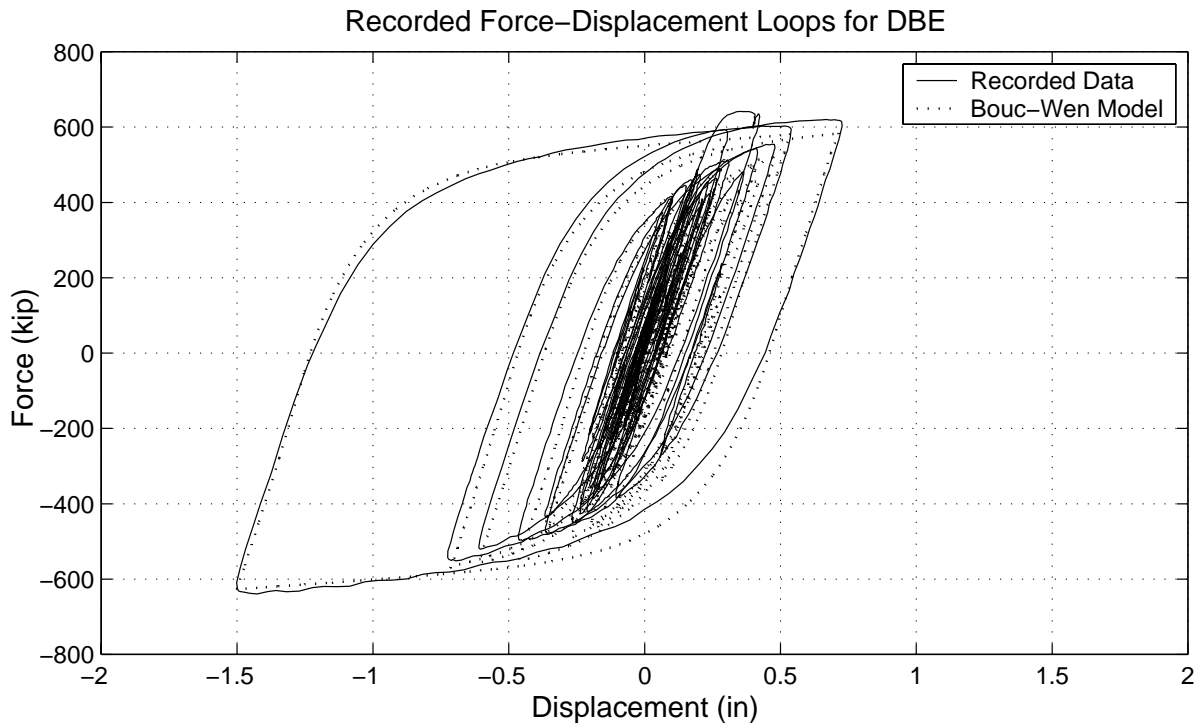


Figure 5-3. Comparison of recorded hysteresis loops obtained from Specimen 00-12 when subjected to the drift-induced loading histories and the calibrated Bouc-Wen model.

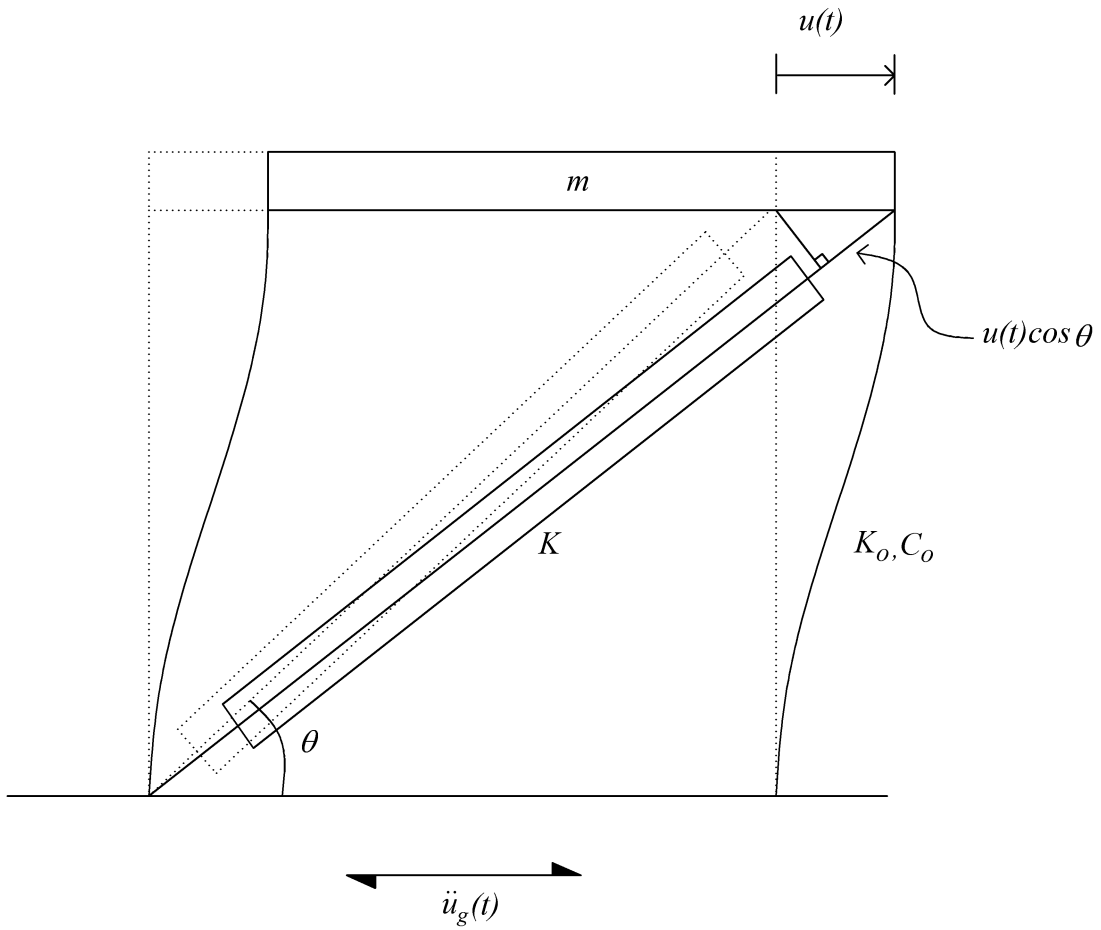


Figure 5-4. Schematic of a SDOF structure with an unbonded brace.

$$P(t) = \alpha K u(t) \cos(\theta) + (1 - \alpha) K u_y z. \quad (5-8)$$

In Equation (5-8), K is either K_i or K_{total} , and is given by Equations (4-4) or (4-3), respectively; whereas u_y , α and z are given by Equations (5-4), (5-5), and, (5-2) respectively.

With the introduction of the normalized yield force

$$f = \frac{F_y}{mg} = \frac{K u_y}{mg}, \quad (5-9)$$

Equation (5-8) becomes

$$P(t) = \alpha f m g \frac{u}{u_y} \cos(\theta) + (1 - \alpha) f m g z. \quad (5-10)$$

Substitution of Equation (5-10) into Equation (5-7) gives

$$\ddot{u}(t) + 2\zeta\omega_o\dot{u}(t) + \omega_o^2 u(t) + \alpha f g \frac{u(t)}{u_y} \cos^2(\theta) + (1 - \alpha) f g \cos(\theta) z = -\ddot{u}_g(t) \quad (5-11)$$

where $\omega_o = \sqrt{K/m}$ and $\zeta = C_o/(2m\omega_o)$.

Figures 5-5 through 5-7 plot nonlinear displacement and base shear spectra for the response of the single-degree-of-freedom structure shown in Figure 5-4. The spectra are plotted against the elastic period of the unbraced structure ($T_o = 2\pi/\omega_o = 2\pi\sqrt{m/K_o}$). The response is computed with a state-space formulation where Equations (5-2) and (5-11) are integrated simultaneously (Makris and Chang 2000).

The displacement spectra in the top row of Figures 5-5 through 5-7 indicate that the brace ductility demand increases rapidly with the period of the unbraced structure, T_o . Given that unbonded braces can achieve ductilities of the order of 15 or higher, the spectra for the 1971 San Fernando earthquake (Figure 5-6) and the 1979 El Centro earthquake (Figure 5-6) indicate that an unbraced structure with period $T_o = 1$ sec needs a brace strong enough to deliver a yield force $F_y = fmg$ that exceeds 20 percent of the weight of the structure. Although not considered here, when unbonded braces are used in building structures the satisfaction of the drift requirements should

be met by considering the simultaneous yielding of the frame, which will likely require an even stronger brace.

The spectra shown in Figure 5-7 is for the so-called LA01 record (Woodward-Clyde Federal Services 1997). This record was derived from the 1940 Imperial Valley, El Centro record, scaled to achieve a hazard level corresponding to a 10-percent probability of exceedance in 50 years. As discussed in Section 4.7, this record resulted in the largest Cumulative Plastic Ductility for a single brace in a six-story structure considered by Sabelli (2001). The maximum ductility for a single brace was 10.4, a value consistent with the values predicted by the spectra in Figure 5-7 at a period of 0.55 sec (the design period of the structure).

In addition to the response calculated with the Bouc-Wen model, Figures 5-5 through 5-7 plot the response calculated using a bilinear model. The solid lines in the graphs of Figures 5-5 through 5-7 are computed by setting the parameter n in the Bouc-Wen model equal to one. The dashed lines are computed by setting $n = 20$ which gives a bilinear model (i.e., sharp transition from the elastic to the post-yielding regime). The good agreement between the solid and dashed lines for all the earthquakes studied indicates that engineers can use with confidence the bilinear element which is included in commercially available structural analysis programs in order to represent the nonlinear post-yielding behavior of unbonded braces.

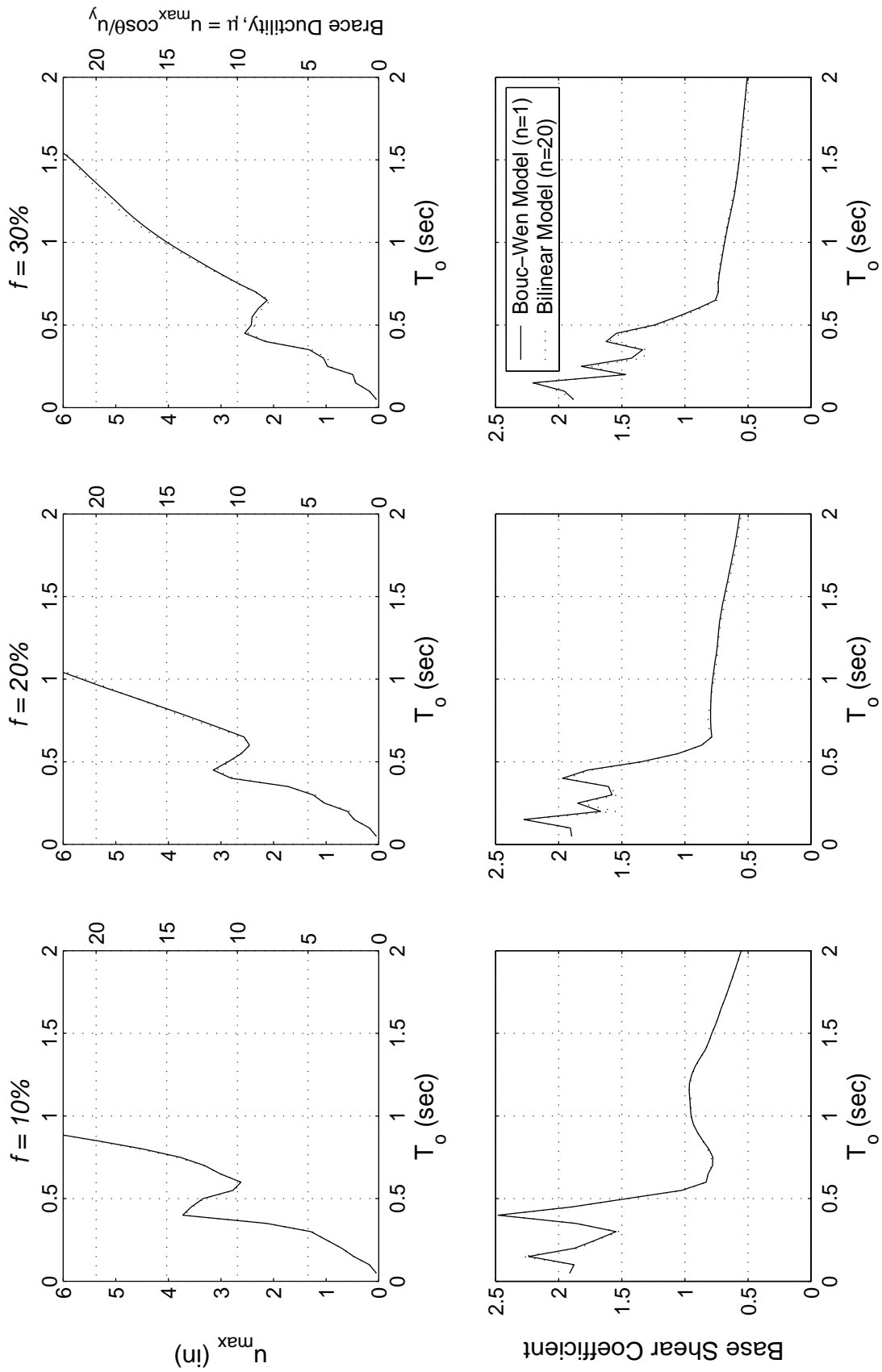


Figure 5-5. Exact drift and base shear spectra for a linear SDOF structure with an unbonded brace subjected to the 1971 San Fernando earthquake, Pacoima Dam record. Solid line: Bouc-Wen model with $n = 1$. Dashed line: Bilinear approximation $n = 20$.

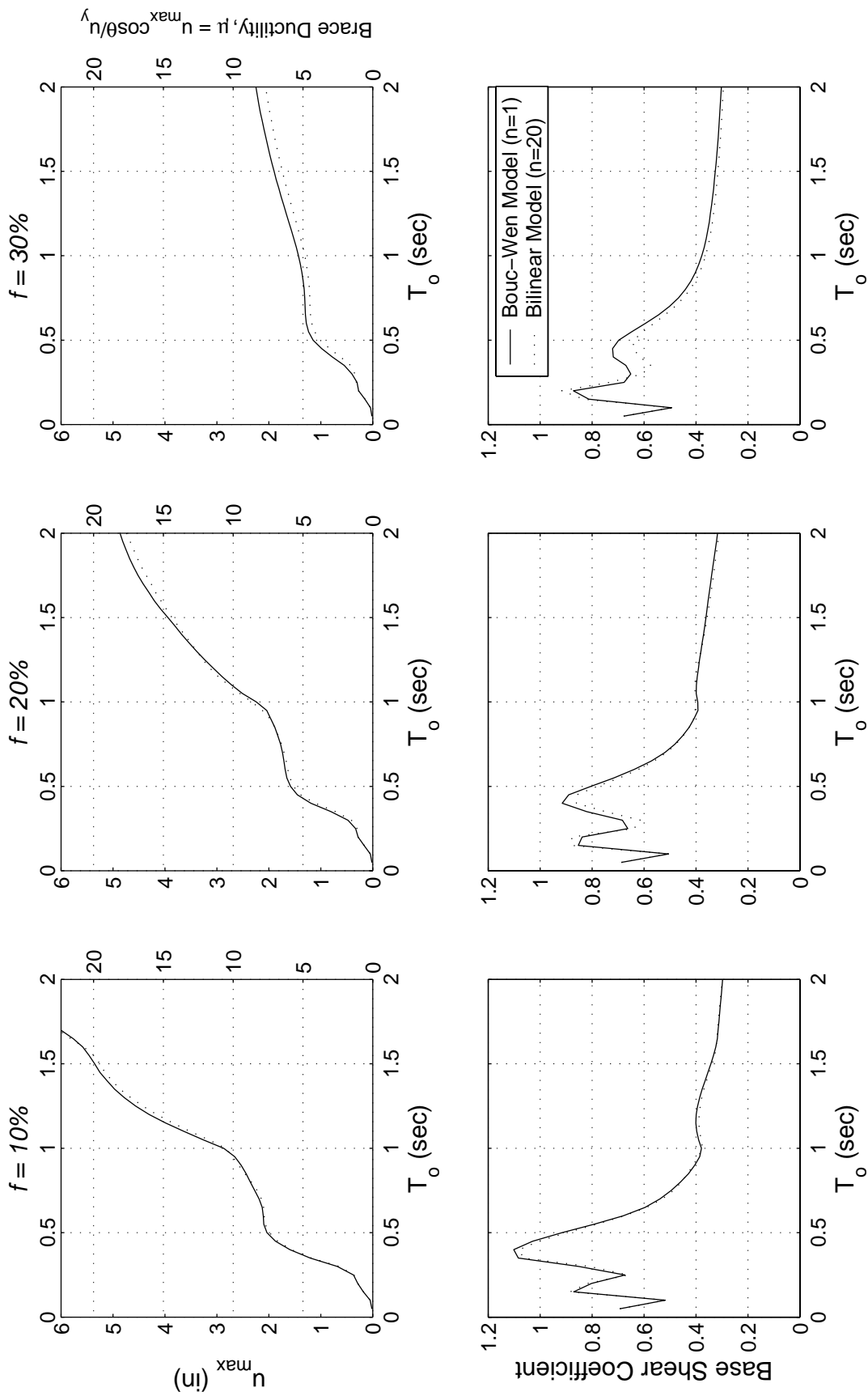


Figure 5-6. Exact drift and base shear spectra for a linear SDOF structure with an unbonded brace subjected to the 1979 El Centro earthquake, Array #5 record. Solid line: Bouc-Wen model with $n = 1$. Dashed line: Bilinear approximation $n = 20$.

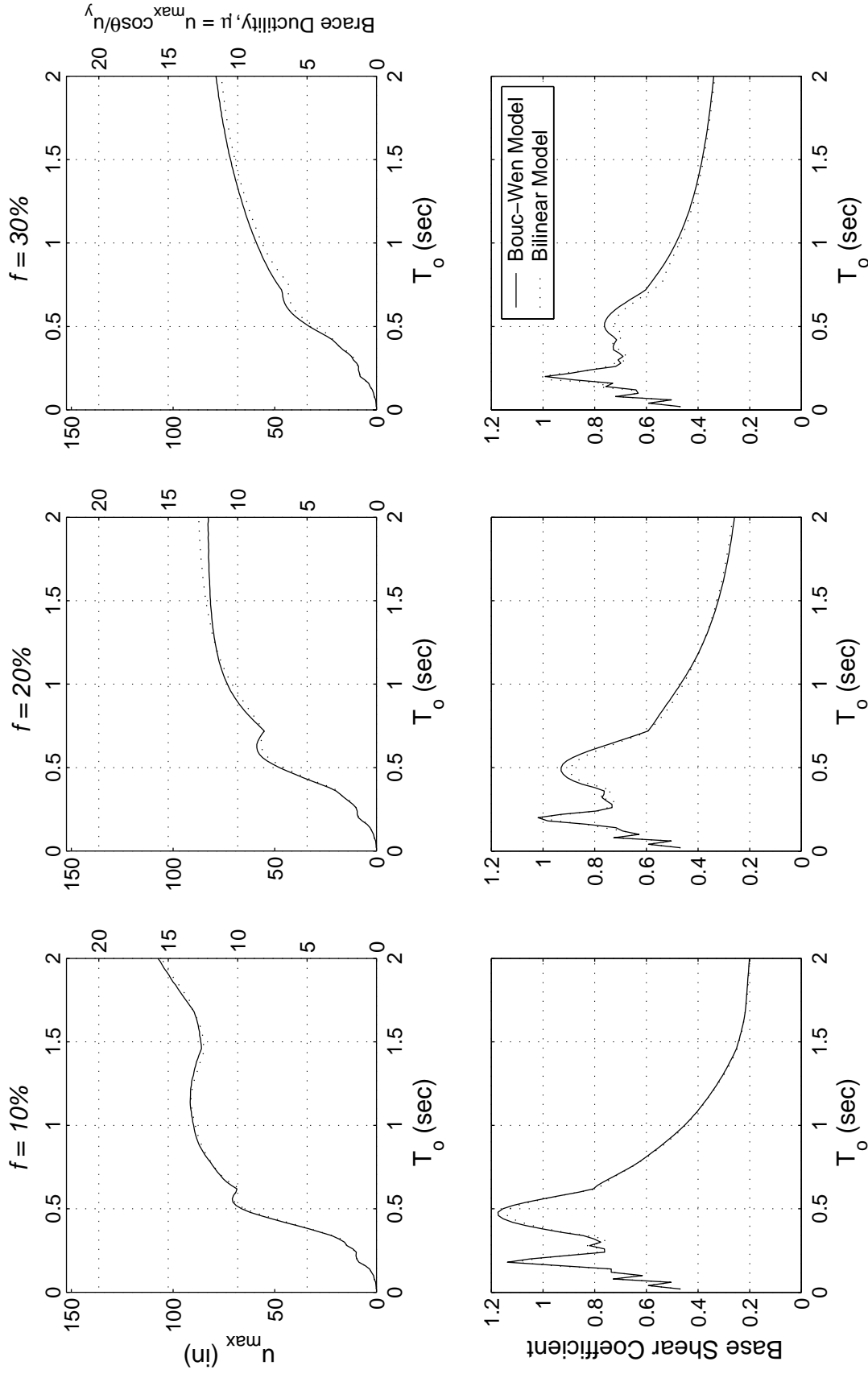


Figure 5-7. Exact drift and base shear spectra for a linear SDOF structure with an unbonded brace subjected to the SAC LA01 record. Solid line: Bouc-Wen model with $n = 1$. Dashed line: Bilinear approximation $n = 20$.

6 Conclusions

This report presented results from a two-phase experimental program on the axial behavior of unbonded braces. The test results demonstrated good performance of the braces under various loading histories specified by the SAC and OSHPD protocols.

The experimental data were used to (a) verify the results of theoretical predictions on the structural stability of the unbonded braces; (b) validate the inelastic capacity of the braces under severe earthquake demands; and (c) calibrate a macroscopic hysteretic model that was found to predict, with fidelity, the brace force-displacement behavior.

For the configuration of the braces tested, this study found that plastic torsional buckling of the inner core is the most critical stability mode. It is concluded that if the yielding portion extends outside of the confining tube, the flanges of the yielding portion should have a width to thickness ratio of $b/t < 5$. The study indicates that the incremental theory of plasticity predicts the correct critical load for plastic torsional buckling, provided that the flanges of the cruciform are assumed to be slightly bent.

Results from a comprehensive experimental test program demonstrate that unbonded braces deliver ductile, stable and repeatable hysteretic behavior. The plastic deformation capacity of the braces exceeded the specified requirements for both phases, both in terms of ultimate deformation and in terms of cumulative plastic strain.

A Bouc-Wen model was proposed to approximate the macroscopic behavior of the unbonded brace. All but two of the model parameters are determined from the geometrical and physical properties of the brace. A single set of calibrated model parameters was found to satisfactorily predict the cyclic and transient behavior of the brace when subjected to a variety of loading histories. The proposed macroscopic model can be easily implemented to compute the dynamic response of structures that include unbonded braces. Additional parametric studies indicated that

a simple bilinear model satisfactorily represents the brace nonlinear behavior for structural design purposes.

Unbonded braces are a reliable and practical alternative to conventional framing systems to enhance the earthquake resistance of existing and new structures. Unbonded braces are capable of providing both the rigidity needed to satisfy structural drift limits, and a stable and substantial energy absorption capability.

References

- Batdorf, S. B. (1949). Theories of plastic buckling. *J. Aeronautical Sciences*. July, 405-8.
- Bazant, Z. P., and Cedolin, L. (1991). *Stability of structures*. Oxford, U.K.: Oxford University Press.
- Bergman, D. M., and Goel, S. C. (1987). *Evaluation of cyclic testing of steel-plate devices for added damping and stiffness*. Technical Report UMCE 87-10. Ann Arbor, Mich.: University of Michigan.
- Bijlaard, P. P. (1956). Theory of plastic buckling of plates and application to simply supported plates subjected to bending or eccentric compression in their plane. *J. Applied Mechanics* 23(1):27-34.
- Bleich, F. (1952). *Buckling strength of metal structures*. New York: McGraw-Hill.
- Bouc, R. (1971). Modèl mathématique d'hysteresis. *Acustica* 24:16-25.
- Gerard, G., and Becker, H. (1957). *Handbook of structural stability: Part I, Buckling of flat plates*. National Advisory Committee for Aeronautics. NACA Tech. Note 3781.
- Green A. E., and Naghdi, P. M. (1965). *A general theory of an elastic-plastic continuum*. *Arch. Rat. Mech. Anal.* 18:251-81.
- Haaijer G. (1957). Plate buckling in the strain-hardening range. *J. Engineering Mechanics Division* 83(EM2): 1-47. ASCE.
- Handelmann, G. H., and Prager, W. (1948). *Plastic buckling of a rectangular plate under edge thrust*. Nat. Adv. Comm. Aeronautics. Tech. Note 1530.
- Hasegawa, H., Takeuchi, T., Nakata, Y., Iwata, M., Yamada, S., Akiyama, H. (1999). Experimental study on dynamic behavior of unbonded braces. *AIJ J. Technol. Des.* 9:103-106 (in Japanese).
- Hutchinson, J. W. (1974). Plastic buckling. In *Advances in Applied Mechanics*, C-S. Yih ed. New York: Academic Press.
- Ilyushin, A. A. (1947). *The elasto-plastic stability of plates*. Nat. Adv. Comm. Aeronautics. Tech. Note 1188.

- Iwata, M., Kato, T., Wada, A. (2000). Buckling-restrained braces as hysteretic dampers. In *Proceedings of Third International Conference on Behavior of Steel Structures in Seismic Areas* (STESSA 2000), Montreal, Canada, 33-38. Rotterdam; and Brookfield, Vt.: A.A. Balkema.
- Kelly, J. M., Skinner, R. I., and Heine, A. J. (1992). Mechanism of energy absorption in special devices for use in earthquake resistant structures. *Bull. N.Z. Nat. Soc. Earthquake Eng.* 5(3):63-88.
- Kimura, K., Takeda, Y., Yoshioka, K., Furuya, N., and Takemoto, Y. (1976). An experimental study on braces encased in steel tube and mortar. Annual Meeting of the Architectural Institute of Japan (in Japanese).
- Konami, S., Sugihara, H., Narikawa, M., Huan, Y. H., Maeda, Y., and Wada, A. (1999). Seismic performance of moment resisting frames with hysteretic damper. Annual Meeting of the Architectural Institute of Japan (in Japanese).
- Lubliner, J. (1990). *Plasticity theory*. New York: Macmillan.
- Makris, N. (2002). Plastic torsional buckling of a cruciform column. *J. Engrg. Mech.* ASCE. In review.
- Mochizuki, N., Murata, Y., Andou, N., Takahashi, S. (1988) An experimental study on buckling of unbonded braces under centrally applied loads. Annual Meeting of the Architectural Institute of Japan (in Japanese).
- Onat, E. T., and Drucker, D. C. (1952). Inelastic instability and incremental theories of plasticity. *J. Aeronautical Sciences* 20(3):181-86.
- Papadopoulos, P., and Lu, J. (1998). A general framework for the numerical solution of problems in finite elasto-plasticity. *Comput. Meth. Appl. Mech. Engrg.* 159:1-18.
- Sabelli, R. (2001). Research on improving the design and analysis of earthquake-resistant steel braced frames. EERI/FEMA NEHRP Fellowship Report. Oakland, Calif.
- Salmon, C. G., and Johnson, J. E. (1996). *Steel structures: design and behavior, emphasizing load and resistance factor design*. Fourth ed. New York: Harper Collins College Publishers.
- Simo and Hughes (1998). *Computational inelasticity*. Interdisciplinary Applied Mathematics, Vol. 7. New York: Springer-Verlag.
- Skinner, R. I., Kelly, M. J., and Heine A. J. (1975). Hysteretic dampers for earthquake-resistant structures. *Earthquake Engng and Struct. Dyn.* 3:287-96.
- Stowell, E. Z. (1948). *Unified theory of plastic buckling of columns and plates*. Nat. Adv. Comm. Aeronautics. Tech. Note 1681.
- Timoshenko, S. P., and Gere, J. M. (1961). *Theory of elastic stability*. New York: McGraw-Hill.

- Tsai, K. C., Chen, H. W., Hong, C. P. and Su, Y. F. (1993). Design of steel triangular plate energy absorbers for seismic-resistant construction. *Earthquake Spectra* 9(3):505-28.
- Tyler, R. G. (1978). Tapered steel cantilever energy absorbers. *Bull. N.Z. Nat. Soc. for Earthquake Eng.* 11(4):282-94.
- Wada, A., Saeki, E., Takeuch, T., Watanabe, A. (1989). Development of unbonded brace. In *Column* (A Nippon Steel Publication), No.115, 12.
- Watanabe, A., Hitomoi, Y., Saeki, E., Wada, A., Fujimoto, M., (1988). Properties of braced encased in buckling-restraining concrete and steel tube. In *Proceedings of Ninth World Conference on Earthquake Engineering*, Tokyo-Kyoto, Japan, Vol. IV, 719-24. Tokyo: 9WCEE Organizing Committee, Japan Association for Earthquake Disaster Prevention.
- Watanabe, A., Nakamura, H. (1992). Study on the behavior of buildings using steel with low yield point. In *Proceedings of Tenth World Conference on Earthquake Engineering*, 4465-68. A.A. Balkema: Rotterdam.
- Wen, Y-K. (1975). Approximate method for nonlinear random vibration. *J. Engrg. Mech.* 102(EM4):389-401. ASCE.
- Wen, Y-K. (1976). Method for random vibration of hysteretic systems. *J. Engrg. Mech.* 102(EM2):249-63. ASCE.
- Whittaker, A. S., Aiken, I. D., Bergman, D., Clark, P. W., Cohen, J., Kelly, J. M., Scholl, R. (1993). Code requirements for the design and implementation of passive energy dissipation systems. In *Proc. of ATC 17-1 Seminar on Seismic Isolation, Passive Energy Dissipation and Active Control*, San Francisco, California, March 11-12, 1993, Vol. 2, 497-508. Redwood City, Calif.: Applied Technology Council.
- Woodward-Clyde Federal Services. (1997). *Develop suites of time histories*. Draft report to SAC Joint Venture Steel Project, Task 5.4.1. Pasadena, Calif.

Appendix A Acceptance Criteria for Fall 2000 Tests

Prior to conducting the testing program, a number of criteria were defined¹ to evaluate the adequacy of the behavior of the unbonded brace test specimens during the OSHPD brace loading history. The criteria put forward by SIE, Inc., Nippon Steel Corporation and Ove Arup & Partners California were accepted by OSHPD December 12, 2000. The acceptance criteria and the outcome of the tests on Specimens 00-11 and 00-12 are given below.

Requirement 1

All tests conducted on both specimens shall be witnessed by representatives of OSHPD, Ove Arup & Partners and Nippon Steel Corporation.

Outcome: satisfied

All tests of Specimen 00-11 and 00-12 were witnessed by representatives of OSHPD, Ove Arup & Partners, Nippon Steel Corporation and SIE, Inc.

Requirement 2

The force-displacement hysteresis loops for all tests of both specimens shall exhibit stable, repeatable behavior, with positive incremental stiffness for all cycles in all tests. At the maximum brace deformation, corresponding to 2.25 percent story drift ratio, there shall be no strength degradation below 80 percent of the maximum strength identified for all cycles in all tests.

Outcome: satisfied

The force-displacement hysteresis loops for all tests exhibited stable, repeatable behavior. The ratio of brace force at maximum/minimum deformation (corresponding to 2.25 percent story drift ratio) to the maximum/minimum brace force was in all cases greater than 80 percent. This information is presented in Table A-1.

1. *Protocol For Cyclic Tests of Nippon Steel Corporation Unbonded Braces*, Rev. 1, November 27, 2000, by SIE, Inc., Nippon Steel Corporation, and Ove Arup & Partners California, Ltd.

Table A-1. Specimens 00-11 and 00-12 maximum forces — Acceptance requirement 2

Compression/Tension	Brace Deformation		Brace Force (kips)		
	(inches)	Strain (%)	Maximum	At Maximum Deformation	Ratio
Specimen 00-11					
Maximum Tension	2.75	2.05	675.6	660.4	97.8%
Maximum Compression	-3.08	-2.30	-764.3	-744.3	97.4%
Specimen 00-12					
Maximum Tension	2.73	2.04	684.4	665.2	97.2%
Maximum Compression	-2.74	-2.04	-742.4	-731.9	98.6%

Requirement 3

There shall be no signs of fracture or failure in any of the tests.

Outcome: satisfied

There were no signs of fracture or failure in any of the OSHPD brace loading history tests.

Requirement 4

The steel core material yield stress, as determined from the results of those tests in which the specimens are loaded beyond the yield point, shall be between the JIS SN400B lower and upper limits of 34.1 ksi and 51.5 ksi, respectively.

Outcome: satisfied

From the results of Test 1, the steel core yield stress was 40.9 ksi for Specimen 00-11 and 40.7 ksi for Specimen 00-12. These values are within 1 percent of those determined by coupon tests.

Appendix B Estimation of Yield Displacement

In this appendix a simplified bilinear force-deformation relationship is used to establish a relation between maximum brace displacement and the yield displacement.

With reference to Figure B-1, the maximum force, F_{max} , can be expressed in terms of the maximum and yield displacements

$$F_{max} = ku_y + k_2(u_{max} - u_y) \quad (\text{B-1})$$

or an equivalent elastic displacement

$$F_{max} = k(u_y + \Delta u_y). \quad (\text{B-2})$$

Equating Equations (B-1) and (B-2) yields

$$\Delta u_y = \frac{k_2}{k}(u_{max} - u_y), \quad (\text{B-3})$$

which when divided by u_y gives the fractional change in yield displacement expressed as a function of maximum ductility, μ_{max} :

$$\frac{\Delta u_y}{u_y} = \frac{k_2}{k}(\mu_{max} - 1) = \alpha(\mu_{max} - 1) \quad (\text{B-4})$$

where α is defined as the ratio of post-yield to elastic stiffness.

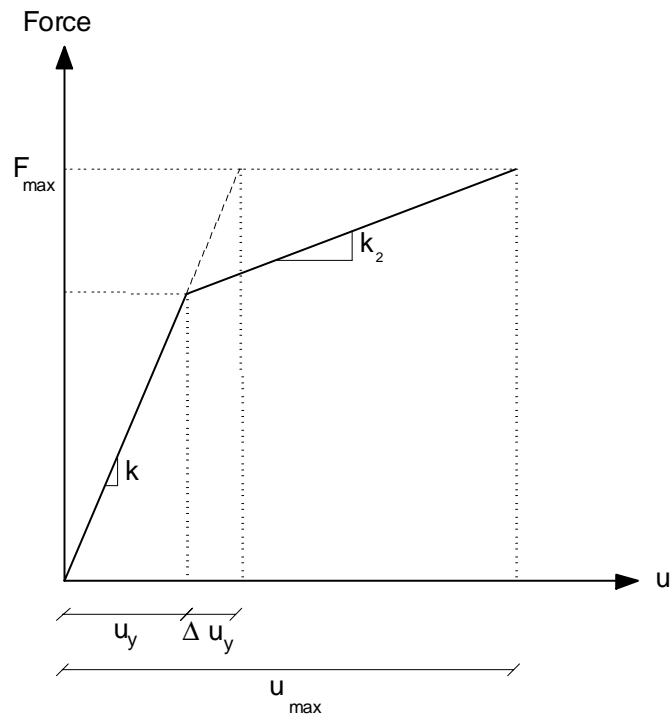


Figure B-1. Bilinear force-deformation relation.

PEER REPORTS

PEER reports are available from the National Information Service for Earthquake Engineering (NISEE). To order PEER reports, please contact the Pacific Earthquake Engineering Research Center, 1301 South 46th Street, Richmond, California 94804-4698. Tel.: (510) 231-9468; Fax: (510) 231-9461.

- PEER 2002/08** *Component Testing, Stability Analysis and Characterization of Buckling-Restrained Unbonded BracesTM*. Cameron Black, Nicos Makris, and Ian Aiken. September 2002.
- PEER 2002/07** *Seismic Performance of Pile-Wharf Connections*. Charles W. Roeder, Robert Graff, Jennifer Soderstrom, and Jun Han Yoo. December 2001.
- PEER 2002/06** *The Use of Benefit-Cost Analysis for Evaluation of Performance-Based Earthquake Engineering Decisions*. Richard O. Zerbe and Anthony Falit-Baiamonte. September 2001.
- PEER 2002/05** *Guidelines, Specifications, and Seismic Performance Characterization of Nonstructural Building Components and Equipment*. André Filiatrault, Constantin Christopoulos, and Christopher Stearns. September 2001.
- PEER 2002/01** *Nonstructural Loss Estimation: The UC Berkeley Case Study*. Mary C. Comerio and John C. Stallmeyer. December 2001.
- PEER 2001/16** *Statistics of SDF-System Estimate of Roof Displacement for Pushover Analysis of Buildings*. Anil K. Chopra, Rakesh K. Goel, and Chatpan Chintanapakdee. December 2001.
- PEER 2001/15** *Damage to Bridges during the 2001 Nisqually Earthquake*. R. Tyler Ranf, Marc O. Eberhard, and Michael P. Berry. November 2001.
- PEER 2001/14** *Rocking Response of Equipment Anchored to a Base Foundation*. Nicos Makris and Cameron J. Black. September 2001.
- PEER 2001/13** *Modeling Soil Liquefaction Hazards for Performance-Based Earthquake Engineering*. Steven L. Kramer and Ahmed-W. Elgamal. February 2001.
- PEER 2001/12** *Development of Geotechnical Capabilities in OpenSees*. Boris Jeremic. September 2001.
- PEER 2001/11** *Analytical and Experimental Study of Fiber-Reinforced Elastomeric Isolators*. James M. Kelly and Shakhzod M. Takhirov. September 2001.
- PEER 2001/10** *Amplification Factors for Spectral Acceleration in Active Regions*. Jonathan P. Stewart, Andrew H. Liu, Yoojoong Choi, and Mehmet B. Baturay. December 2001.
- PEER 2001/09** *Ground Motion Evaluation Procedures for Performance-Based Design*. Jonathan P. Stewart, Shyh-Jeng Chiou, Jonathan D. Bray, Robert W. Graves, Paul G. Somerville, and Norman A. Abrahamson. September 2001.
- PEER 2001/08** *Experimental and Computational Evaluation of Reinforced Concrete Bridge Beam-Column Connections for Seismic Performance*. Clay J. Naito, Jack P. Moehle, and Khalid M. Mosalam. November 2001.

- PEER 2001/07** *The Rocking Spectrum and the Shortcomings of Design Guidelines.* Nicos Makris and Dimitrios Konstantinidis. August 2001.
- PEER 2001/06** *Development of an Electrical Substation Equipment Performance Database for Evaluation of Equipment Fragilities.* Thalia Agnanos. April 1999.
- PEER 2001/05** *Stiffness Analysis of Fiber-Reinforced Elastomeric Isolators.* Hsiang-Chuan Tsai and James M. Kelly. May 2001.
- PEER 2001/04** *Organizational and Societal Considerations for Performance-Based Earthquake Engineering.* Peter J. May. April 2001.
- PEER 2001/03** *A Modal Pushover Analysis Procedure to Estimate Seismic Demands for Buildings: Theory and Preliminary Evaluation.* Anil K. Chopra and Rakesh K. Goel. January 2001.
- PEER 2001/02** *Seismic Response Analysis of Highway Overcrossings Including Soil-Structure Interaction.* Jian Zhang and Nicos Makris. March 2001.
- PEER 2001/01** *Experimental Study of Large Seismic Steel Beam-to-Column Connections.* Egor P. Popov and Shakhzod M. Takhirov. November 2000.
- PEER 2000/10** *The Second U.S.-Japan Workshop on Performance-Based Earthquake Engineering Methodology for Reinforced Concrete Building Structures.* March 2000.
- PEER 2000/09** *Structural Engineering Reconnaissance of the August 17, 1999 Earthquake: Kocaeli (Izmit), Turkey.* Halil Sezen, Kenneth J. Elwood, Andrew S. Whittaker, Khalid Mosalam, John J. Wallace, and John F. Stanton. December 2000.
- PEER 2000/08** *Behavior of Reinforced Concrete Bridge Columns Having Varying Aspect Ratios and Varying Lengths of Confinement.* Anthony J. Calderone, Dawn E. Lehman, and Jack P. Moehle. January 2001.
- PEER 2000/07** *Cover-Plate and Flange-Plate Reinforced Steel Moment-Resisting Connections.* Taejin Kim, Andrew S. Whittaker, Amir S. Gilani, Vitelmo V. Bertero, and Shakhzod M. Takhirov. September 2000.
- PEER 2000/06** *Seismic Evaluation and Analysis of 230-kV Disconnect Switches.* Amir S. J. Gilani, Andrew S. Whittaker, Gregory L. Fenves, Chun-Hao Chen, Henry Ho, and Eric Fujisaki. July 2000.
- PEER 2000/05** *Performance-Based Evaluation of Exterior Reinforced Concrete Building Joints for Seismic Excitation.* Chandra Clyde, Chris P. Pantelides, and Lawrence D. Reaveley. July 2000.
- PEER 2000/04** *An Evaluation of Seismic Energy Demand: An Attenuation Approach.* Chung-Che Chou and Chia-Ming Uang. July 1999.
- PEER 2000/03** *Framing Earthquake Retrofitting Decisions: The Case of Hillside Homes in Los Angeles.* Detlof von Winterfeldt, Nels Roselund, and Alicia Kitsuse. March 2000.
- PEER 2000/02** *U.S.-Japan Workshop on the Effects of Near-Field Earthquake Shaking.* Andrew Whittaker, ed. July 2000.

- PEER 2000/01** *Further Studies on Seismic Interaction in Interconnected Electrical Substation Equipment.* Armen Der Kiureghian, Kee-Jeung Hong, and Jerome L. Sackman. November 1999.
- PEER 1999/14** *Seismic Evaluation and Retrofit of 230-kV Porcelain Transformer Bushings.* Amir S. Gilani, Andrew S. Whittaker, Gregory L. Fenves, and Eric Fujisaki. December 1999.
- PEER 1999/13** *Building Vulnerability Studies: Modeling and Evaluation of Tilt-up and Steel Reinforced Concrete Buildings.* John W. Wallace, Jonathan P. Stewart, and Andrew S. Whittaker, editors. December 1999.
- PEER 1999/12** *Rehabilitation of Nonductile RC Frame Building Using Encasement Plates and Energy-Dissipating Devices.* Mehrdad Sasani, Vitelmo V. Bertero, James C. Anderson. December 1999.
- PEER 1999/11** *Performance Evaluation Database for Concrete Bridge Components and Systems under Simulated Seismic Loads.* Yael D. Hose and Frieder Seible. November 1999.
- PEER 1999/10** *U.S.-Japan Workshop on Performance-Based Earthquake Engineering Methodology for Reinforced Concrete Building Structures.* December 1999.
- PEER 1999/09** *Performance Improvement of Long Period Building Structures Subjected to Severe Pulse-Type Ground Motions.* James C. Anderson, Vitelmo V. Bertero, and Raul Bertero. October 1999.
- PEER 1999/08** *Envelopes for Seismic Response Vectors.* Charles Menun and Armen Der Kiureghian. July 1999.
- PEER 1999/07** *Documentation of Strengths and Weaknesses of Current Computer Analysis Methods for Seismic Performance of Reinforced Concrete Members.* William F. Cofer. November 1999.
- PEER 1999/06** *Rocking Response and Overturning of Anchored Equipment under Seismic Excitations.* Nicos Makris and Jian Zhang. November 1999.
- PEER 1999/05** *Seismic Evaluation of 550 kV Porcelain Transformer Bushings.* Amir S. Gilani, Andrew S. Whittaker, Gregory L. Fenves, and Eric Fujisaki. October 1999.
- PEER 1999/04** *Adoption and Enforcement of Earthquake Risk-Reduction Measures.* Peter J. May, Raymond J. Burby, T. Jens Feeley, and Robert Wood.
- PEER 1999/03** *Task 3 Characterization of Site Response General Site Categories.* Adrian Rodriguez-Marek, Jonathan D. Bray, and Norman Abrahamson. February 1999.
- PEER 1999/02** *Capacity-Demand-Diagram Methods for Estimating Seismic Deformation of Inelastic Structures: SDF Systems.* Anil K. Chopra and Rakesh Goel. April 1999.
- PEER 1999/01** *Interaction in Interconnected Electrical Substation Equipment Subjected to Earthquake Ground Motions.* Armen Der Kiureghian, Jerome L. Sackman, and Kee-Jeung Hong. February 1999.
- PEER 1998/08** *Behavior and Failure Analysis of a Multiple-Frame Highway Bridge in the 1994 Northridge Earthquake.* Gregory L. Fenves and Michael Ellery. December 1998.

- PEER 1998/07** *Empirical Evaluation of Inertial Soil-Structure Interaction Effects.* Jonathan P. Stewart, Raymond B. Seed, and Gregory L. Fenves. November 1998.
- PEER 1998/06** *Effect of Damping Mechanisms on the Response of Seismic Isolated Structures.* Nicos Makris and Shih-Po Chang. November 1998.
- PEER 1998/05** *Rocking Response and Overturning of Equipment under Horizontal Pulse-Type Motions.* Nicos Makris and Yiannis Roussos. October 1998.
- PEER 1998/04** *Pacific Earthquake Engineering Research Invitational Workshop Proceedings, May 14–15, 1998: Defining the Links between Planning, Policy Analysis, Economics and Earthquake Engineering.* Mary Comerio and Peter Gordon. September 1998.
- PEER 1998/03** *Repair/Upgrade Procedures for Welded Beam to Column Connections.* James C. Anderson and Xiaojing Duan. May 1998.
- PEER 1998/02** *Seismic Evaluation of 196 kV Porcelain Transformer Bushings.* Amir S. Gilani, Juan W. Chavez, Gregory L. Fenves, and Andrew S. Whittaker. May 1998.
- PEER 1998/01** *Seismic Performance of Well-Confined Concrete Bridge Columns.* Dawn E. Lehman and Jack P. Moehle. December 2000.